University of Strathclyde

Department of Pure and Applied Chemistry

Deciphering Optical Properties of Hollow Gold Nanospheres

By

Hainan Xie

A thesis presented in fulfilment of the requirements for the degree of Doctor of Philosophy.

2012

Signed:

Date:

Acknowledgements

A three year PhD is actually very short and I was not sure what I could achieve three years ago. Now it comes to the end and I am very proud to say that these three years are the most important and amazing period in my life. There are so many people to be acknowledged and here I only list some of them who are directly related to this thesis.

Firstly, I would like to give my biggest thank to my family for their firm support in the past three years.

Secondly, I would like to thank my supervisors Prof. Duncan Graham and Dr. Karen Faulds for their guidance through my PhD projects.

Thirdly, I would like to thank Dr. Iain Larmour, Dr. Ross Stevenson, Dr. Alastair Wark, Prof. Nicholas Stone, Prof. W Ewen Smith and Dr. Jennifer Dougan for their direct help.

In addition, I would like to thank Danny van Lierop, Richard Cassar and the rest of the Raman group who brought me lots of fun and made my lab life colourful.

Finally, I would like to thank the Scottish Overseas Research Students Award Scheme (SORSAS) and University of Strathclyde for their generous financial support.

I am sure without any of these people and funding sources, things could not go smoothly. Thank you all so much!

Abstract

Hollow gold nanospheres (HGNs) demonstrate a tunable localised surface plasmon resonance ranged from the visible to near infrared (NIR) which is of significant importance for bioimaging due to the better penetration depth and reduced autofluorescence. They consist of high quality nanoshells with a small size and spherical shape. However, the reproducibility of the synthesis is an issue especially for HGNs with localised surface plasmon resonances (LSPRs) in the NIR region. Also the optical properties of these nanostructures are not yet well understood. In this thesis, the improved synthesis of hollow gold nanospheres (HGNs), which extends their localised surface plasmon resonances up to 1320 nm with citrate covered surface, is demonstrated. Their optical properties are systematically interrogated and compared to citrate-reduced gold and silver nanoparticles with similar physical properties. The scattering properties are shown through the investigation of surface enhanced Raman scattering (SERS) responses and the absorption properties are illustrated by a study of their photothermal properties. The comparison results show that HGNs make superior substrates over standard solid nanoparticle substrates for SERS and photothermal applications in the NIR region and the detailed synthesis can be used to tune the LSPR to the required position allowing their activity to be maximized. A new nanostructure based on HGNs is also developed and the relationship between nanostructures and SERS activities is demonstrated by correlation of Raman maps and scanning electron microscopy (SEM). Finally, the combination of SERS and spatially offset Raman spectroscopy is used to demonstrate the potential *in vivo* applications by showing the successful detection of bisphosphonate functionalised SERS-active nanotags through 20 mm thick porcine muscle tissue. The work in this thesis not only provides insights into the interesting optical properties of hollow gold nanospheres, but also adds to the growing body of evidence in relation to nanostructures and surface enhancement of

Raman scattering and shows the promising future of applications of surface enhanced spatially offset Raman spectroscopy.

Contents

Chapter 1. General Introduction

Gold is chemically inert and relatively non-toxic compared to other heavy metals and is therefore very useful for biological applications. Gold nanoparticles (AuNPs) possess unique physical and chemical properties which make them excellent scaffolds for the fabrication of chemical and biological sensors.[1] First, the synthesis of AuNPs is straightforward and can be made highly stable.[2] Second, AuNPs have distinct optical properties which are being widely applied for surface enhanced optical techniques.[3] Third, they provide a high surface-to-volume ratio with excellent biocompatibility using appropriate ligands.[4] Finally, these properties of AuNPs can be tuned by varying sizes, shapes and surface chemistry.[2] These unique properties have allowed researchers to develop novel sensing strategies with improved sensitivity, stability and selectivity. In the following sections, gold nanoparticles and their derived structures will be introduced and their applications discussed.

1.1 Synthesis of Gold nanoparticles

Gold nanoparticles have a rich history in chemistry and the modern way of AuNP synthesis was discovered by Michael Faraday 150 years ago when he investigated the red colour of the colloidal nature of AuNPs.[5] High-yielding and reproducible methods for the synthesis of AuNPs with spherical and nonspherical shapes have been developed over the last half century.[4] Now, AuNPs from 1 nm to more than 200 nm can be obtained.

1.1.1 Citrate reduced preparation approach

In 1951, Turkevich *et al.* developed one of the most popular synthesis methods of Au NPs, using citrate reduction of $HAuCl_4$ in water.[6] In this approach, citric acid acts as both reducing and stabilizing agent (equation 1) and provides AuNPs with diameters of 20 nm.

$$6AuCl^-_4 + C_6H_8O_7 + 5H_2O \rightarrow 6CO_2 + 24Cl^- + 6Au^0 + 18H^+ \qquad 1$$

Further studies by G. Frens and colleagues enabled control over AuNP sizes by varying the feed ratio of gold salt to sodium citrate.[7] The kinetics of the Turkevich process was provided by Chow and Zukoski.[8] The biggest issue of this method is the polydispersity especially for particles larger than 40 nm. Recently, a two step synthesis has been developed providing a relatively monodispersed AuNPs with size larger 40 nm.[9] Generally, gold seeds with size ~15 nm are firstly synthesized using the citrate reduced method and then a further gold layer is deposited on the seeds in the presence of an excess amount of sodium citrate producing high quality large AuNPs.

1.1.2 The Brust–Schiffrin Method for Thiol-protected Au NPs

Brust and Schiffrin reported a two-phase synthetic strategy, using strong thiol–gold interactions to protect AuNPs with thiol ligands in 1994 which is a breakthrough in the field of AuNPs synthesis after the initial attempt from Mulvaney[10] of stabilizing AuNPs with alkanethiols.[11] $AuCl_4^-$ was transferred from the aqueous solution to toluene using tetraoctylammonium bromide as the phase-transfer reagent and reduced with aqueous sodium borohydride in the presence of dodecanethiol.[11] After the addition of sodium borohydride, the organic phase changes colour from orange to deep brown within a few seconds which produces AuNPs with the diameters in the range of 1-6 nm. These thiol-protected AuNPs feature superior stability because of the strong thiol–gold interaction and they can be easily handled, characterised, and functionalised. The nanoparticles can be thoroughly dried and then redispersed in organic solvents without any aggregation or decomposition.[1]

1.1.3 Other preparation methods

The previous two synthesis methods cover the range of gold nanoparticles from 1 nm up to 200 nm. Further manipulation of the structure of AuNPs can be achieved by physical methods. For example, thermolysis,[12] digestive ripening,[13] and conventional ripening[14] have significantly reduced average particle size and polydispersity and resulted in the formation of superlattices in 2D and 3D. The particle sizes and structures can also be modified by UV and laser irradiation.[1] Ultrasonic fields provide an approach to control the reduction rate of $AuCl_4^-$ in aqueous solutions and therefore affect core sizes with the intensity of the ultrasound and the reactor position.[15] Radiolysis is one of the other methods that can control the particle size.[16] Once formed, size-exclusion chromatography can separate suspended AuNPs by shape and size.[17]

1.2. Properties of gold nanoparticles

Metals such as gold have different optical properties compared to standard dielectrics because of the presence of free conduction electrons.[18] The free electrons of metals move in a background of fixed positive ions ensuring overall neutrality. This forms a *plasma* which can also be called a *free-electron plasma*.[19] The optical properties of metals are governed by the optical response of this free-electron plasma.[19] A *plasmon* is a quantum quasi-particle representing the elementary excitations of the charge density oscillations in a plasma and the *surface plasmon* is a mixed plasmon-photon mode.[19] When at the particular frequency (wavelength) of the incident light, the optical response (scattering and absorption) of the metal substrate is very large which is called *plasmon resonance*. While the metals come to the small objects in particular for nanoparticles, where the size is compatible or smaller than the excitation wavelength, the nature of the electromagnetic modes of the system is modified which results in *localised surface plasmon*.[19]

Gold nanoparticle suspensions show a very intense color, which is absent in the bulk material as well as in the individual atoms.[20] In the presence of an external light field, an electron gas that moves away from its equilibrium position is formed, creating induced surface polarization charges that act as a restoring force on the electron gas. (Figure 1) This results in collective oscillatory motion of the electrons characterized by a dominant resonance band (localized surface plasmon resonance) lying in the visible and near infrared for gold.[18]

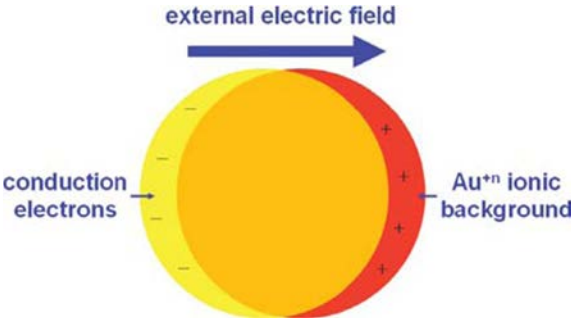

Figure 1. Schematic representation of a dipolar plasmon oscillation in a gold nanoparticle.[18]

Mie theory describes the extinction of metallic nanoparticles and specifies that the dielectric constant of the metal and the surrounding medium, as well as the size, shape and monodispersity of the nanoparticles all have an effect on the resultant spectrum.[21] The sensitivity of the localised surface plasmon resonance (LSPR) to changes in the local refractive index surrounding the nanoparticles that makes gold nanoparticles ideal candidates for biosensing.[4] In the following subsections, the general applications of gold nanoparticles are discussed.

1.2.1 Colourimetric detections

The aggregation of AuNPs of appropriate sizes ($d > 3$ nm) results in interparticle surface plasmon coupling, inducing a visible colour change from red to blue at nanomolar concentrations.[22] The colour change caused by the AuNP aggregation provides a practical platform for absorption-based colourimetric sensing of any target analyte that directly or indirectly triggers the AuNP aggregation or redispersion.

1.2.1.1 Detection of Oligonucleotides

In 1996, Mirkin *et al.* demonstrated the DNA-meditated AuNP assembly.[23] Fabrication of AuNPs functionalised with thiolated DNA strand makes it possible to tailor the optical, electronic and structural properties of the colloidal aggregates by using the specificity of DNA interactions to direct the interactions between particles of different size and composition.[23] This discovery has stimulated extensive use of oligonucleotide-directed AuNP aggregation for colourimetric detection of oligonucleotides and fabrication of structured assemblies.[1] In this approach, two single strand DNA-modified AuNP probes were used for colourimetric detection of target oligonucleotides. The base sequences in the AuNP probes were complementary to both ends of the target oligonucleotides (Figure 2). The presence of target oligonucleotides induced the aggregation of AuNPs with concomitant colour change as a result of hybridization of the DNA strand. Highly specific base-pairing of DNA strands coupled with the intense absorptivity of AuNPs enabled the subpicomolar quantitative colourimetric detection of oligonucleotides.[1]

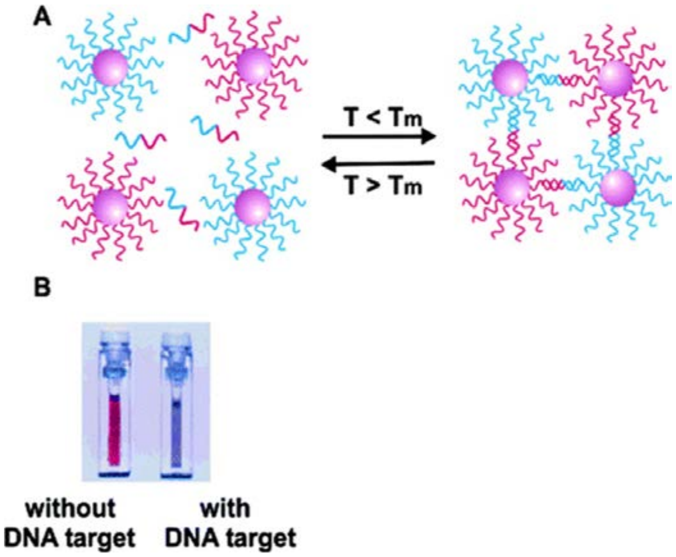

Figure 2 Aggregation of oligonucleotide AuNPs in presence of complementary target DNA (A), leading to change in color of solution from red to blue (B).[24]

Recently, a novel sensing strategy using single-stranded probe DNA, unmodified gold nanoparticles, and a positive charged, water-soluble conjugated polyelectrolyte to detect a broad range of targets including nucleic acid (DNA) sequences, proteins, small molecules, and inorganic ions was reported by Xia *et al.*.[25] This is a nearly "universal" biosensor approach which significantly extents the colourimetric method.

1.2.1.2 Assays for cations

The contamination of Hg^{2+} in water and soil will transform into methyl mercury to accumulate in human body through the food chain which may damage many organs.[26] The detections of Hg^{2+} based on AuNPs have significantly developed in the past decade. The most important example is based on DNA-conjugated AuNPs.[27,28] Hg^{2+} -induced complexation of ligands such as short single-stranded DNA or double-stranded DNA from the surfaces of AuNPs can cause the aggregation of AuNPs, which can be used to detect Hg^{2+}. Single-stranded DNA with thymine-rich (T-rich) domains can absorb onto the surfaces of unmodified AuNPs. The functionalized AuNPs are monodispersed in aqueous media due to the electrostatic repulsion between the nucleic acid. Upon the addition of Hg^{2+}, the complexation of Hg^{2+} with T-rich domains induces aggregation of AuNPs causing the color change. The system utilizes a combination of oligonucleotides and NPs at low concentrations, which readily detects Hg^{2+} in aqueous solutions and in the presence of an excess of other metal ions with the detection limit of sub-10nM.[28] The method can also be modified for the detection of other metal ions by replacing natural DNA bases with metal-dependent synthetic artificial bases.[29]

1.2.1.3 Detection of proteins

Many disease states are usually linked with the presence of certain biomarker proteins or irregular protein concentrations. AuNPs have been successfully applied for colorimetric detection of proteins.[1] The detection of carbohydrate binding proteins has been achieved from a diverse range of carbohydrate functionalized AuNPs.[1] For example, Kataoka *et al.* utilized the aggregation of β-D-lactopyranoside (Lac)-functionalized AuNPs for the detection of Recinus communis agglutinin.[30] The degree of colloidal aggregation was proportional to the protein concentration, allowing the quantitative detection of lectin.

In an aptamer-based method, platelet-derived growth factors (PDGFs) specific aptamer functionalised AuNPs were used to detect PDGFs by monitoring the changes in the colour and extinction of the aptamer-AuNPs that occur as a result of aggregation.[31] In addition, a general antigen-antibody interaction has also been employed for the AuNP aggregation-based immunoassay for proteins.[32] Using this method, a detection limit of 2 μg/mL of antiprotein in serum samples has been achieved by Rosenzweig *et al.*.[33]

1.2.2 Fluorescence-based assays

Fluorescence resonance energy transfer (FRET) is a nonradioactive process and it usually occurs over the distances of 10Å to 100 Å which is comparable to the dimensions of most biological macromolecules.[34] FRET happens between an excited state donor D (usually a fluorophore) and a proximal ground state acceptor A through long-range dipole–dipole interactions (Figure 3). The emission spectrum of the donor and the absorption spectrum of acceptor must overlap, but the acceptor does not necessarily have to re-emit the energy fluorescently itself (i.e. dark quenching). The rate of energy transfer is not only dependent on the distance between the donor and acceptor molecules, but also on many other factors, such as the extent of spectral overlap, and the relative orientation of the transition dipoles.[34]

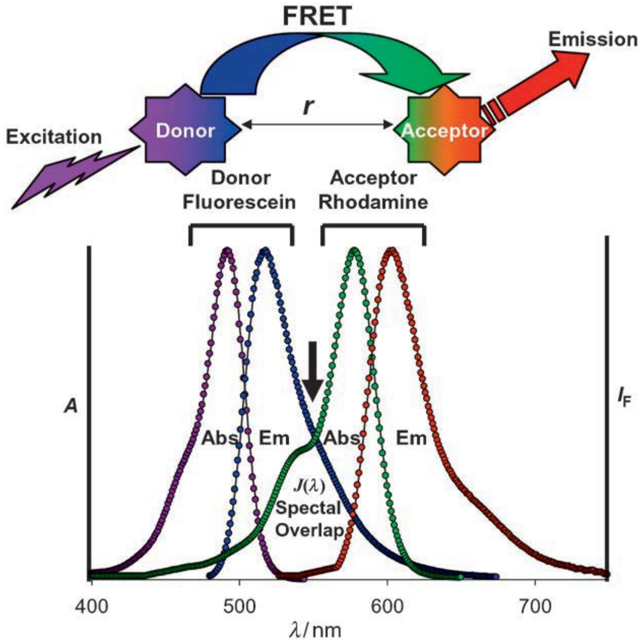

Figure 3 Schematic of the FRET mechanism.[34]

AuNPs can serve as excellent fluorescence quenchers for FRET-based assays due to their extraordinary high molar extinction coefficients and broad energy bandwidth.[1] Murray and co-workers have reported a FRET based assay for the detection of various metal ions including K^+ and Ca^{2+}.[35] This quenching system has also been employed in Hg^{2+} sensing.[36] For example, highly fluorescent rhodamine B

(RB) molecules would be quenched when they are adsorbed onto AuNP surfaces. In the presence of metal ions such as Hg^{2+}, RB molecules are released from the AuNP surface and therefore restore the florescence of RB.[36] Under the optimum conditions, the selectivity of this system for Hg^{2+} over other metal ions in aqueous solutions is remarkably high, and a 2.0 ppb limit of detection for Hg^{2+} in the matrix pond water is achieved.[36] Besides the detection of metal ions, FRET based AuNP assays were utilized for sensing small organic molecules like thiols at submicromolar levels.[37] Hairpin FRET-based systems for sensing DNA have been created by labeling molecular beacons with AuNPs.[38] The nucleic acid probe modified with the organic dye is self-complementary, forming the hairpin structure on AuNP with effective FRET fluorescence quenching. The hairpin structure changes to rodlike through complementary hybridization with the target DNA, resulting in an increase in fluorescence of the dye.[38] By utilizing the similar principle, Nie *et al.* have shown that fluorophore-modified oligonucleotides labeled on small AuNPs (2.5 nm) can spontaneously assemble into a constrained arch-like conformation. Binding of target molecules results in a conformational change, which restores the fluorescence of the quenched fluorophore.[39]

In addition to the hairpin FRET-based systems, another similar detection strategy based on DNA hybridizations is also widely used. Hybridization of dye-modified DNA reporter sequences with oligonucleotide-functionalised AuNPs quenches fluorescence of the reporter. The presence of a target then displaces and releases the reporter from AuNPs by forming more stable duplex between the target and the oligonucleotide on AuNPs. For example, Mirkin *et al.* have developed AuNP probes, (nanoflares) which are designed to detect and quantify intracellular analytes, such as mRNA in cells.[40-42]

Besides normal fluorophores, semiconductor quantum dots (QDs) have also been used for FRET-based AuNPs assays for detection of proteins.[43] For example, a fluorescent competitive assay for DNA identification using QDs and AuNPs have been reported by Malvin *et al.*.[44] AuNPs were assembled with CdSe QDs through short DNA strands, causing fluorescence quenching of the CdSe QDs.[44] Addition of complementary oligonucleotides then displaces the AuNP-DNA from the QD-DNA, resulting in QD fluorescence restoration.

1.2.3 Localised surface plasmon resonance (LSPR) sensing

The most common method for LSPR sensing is the wavelength-shift measurement, in which the change in the maximum (or minimum) of the LSPR extinction curve is monitored as a function of changes in the local dielectric environment caused by analyte adsorption.[45] LSPR assays have been conducted both in solution phase and on surfaces coated with nanoparticle monolayers.[1] In the case of solution phase, the LSPR of AuNPs was red-shifted when functionalized with monoclonal antibodies interacted with analytes.[46] Moreover, the wavelength shift was found to be proportional to the amount of ligands.[46] However, most AuNP-based LSPR sensors have been fabricated by immobilizing nanoparticles onto surface.[1] Owing to the high dielectric constants of AuNPs and the electromagnetic coupling between AuNPs and the metal film on the surface, the introduction of AuNPs onto the sensing surface provides an effective way to increase the sensitivity of SPR sensors.[47] For example, a gold film-coated chip was used to detect dopamine in nanomolar concentration by immobilizing a molecularly imprinted polymer gel with embedded AuNPs.[48] Various substrates, such as quartz, optical fibers, ITO glass, sol–gel matrix, etc., have been used for supports for AuNPs, allowing the detection of numerous analytes such as human serum albumin, BSA, human IgG, streptavidin, interleukin-1β, propanethiol *etc.*.[1]

Based on Mie's theory, nanoparticles with same composition but different sizes or shapes will generate different optical responses due to their different localised surface plasmon oscillation. In the next section, several recently developed nanomaterials based on gold are introduced.

1.3 Gold nanorods

Gold nanorods have promising applications in the fields of drug delivery and photothermal therapy. These promises come from their unique optical and photothermal properties, the availability of synthetic protocols that can tune the size and shape of the particles, the ability to modify the surface and conjugate drugs/molecules to the nanorods, and the relative biocompatibility of gold nanorods.[49]

1.3.1 Synthesis of gold nanorods

The growth of gold nanorods is, within the field of anisotropic nanoparticle synthesis, the most established protocol, in terms of the degree of control of the size, shape and monodispersity.[2] Of the reported procedures for gold rod formation, seed mediated growth has been by far the most efficient and popular approach.[50] (Figure 4) The original idea was that cationic surfactant micelles could serve as a ‘‘soft template’’ for directing nanoparticle growth and could additionally provide colloidal stability for the synthesized nanoparticles. The role of the seed particles is also critical. Furthermore, the presence of small amounts of silver nitrate during the synthesis has a dramatic effect on the final shape and crystalline structure of the particles.[2]

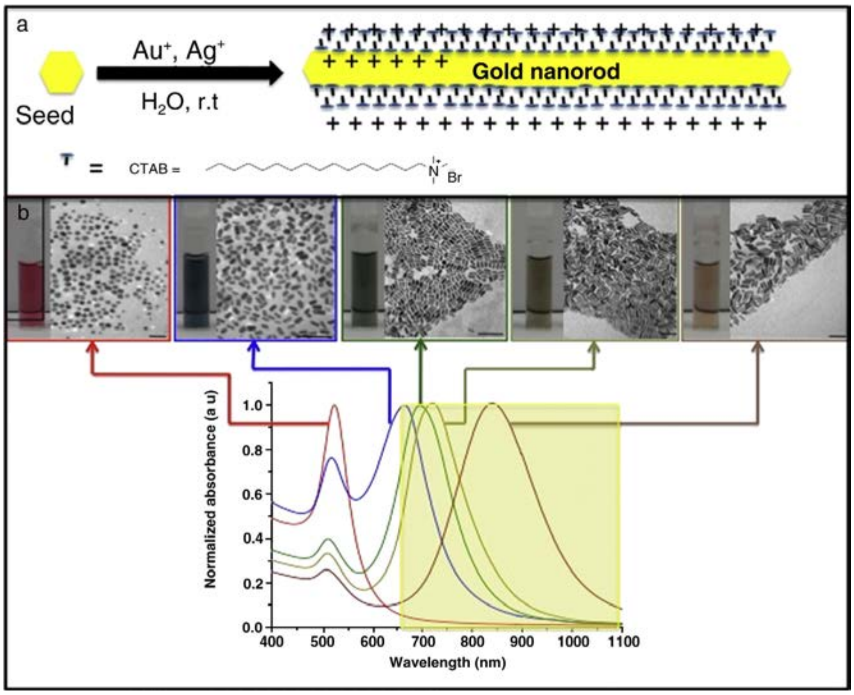

Figure 4 a. Synthesis of gold nanorods from spherical gold seeds in the presence of CTAB as a shape-directing agent in water at room temperature. b: UV–Vis spectra, transmission electron micrographs, and photographs of aqueous solutions of gold nanorods of different aspect ratio (length/width). Aspect ratio increases from left to right. All scale bars=100 nm. The yellow shaded area of the spectra is the biological “water window”.[49]

1.3.2 Properties of gold nanorods

For gold nanorods, the LSPR band is split into two, corresponding to a transverse (short axis) band and a longitudinal (long axis) band, whose position depends on the aspect ratio (length/width) of the particles.(Figure 4) The ability to tune the optical absorption and scattering through the vis-NIR region which is widely considered to be the best spectral region for imaging and therapy[51] for gold nanorods provides an inherent advantage over their spherical gold nanoparticle counterparts, which absorb only in the visible region. Here, two most important applications of gold nanorods are featured.

Upon NIR irradiation into the LSPR bands of gold nanorods, the excited conduction band electrons decay to the ground state by releasing their energy as heat to the surrounding medium; thus gold nanorods can be considered “nanoheaters”.[49] This photothermal effect is the fundamental basis for the potential therapeutic applications of gold nanorods themselves, in addition to any delivery capability they may have for small drug molecules. It has been reported that the temperature increases range from ~10 °C to nearly 100 °C, depending on laser power, time of irradiation, and concentration of gold nanorods in the spot size of the laser.[49]

Gold nanorods have been used as contrast agents via laser optoacoustic imaging in live mice.[52] Gold nanorods were injected deeply into a mouse, and irradiated with a pulsed near-infrared laser which is resonant with the longitudinal LSPR band of the nanorods. Energy absorbed by the nanorods was released to the environment as heat, which thermoelastically expanded the tissue and generated acousticwaves, which were measured at ultrasound frequencies at various positions and times around the animal.[52] The ability to detect Au-NRs at a very low concentration deep within a tissue using optoacoustic methods, along with the fact that Au-NRs can be attached to vehicles such as monoclonal antibodies to target cancer cells, is promising in the development of new diagnostic modalities that employ optoacoustic methods targeting Au-NRs as molecular-specific contrast agents for the early detection of cancer.[52]

1.4 Gold nanocages

Gold nanocages comprise a novel class of nanostructures possessing hollow interiors and porous walls. Due to their unique structure and related optical properties, gold nanocages have been extensively used for drug deliveries[53] and photothermal therapies[54].

1.4.1 Synthesis of gold nanocages

The galvanic replacement reaction represents a simple mean of preparing multi metal hollow structures. The electrochemical potential difference between two metals drives the reaction, with one serving as the cathode and the other as the anode.[55] In the case of the preparation of Au-based nanocages, the reduction potential of $AuCl_4/Au$ (0.99 V vs SHE) is more positive than that of AgCl/Ag (0.22 V vs SHE).[55] Thus, Ag nanocubes prepared by polyol reduction[56] can serve as a template for reaction, being oxidized by $HAuCl_4$ according to

$$3Ag_{(s)} + HAuCl_4 \longrightarrow Au_{(s)} + 3AgCl_{(s)} + HCl_{(aq)} \qquad 2$$

The produced Au is confined to the nanocube surface, growing on it and adopting its morphology, as interior Ag is oxidized to produce a hollow structure. In principle, this Ag template-engaged replacement reaction can be applied to any metal whose redox potential is more positive than the AgCl/Ag pair, although morphology differences have been observed in other systems.[56] The synthesis schematic and TEM images of precursors and final products are shown in Figure 5.

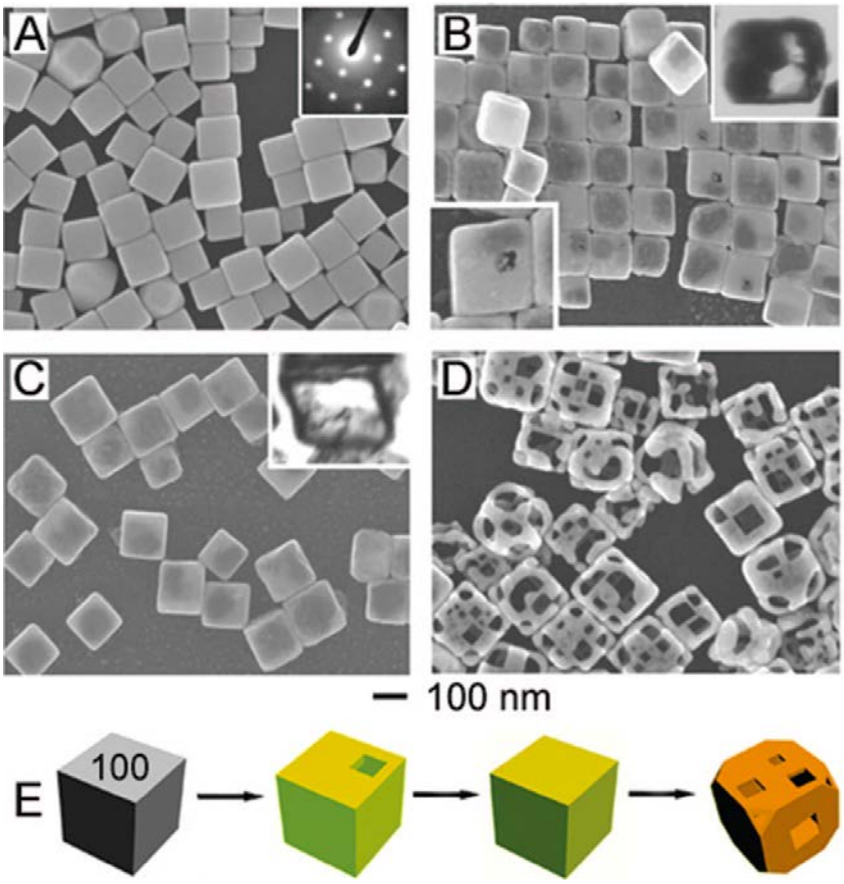

Figure 5 (A) SEM image of Ag nanocubes; electron diffraction (inset) indicates that they are single crystals. (B) SEM image of product after 0.30 mL of 1 mM $HAuCl_4$ solution was added to a 5 mL of 0.8 mM Ag nanocube suspension; a pinhole (lower inset) is observed on the exposed face of ∼1 in 6 nanocubes and TEM image (upper inset) of a microtomed sample reveals early hollowing out. (C) SEM image of product after 0.50 mL of $HAuCl_4$ solution was added; TEM image (inset) of a microtomed sample reveals the hollow interior of the nanobox. (D) SEM image of product after 2.25 mL of $HAuCl_4$ solution was added; porous nanocages were produced. (E) Illustration summarizing morphological changes. Coloration indicates the conversion of a Ag nanocube into a Au/Ag nanobox then a predominately Au nanocage.[55]

1.4.2 Properties of gold nanocages

By changing the amount of $AuCl_4^-$ and silver during the galvanic reaction, the morphology and LSPR of gold nanocages can be tuned.[56] They have been used for targeting cancer cells,[57] contrast enhanced agents through photoacoustic tomography (PAT),[58] drug carriers[53] and photothermal therapies.[54] Recently, Xia *et al.* developed a smart drug carrier based on gold nanocages for controlled release with NIR-light.[59] In principle, gold nanocages were firstly loaded with a model drug and then functionalised with thermoresponsive polymers. At the normal human body temperature, the polymers block the pores on the cage surface to prevent releasing loaded drugs. Once these nanoparticles are illuminated by NIR light, the heat generated by the photothermal effects of nanocages will cause the change of the polymer morphology and release the drugs from the cages.[59]

1.5 Hollow gold nanoparticles

Very recently a new metal nanostructure with strong NIR localised surface plasmon resonances (LSPRs) consisting of high quality nanoshells with small size and spherical shape has been developed and termed hollow gold nanospheres (HGNs).[60]

1.5.1 Synthesis of hollow gold nanospheres

Figure 6 shows a schematic of the synthesis. Cobalt nanoparticles are formed in the presence of $NaBH_4$ which reduces Co^{2+} to Co^0. Gold shells are then grown onto these Co nanoparticles via galvanic reaction introduced in the last section. The solution is finally exposed to air and the oxygen sensitive Co nanoparticles are removed forming a hollow structure. Co nanoparticles were used as sacrificial templates for the synthesis of hollow gold nanospheres. The quality of the resultant HGNs highly depends on the quality of the starting Co nanoparticles which are very sensitive to oxygen. The size of the Co nanoparticles correlates to the inner diameter of the HGNs and this is tuned by changing the amount of sodium citrate while the shell thickness is controlled by altering the amount of Au^{3+} ions present. This results localized surface plasmon resonance of HGNs in the region of 550–820 nm shown in Figure 7.[60]

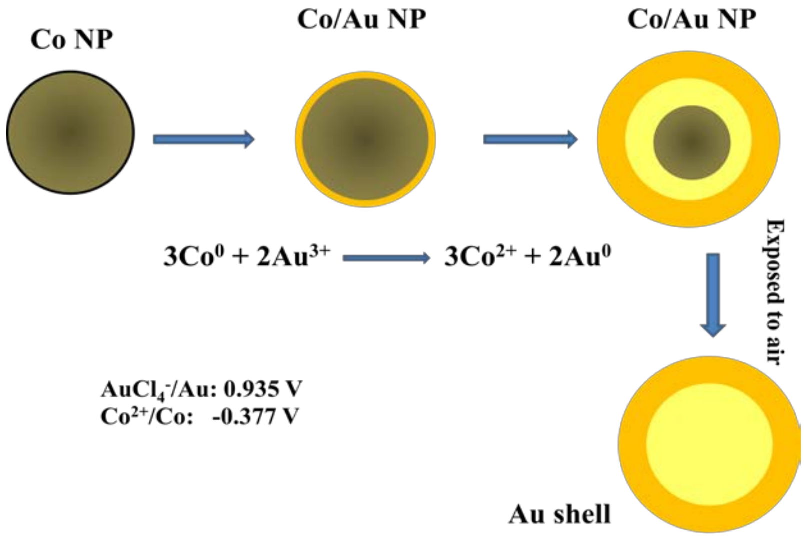

Figure 6. Schematic of HGN synthesis process. Reproduced from ref.60.

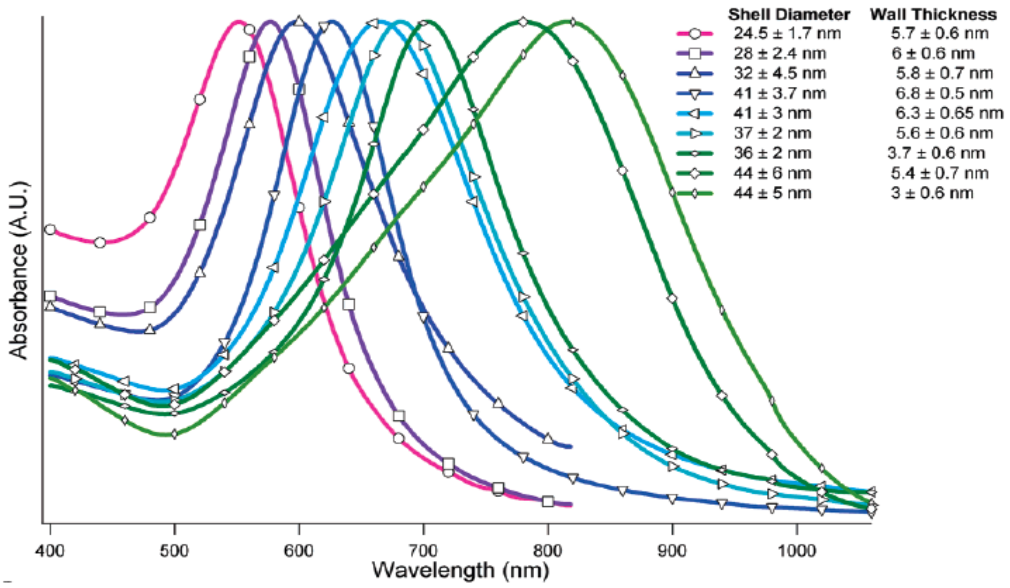

Figure 7. UV−visible absorption spectra of nine HGN samples with varying diameters and wall thicknesses.[60]

Like a normal gold nanoparticle, the LSPR bandwidth of HGN depends on the uniformity of the particle diameter and shell thickness, and poorer uniformity results in broader spectral width. This synthesis must be carefully controlled to make high-quality HGNs, especially those with a LSPR in the NIR region. One critical factor is the removal of O_2 before and during the reaction using Ar or N_2 gases.[61] The further discussion of the synthesis is shown in section 2.3.1.

1.5. 2 Applications of hollow gold nanospheres

Due to their optical properties and small sizes (usually from 30 to 60 nm), HGNs have been used for pH sensing,[62] SERS imaging of cancer markers in single cells,[63] on-chip immunoassays,[64] and as a DNA biosensor.[65] They also have been successfully utilized for both *in vitro* and *in vivo* photothermal ablation therapy (PTA) of carcinoma and melanoma cancer cells.[66,67] Figure 8 demonstrates the principle behind PTA. HGNs are actively linked to target cancer cells though antibody (Ab)-antigen (Ag) or ligand (e.g., hormone)-receptor interaction. Heat (represented by the symbol Δ) generated from light illumination of the HGNs is used for thermal imaging and/or destroying of the cancer cells.[61] Using a small molecular weight peptide as a targeting ligand and attaching it at the end of PEG chains, receptor-mediated active targeting of melanoma and efficient PTA with photothermal coupling agents *in vivo* have been shown for the first time.[66]

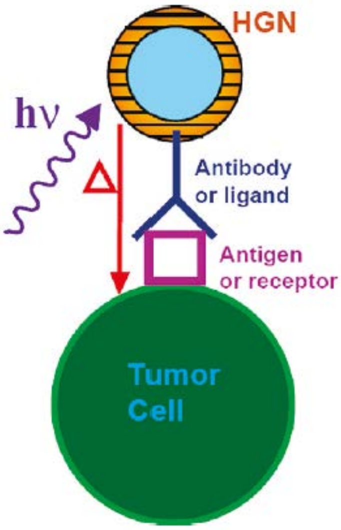

Figure 8. Illustration of the principle of PTA. HGNs were firstly functionalized with specific targeting groups for tumor cells and then heat generated by the conversion of the illumination light selectively killed the malignant tumor cells. [61]

1.6. Characterisation of nanoparticles

1.6.1. UV-Visible-Near infrared (Extinction) spectroscopy[68]

UV-Visible-Near infrared spectroscopy provides two important pieces of information. Firstly, the information on the energy of the electronic excitation is indicated by the position of absorption (λ_{max}). Secondly, it provides the information of molar extinction coefficient (ε). This value is constant for a given molecule at the given wavelength and it is the measure of the ease of the transition caused by the absorption of the radiation. The Beer-Lambert Law links the molar extinction coefficient (ε) and the concentration of the chromophore (c) and is described as: $\varepsilon = A/cl$ where A is the absorption value at the particular wavelength and l is the distance the light travels through the material.[69] Importantly, regarding the characterizations of nanoparticles, it also indirectly provides the information of sizes of various nanoparticles. The extinction spectrum is the combination of scattering and absorption properties of the sample. For organic molecules such as dyes and DNA, the scattering effect is extremely weak and normally can be ignored. However, in the case of gold nanoparticles, it highly depends on the sizes. AuNPs with a diameter smaller than 20 nm essentially show absorption, but as the size increases to 80 nm, the ratio of scattering to absorption also increases which is required for biological imaging based on light scattering.[5]

1.6.2. Zeta potential[70]

Zeta potential is the potential difference between the dispersion medium and the stationary layer of fluid attached to the dispersed particle. The value of zeta potential indicates the stability of colloidal suspensions. It gives the information of the degree of repulsion between adjacent, similarly charged particles in a suspension. A high zeta potential will be considered as a stable suspension which will resist aggregation. When the potential is low, (between 0 and ±5 mV) attraction exceeds repulsion and the nanoparticle suspension will break and flocculate. Therefore, colloids with high zeta potential (negative or positive) are electrically stabilized while colloids with low zeta potentials tend to coagulate or flocculate.

1.6.3. Dark-field Microscopy[71]

Dark-field Microscopy only collects the scattered light from the samples which excludes unscattered beam from the image which creates a general dark background for unscattered environment. Dark-field microscopy has been widely used for imaging live and unstained biological samples, such as a smear from a tissue culture or individual water-borne single-celled organisms. As mentioned above, noble nanoparticles scatter light creating “shinny” spots in the images which also makes dark-field microscopy useful for preliminary optical characterizations.

1.6.4. Scanning Electron Microscopy (SEM)[72]

SEM generates images by scanning a focused electron beam across the surface of a sample. The electron beam interacts with the sample producing signals that contain information about the sample's surface topography, composition, and other properties such as electrical conductivity.

1.6.5. Transmission Electron Microscopy (TEM)[73]

TEM is a technique whereby an electron beam is transmitted through an ultra thin sample, interacting with the sample as it passes through. An image is formed from the interaction of the electrons transmitted through the sample and magnified and focused onto a CCD camera. TEM provides the ability of imaging at a significantly higher resolution than light microscopes enabling the examination of fine detail such as atomic arrays and diffraction information if the ordered structures involve crystals.

1.6.6. Electron Energy Loss Spectroscopy (EELS)[74]

The basic mechanism of the electron energy loss spectroscopy (EELS) is to expose a material to a beam of electrons with a known, narrow range of kinetic energies. The inelastic scattering of some electrons means that they lose energy and have their paths slightly and randomly deflected. The amount of energy loss can be measured via an electron spectrometer and interpreted in terms of what caused the energy loss. The inner-shell ionizations which is one of the inelastic interactions are particularly useful for the detection of the elemental components of a material. Looking at a wide range of energy losses, the types of atoms, and the numbers of atoms of each type, being struck by the beam can be determined. The scattering angle (the amount that the path of the electron is deflected) can also be measured, giving information about the dispersion relation of whatever material excitation caused the inelastic scattering.

1.7. Raman spectroscopy

1.7.1 History of Raman Scattering

In 1921, Raman scattering was discovered by Chandrasekhara Venkata Raman in India.[75] It is interesting to note that Raman used a very rudimentary optical tool, the sun as a light source and his eyes as a detector to observe the effect. Importantly, what he observed is what we call today “anti-Stokes Raman scattering”, which is normally quite weak. In the case of anti-Stokes Raman scattering, the scattered photons have an energy that is larger than the incoming ones (following interaction with an excitation already present in the sample). In fact, it was this up-conversion process in energy that convinced Raman that he was in the presence of a new optical scattering phenomenon. The "up-conversion" Raman observed by eye in several organic liquids[75] implied an inelastic scattering process, which is what we now call the Raman scattering. The measurement and analysis of the signals (photons) arising from the Raman effect is called Raman spectroscopy.

1.7.2 Raman scattering and Raman spectrum

Raman scattering is a form of vibrational spectroscopy and is concerned with the inelastic scattering of light from a molecule. It differs from the majority of light scattered by molecules which is termed Rayleigh scattering; an elastic process that does not induce any molecular energy changes. For Raman scattering, if the scattered photon has less energy than the incident photon ($E_S < E_L$), then the molecule is excited to a higher-energy level by E_L - E_S which is called a Stokes process; if on the contrary, the scattered photon has more energy than the incident photon ($E_S > E_L$), then the molecule has relaxed from an excited vibrational state to its ground state and the energy of the vibration is given as E_S - E_L which is called an anti-Stokes process. (Figure 9)

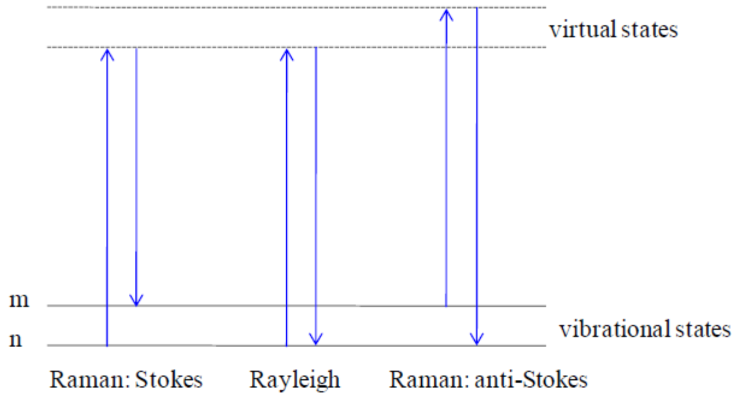

Figure 9 Vibrational transitions involved in light scattering.

The energy lost by the photons in the scattering event is called the Raman shift and is denoted in energy as $\Delta E_R = E_L - E_S$. It is therefore positive for a Stokes and negative for an anti-Stokes process. Raman shifts are commonly expressed in wave-numbers and will then be denoted Δv_R (usually in units of [cm^{-1}]).[19]

The Raman spectrum corresponds to the wavelength- (or energy-) dependence of the Raman scattered intensity at a given incident wavelength. It is commonly shown as Raman intensity as a function of Raman shift (rather than wavelength), as shown in Figure 10 for an example of a Raman spectrum. Peaks in the Raman spectrum correspond to vibrational modes of the molecule, in a similar fashion as for an infrared absorption spectrum. The Raman shift of a peak is equal to the vibrational energy of the corresponding mode. There is some broadening (homogeneous and inhomogeneous) of the peaks, but Raman peaks for molecular compounds are typically narrow (5-20 cm^{-1}).[19] The total intensity (power) scattered by a given vibrational mode is therefore the integrated intensity of the corresponding Raman peak.[19]

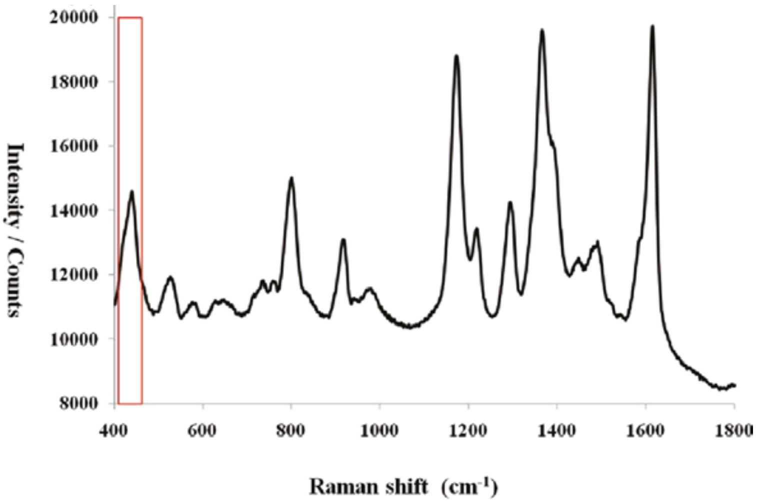

Figure 10 A typical Raman (in fact SERS) spectrum of malachite green at 633 nm excitation.

1.7.2.1 Raman polarizability[76]

The lasers that are normally used for excitation in Raman scattering are usually at least partially polarized. When a photon interacts with a molecule, the electron cloud is distorted by an amount that depends on the ability of the electrons to polarize (i.e. the polarizability, α). The light causing the effect is polarized in one plane, but the effect on the electron cloud is in all directions. This can be described as a dipole change in the molecule in each of the three Cartesian co-ordinates x, y and z. Thus, to describe the effect on molecular polarizability of an interaction with linearly polarized radiation, three dipoles require to be considered. The simple expression is that a dipole μ is created in the molecule by the field from the incident photon E.

$$\mu=\alpha E \qquad 3$$

To allow for the polarization angle of the linearly polarized light, the polarizability components of the molecule are usually labelled, for example α_{xx}.

The first subscript x refers to the direction of polarisability of the molecule, and the second x refers to the polarization of the incident light. Thus, $\mu_x=\alpha_{xx}E_x+ \alpha_{xy}E_y+ \alpha_{xz}E_z$. Similar expressions will exist for both μ_y and μ_z.

Thus, the polarizability of the molecule is a tensor,

$$\begin{bmatrix} \mu_x \\ \mu_y \\ \mu_z \end{bmatrix} = \begin{bmatrix} \alpha_{xx} & \alpha_{xy} & \alpha_{xz} \\ \alpha_{yx} & \alpha_{yy} & \alpha_{yz} \\ \alpha_{zx} & \alpha_{zy} & \alpha_{zz} \end{bmatrix} \begin{bmatrix} E_x \\ E_y \\ E_z \end{bmatrix}$$

In Raman scattering the incident and scattered beams are related. If radiation of a particular polarization is used to create the Raman scattering, the polarization of the scattered beam is related to but not necessarily the same as that of the incident beam.

1.8 Surface enhanced Raman scattering

One in every 10^6-10^8 photons involves a change in energy and is termed Raman scattering.[19] Therefore, Raman scattering is an intrinsic weak effect. Surface enhanced Raman scattering (SERS) effect is about amplifying Raman signals by several orders of magnitude and is an ultra-sensitive vibrational spectroscopic technique that can be used for the detection of molecules on or in close proximity to the surface of metal nanostructures.[77] Generally, the detection limits of SERS are at least compatible with the rival optical spectroscopic technique of fluorescence.[78] However the vibrational nature of SERS means that identification of the components of a mixture without separation is superior to fluorescence. For example, six labelled oligonucleotides can be detected in solution without separation of the individual species using SERS as reported by Faulds *et al.*.[79]

SERS is purely a nanoscale effect and there are two main factors that account for this effect, one is the electromagnetic enhanced mechanism (EM) and the other is the chemical enhancement mechanism (CE).[80] Electromagnetic enhancement applies to all analytes, while chemical enhancement is probe-dependent and in general requires chemical bonding of the analyte to the metallic nanoparticle surface and therefore, in this section, we will focus on the EM mechanism and briefly introduce the CE mechanism.

1.8.1 Electromagnetic Enhancement Mechanism

Under the excitation of a laser source at a frequency ω_L, the electric field E_{In} at the molecule position induces a Raman dipole $\mu_{ind}=\alpha\ E_{In}$ where α is Raman polarizability tensor, oscillating at the Raman frequency ω_R. This oscillating Raman dipole radiates a power proportional to $|\mu_{ind}|^2$ at frequency ω_R and in fact the Raman signal we detect is this radiation.[19] These processes will be affected in a number of ways when the noble nanopartilces (Au or Ag) present.

Firstly, the amplitude of the electromagnetic field at the molecule position can be dramatically enhanced which results in a strong local field enhancement. This is particularly true when the excitation wavelength λ_L is close to the localised surface plasmon resonances of nanoparticles. Therefore, the electric field E_{LOC} at molecule position is very different to the incident field E_{In} and the magnitude $|E_{LOC}|$ on the metallic nanoparticle surface is much larger than $|E_{In}|$. The local field induces a Raman dipole $\mu_{ind}=\alpha\ E_{LOC}(\omega_L)$ whose magnitude is enhanced by a factor of $|E_{LOC}(\omega_L)|/|E_{In}|$. Therefore, the energy radiated which is proportional to $|\mu_{ind}|^2$ is enhanced by a factor of $|E_{LOC}(\omega_L)|^2/|E_{In}|^2$.[19]

Secondly, the radiation properties of the Raman dipole μ_{ind} are modified which results in a radiation enhancement. And as mentioned above, it can be concluded that is this case, the energy radiated is also enhanced by a factor of $|E_{LOC}(\omega_R)|^2/|E_{In}|^2$.[19]

Thirdly, the Raman tensor α may be modified. However, this modification is typically classified as the chemical enhancement which is discussed in section 1.8.2.[19]

If only two main mechanisms of enhancement which are local field enhancement and radiation enhancement are considered, the overall SERS EM enhancement for a single molecule can be simply expressed as:

$$\mathrm{SMEF}(\omega_L, \omega_R) \approx \frac{|E_{LOC}(\omega_L)|^2}{|E_{In}|^2} \times \frac{|E_{LOC}(\omega_R)|^2}{|E_{In}|^2} \quad 4$$

In many cases, the Raman shift is also small and we can make a further approximation that $\omega_R \approx \omega_L$. Therefore, for zero-Stokes shift, the equation is simplified as:

$$\mathrm{SMEF}(\omega_L) \approx \frac{|E_{LOC}(\omega_L)|^4}{|E_{In}|^4} \quad 5$$

1.8.1.1. Electromagnetic couplings

The previous section discussed the electromagnetic (EM) enhancements of single metallic nanoparticles. Here, the EM enhancements that arise from the interaction of two or more nanoparticles is discussed. The interaction becomes particularly important when nanoparticles are close enough, together to generate large local fields with a single molecule enhanced factor (SMEF) value up to 10^{11}.[81] The interaction between the two nanoparticles creates new localised surface plasmon resonances (LSPRs) which are the result of the coupling of the individual LSPRs of isolated nanoparticles. The most red-shifted resonance is usually the most important one for SERS which arises from the dipolar coupling between two or more single nanoparticle dipolar LSPRs.[45] This coupled LSPR is very sensitive to the exact gap size; a change of ~ 1 nm can result in a large difference in the resonance wavelength.[45]

The most important aspect of coupled LSPR is not the position or the red shifted effect but the generation of the extremely large local field enhancements in particular at the gap between two nanoparticles, the so called “hot spot”. The enhancement factor (EF) of SERS at the hot spot is very large with up to ~ 5×10^{11} [81] and the magnitude of the SERS EF is also highly sensitive to the gap size. The highest EF is obtained at the smallest gap between two nanoparticles. [82] However, the extinction spectrum only reflects the position of the resonances but not the magnitude of the SERS EF.[83] It is impossible to infer the SERS EF from an extinction measurement in the presence of interacting particles which points out the fundamental differences between far-field and local-field properties.[19]

Recently, the group from Van Duyne found that SERS EFs do not correlate with aggregation state, meaning that a single hot spot between two particles is sufficient, and the “extra” particles are not contributing significantly to the SERS signal.[84] In addition, based on the finite element method (FEM) calculations, the hot spot with the smallest interparticle gap size dominates the overall enhancement. In contrast to what has been observed for isolated nanoparticles,[85] no direct correlation between LSPR wavelength and EF is observed.[84]

1.8.2 Chemical enhancement

Charge-transfer mechanism is the most studied mechanism for chemical enhancement. This mechanism is illustrated in Figure 11.

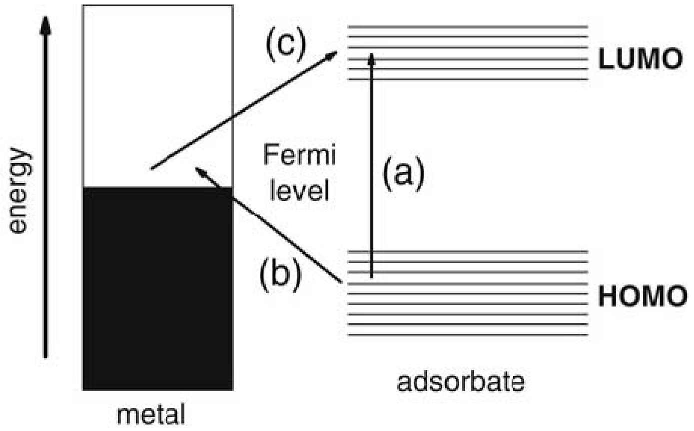

Figure 11 Schematic of a charge-transfer mechanism in the SERS cross-section, appearing as a “resonant contribution” to the measured intensity. The laser energy can be directly in resonance with an electronic transition of the molecule-metal complex (case (a)), or can profit from an indirect coupling (charge transfer)through the metal ((b) + (c)).[19]

It contains the presence of a surface complex either by direct (covalent) binding to the metal or by indirect binding with the assistance of an electrolyte ion (typically chloride).[19] This may create a substantial change in the intrinsic polarizability of the molecule. It is important to realize that the magnitude of the polarizability depends explicitly on the available optical transitions. The “new” indirect transitions provided by the overlap of molecular orbitals give a channel for the modification of polarizability. It is also possible that the surface complex creates a new electronic state that is explicitly in resonance or close to resonance with the laser, hence providing a contribution to the enhancement of a resonant- Raman type.[19]

1.8.3 Surface enhanced resonance Raman scattering (SERRS)

Raman scattering is particularly strong for molecules (dyes) with electronic energies close to the laser excitation which results in resonance Raman scattering (RRS). When these molecules are imobilised on the metal suface, and excited by a resonant laser excitation, an enhancement up to 10^{14} can be achieved compared to normal Raman measurement.[86] The generation of SERRS invovles several steps. Firstly, a chromophore or fluorescent dye adsorbed onto a roughened metal surface and the fluorescence of chromophore or dye will be quenched by the metal surface.[78] Then, a suitable laser coincident with the absorption maximum of the chromophore or dye is chosen to exite the molecule. Therefore the presence of a chromophore or dye gives the contribution of resonance and an extra enhancement can be obtained.[78] However, the main enhancement mechanisms between SERS and SERRS are the same. Therefore, we will not make this distinction in the rest of this thesis.

1.9. Aims of this thesis

The near infrared (NIR) region provides a relatively transparent optical sensing window for bioimaging due to the minimized absorption and scattering effects of tissues in this range. Hollow gold nanospheres (HGNs) demonstrate a tunable localised surface plasmon resonance ranging from the visible to near infrared consisting of high quality nanoshells with small size and spherical shape. However, the reproducibility of the synthesis is a large issue especially for HGNs with LSPRs in the NIR region. Also, the optical properties of these nanostructures are yet to be elucidated. Therefore, in the first part of this thesis, this problem is investigated and use of various optical techniques to characterise the optical properties of these nanoshperes is reported. In addition, use of the newly developed nanostructures consisting of connected HGNs to demonstrate the relationship between nanostructures and surface enhanced Raman scattering is also reported.

Currently, even with an optimized set-up, the depth of penetration (less than 10 mm) remains an obstacle for most *in vivo* SERS applications. In the last part of this thesis, spatially offset Raman spectroscopy is combined with SERS active nanotags to provide an alternative solution to overcome this obstacle.

Chapter 2. Synthesis of Hollow Gold Nanospheres and Their SERS properties

2.1. Introduction

The penetration depth of photons in biological tissues is limited by the inherent absorption and scattering of the components which make up tissues such as blood and water. These components have reduced absorption and scattering effects in the near infrared (NIR) region which provides a relatively transparent optical sensing window for bioimaging.[51] Due to their low toxicity and rich surface modification methods, gold nanoparticle have been widely used in biological sensing via surface enhanced optical techniques.[1,3] However, the localised surface plasmon resonances (LSPRs) of typical gold nanospheres are in the visible range, which limits their applications in turbid media like blood. Therefore, significant effort is being put into developing novel nanostructures based on gold which are active in the NIR window. For example, gold nanorods[50], nanostars[87] and nanocages[55] have been synthesized with a desirable localised surface plasmon resonance range. Unfortunately, these nanostructures are normally covered by surfactants due to synthesis methods, which are usually toxic and hard to replace. Halas and coworkers established and improved the synthesis of gold nanoshells that consist of a dielectric silica core nanoparticle surrounded by an ultrathin metal shell with tunable localised surface plasmon resonance up to one micrometer.[88,89] Because of their optical properties and easily functionalised surface, these nanoshells have been used for immunoassays,[90] photothermally modulated drug delivery,[91] photothermal ablation[92-94] as well as *in vitro*[95,96] and *in vivo*[97] molecular imaging. However, the size of the silica/gold nanoshells with LSPRs close to one micrometer is typically larger than 200 nm[89] which could be problematic for cell membranes penetration.[98]

Hollow gold nanospheres (HGNs) consisting of a spherical gold shell filled with embedding medium (usually water) were introduced in section 1.5.1. The biggest advantage of this type of material is its red-shifted localised surface plasmon resonance yet relatively small size (less than 100 nm) which facilitates its use in biological applications.[61] Recently, an improved synthesis of hollow gold nanospheres in the NIR region using poly(vinylpyrrolidone) (PVP) was reported by Zhang *et al*.[99] Although the reproducibility of the synthesis was improved, the PVP covered nanoparticle surface may become an obstacle for further surface functionalization. In addition, the reported localised surface plasmon resonances of the HGNs were still below 900 nm which is not ideal for human tissue imaging.[100]

In the first part of this chapter, the localised surface plasmon resonances of HGNs are extended up to 1320 nm and importantly the resulting HGNs possess a citrate-covered surface, which can be easily replaced to allow functionalisation of the HGNs.

SERS from metallic nanospheres[19,101] and nanoshells[102,103] have been extensively investigated. However, as a recently developed material, the SERS performance of hollow gold nanospheres has not been thoroughly investigated.[104] To gain a better understanding of the SERS response of HGNs, HGN samples with different localised surface plasmon resonances were functionalised with different Raman reporters which were either on or off resonance with the laser excitation wavelengths. This study gives an insight into the basis of the SERS properties for these kinds of materials.

2.2. Experimental

2.2.1. Synthesis of hollow gold nanospheres

The synthesis of HGNs was adapted from previous reports[99,105] and carried out in a standard Schlenk line (Figure 12) under Ar. In a typical synthesis, 100 µL of 0.4 M cobalt chloride hexahydrate (Fisher Scientific, 99.99%) and 400 (HGN-1320) to 650 (HGN-650) µL of 0.1 M trisodium citrate dihydrate (Sigma-Aldrich, >99%) were added to 100 mL of deionized water and degassed twice. One mL of 0.1 M sodium borohydride (Fisher Scientific, 99%) was injected into the solution under rigorous stirring. The magnetic stirrer was replaced with bubbling argon through a glass pipette in the solution for the synthesis of HGNs with a LSPR above 800 nm. This solution was allowed to react for 20 min under constant argon flow until hydrogen gas evolution ceased, indicating complete hydrolysis of the reductant. 500 µL of 0.2 M trisodium citrate dihydrate was then injected and reacted for a further 10 min. Next, 33 mL of chloroauric acid trihydrate (Fisher Scientific, ACS reagent grade) of different concentrations ranging from 10 µM (HGN 1320) to 130 µM (HGN 650) was injected under rigorous stirring/constant bubbling. This mixture was reacted for a further 10 min under argon before being exposed to air. Finally, 500 µL of 0.1 M sodium citrate was added under vigorous stirring/constant bubbling to stabilize the HGNs, and a colour change (from brown to light green or colorless) was observed. After synthesis, the solution was filtered through a 0.45 µm Millipore filter and concentrated through centrifugation (3466 × g). The precipitate was redispersed into 2 (HGN 1320) to 15 mL (HGN 650) of 0.6 mM sodium citrate solution.

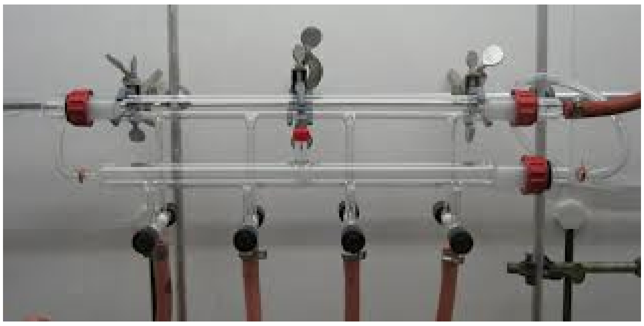

Figure 12 Schlenk line consists of a dual manifold with several ports. One manifold is connected to a source of purified inert gas, while the other is connected to a high-vacuum pump. The inert gas line is vented through an oil bubbler, while solvent vapors and gaseous reaction products are prevented from contaminating the vacuum pump through a liquid nitrogen or dry ice/acetone cold trap.[106]

2.2.2. Characterization

The HGN samples were investigated with high resolution scanning/transmission electron microscopy S/TEM, FEI Titan 80-300 operated at 300 kV.

Before SERS measurements, the concentrations of the hollow gold solutions were adjusted to the same level with the aid of a Nanosight® LM10 based on the Rayleigh scattering technique via the procedure described in the instrument technical notes. The original concentrated solutions were diluted with filtered milli-Q water until 20 to 60 nanoparticles per frame were obtained. The imaging videos were recorded for 60 s and analyzed using the provided software (NTA 2.1). The required dilution factor was then applied to the rest of the samples.

Investigations into the SERS properties of hollow gold nanospheres were carried out by mixing 135 μL of the concentrated hollow gold solution (for HGN1, it was firstly diluted by half before used) and 15 μL of different Raman reporters: 2×10^{-7} M Trans-1,2-bis(4-pyridyl)-ethylene (BPE, Sigma-Aldrich, 97%) in water, 2×10^{-7} M NIR-797 isothiocyanate (Sigma-Aldrich, ≥70%) in water, and 2×10^{-7} M Malachite green isothiocyanate (Invitrogen Life Science, UK) in water. This was followed by 150 μL of water or 30 mM KCl, the samples were left to stabilize overnight before SERS measurements.

Two excitation wavelengths, 632.8 and 785 nm, were used during the SERS study. 632.8 nm solution SERS spectra were recorded using a Renishaw Ramascope system 2000 with a 632.8 nm line of a helium-neon laser as the excitation source. An Olympus 20×/NA0.4 long-working distance objective was used for excitation and signal collection in a 180° backscattering geometry from a microcuvette. The unfocused power output was measured to be ~4.8 mW at the sample. Dielectric edge filters were used to reject the Rayleigh scattered light. Spectra were accumulated for 10 s, and five replicates were carried out at each sample point; the signals were normalized to a cyclohexane standard.

785 nm solution SERS spectra were recorded using a 785 nm diode laser fibre optically coupled probe system attached to a Renishaw inVia microscope system, using an f18 focusing/collection lens. The power at the sample was measured to be ~90 mW, and a 1200 groove diffraction grating was used. Spectra were accumulated for 10 s, and five replicates were carried out at each sample point; the signals were normalized to a cyclohexane standard.

Samples for SEM analysis were prepared on polyelectrolyte functionalized silicon wafers as reported previously.[107,108] Wafers were cleaned using water and ethanol then dried in a N_2 flow. They were then placed in an oxygen plasma cleaner for 60 s before being coated with poly(diallyldimethylammonium chloride) (Sigma-Aldrich) (PDDA). 30 μL of PDDA was dissolved in 1 mL of 1 mM NaCl and then dropped onto the clean wafer for 30 min under a water-saturated atmosphere before being washed off and dried in a N_2 flow. 100 μL of each HGN sample was put onto the PDDA-functionalized silicon wafer for 15 min under a water-saturated atmosphere. The sample was then washed off and dried in a N_2 flow.

SEM was carried out on a Sirion 200 Schottky field-emission electron microscope operating at an accelerating voltage of 5 kV. The samples did not require additional metallic coating before imaging and the particle size was analyzed using image-J. The extinction spectra were acquired using a Cary 5000 UV-vis-NIR spectrometer.

2.3. Results and Discussion

2.3.1. Synthesis of hollow gold nanospheres

Previously, the Co nanoparticle suspension was transferred from a controlled atmosphere to an open air solution containing different concentrations of Au^{3+} ions.[105] This method requires very high experimental skills. Firstly, a large syringe was partially filled with argon and then the Co NPs solution was quickly removed from the round bottom flask. The Co solution was injected into diluted chloroauric acid trihydrate solution with vigorously stirring as soon as possible. Although every step was performed very carefully, the Co NPs can still be partially oxidized.

Figure 13 shows the extinction spectrum of one HGN sample (HGN-1) using this method with the maximum absorption wavelength at 619 nm.

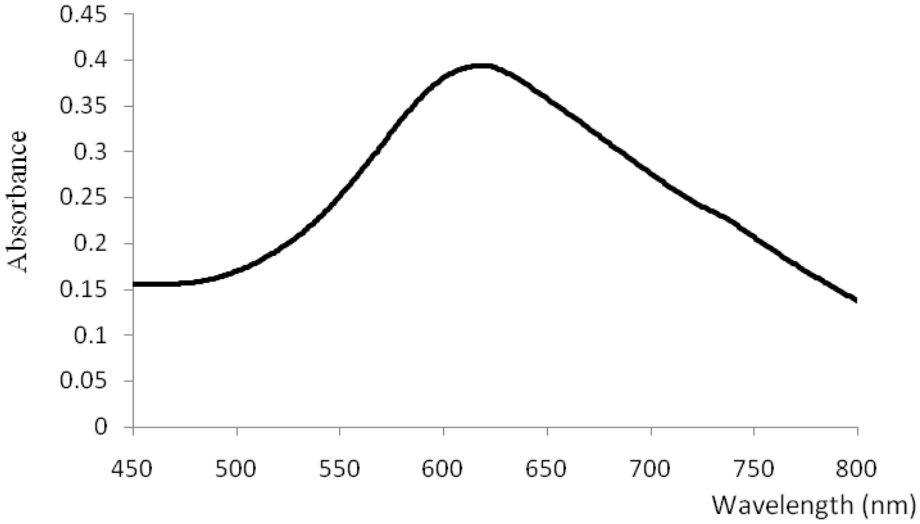

Figure 13 Extinction spectrum of HGN-1 produced according to ref. 60

Through a careful examination of SEM images (Figure 14) of samples synthesized by this method, only nanoparticles with rough surfaces were obtained. There are two probable reasons for this. First, during the transferring process, some Co NPs were inevitably oxidized by air even if the process was done rapidly. Once Co NPs are partially oxidized, only non uniform HGNs can be obtained. More likely, at the initial injection point, the amount of Au ions is much more than the amount of Co NPs, therefore all Co NPs in the solution will be oxidized after injection. Furthermore, due to the electron transportation, the reduced reaction will happen not only at the surface of Co nanoparticle, but also in close proximity to the surface. Figure 15 reveals the schematic of this possible mechanism.

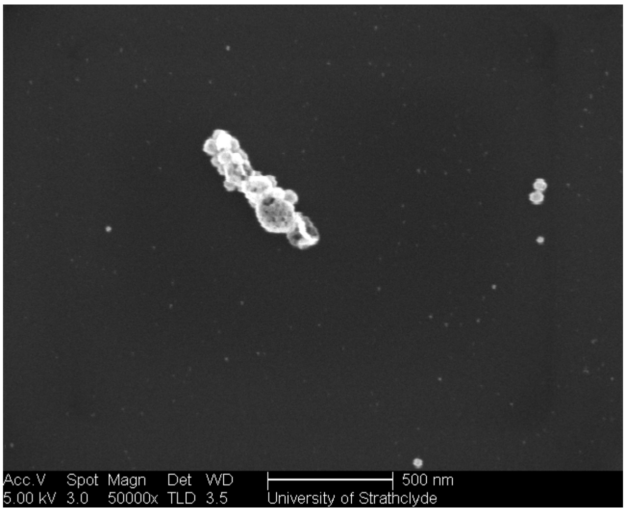

Figure 14 Representative SEM image of HGN-1 produced according to ref. 60.

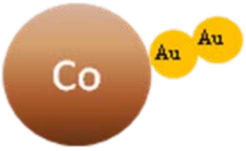

Figure 15 Schematic of a possible mechanism of non uniform hollow gold formation.

To overcome this issue, the same group recently reported an improved method which introduced PVP as a capping agent to protect the Co nanoparticles from oxygen when being transferred provides better reproducibility.[99] However, as mentioned previously, the presence of PVP on the nanoparticle surface will hinder its further functionalisation.

In this work, a slightly modified method using the injection of Au ion solution instead of Co NP solution was initially developed resulted a much better quality of HGNs. Figure 16 demonstrates the extinction spectrum of a typical sample named HGN-2 using this method. The maximum absorption wavelength is at 700 nm.

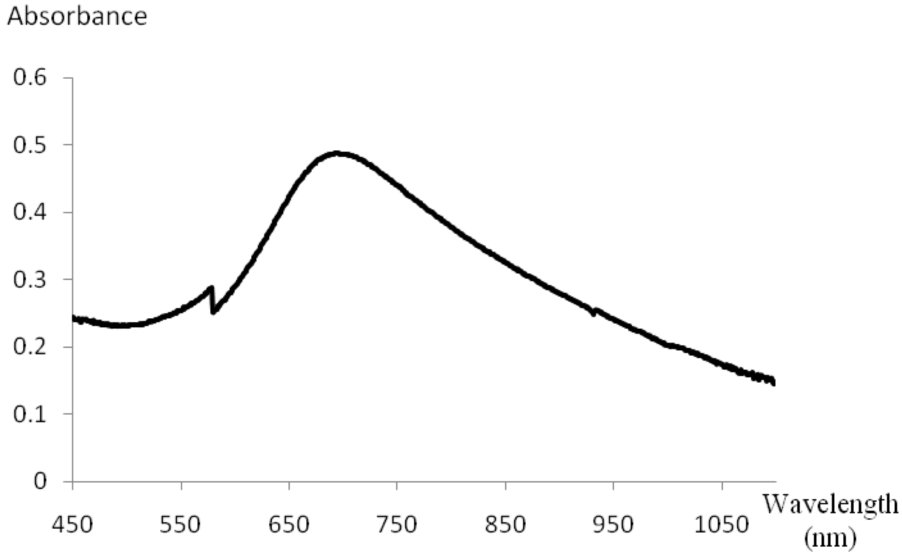

Figure 16 Extinction spectrum of HGN-2 using the improved synthesis method.

From the SEM image of HGN-2 (Figure 17), the surface of HGNs is smooth, however, some obvious pin-holes are found. This can be explained by the mechanism of formation of the HGNs. At the beginning, gold ions are reduced by cobalt nanoparticles and a Co@Au core-shell structure is formed. After exposing to air, Co NPs are oxidized into Co^{2+} in the presence of oxygen, and pin-holes should be formed at this stage. Finally, samples synthesized by this method are demonstrated in Figure 18.

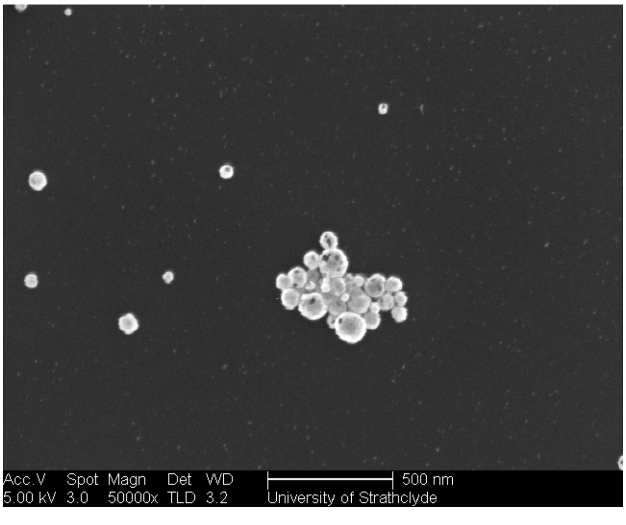

Figure 17 SEM image of HGN-2 using the improved synthesis method.

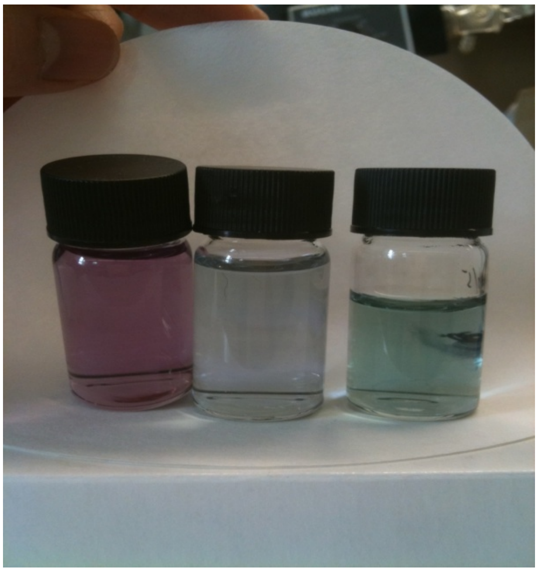

Figure 18 Hollow gold nanoparticles with different LSPRs. The λ_{max} of red (left), blue (middle), and green (right) are 550 nm, 618 nm, and 700 nm respectively.

However, after one or two days, some black sediments were observed from the produced HGN samples and the suspensions became colourless indicating the synthesized samples were not very stable. Therefore, a further improvement was made. Inspired by Zhang *et al.*,[99] the Co nanoparticle suspension was further stabilized by the injection of 500 μL of 0.2 M sodium citrate solution instead of PVP and the Au^{3+} solution was degassed with argon before being injected into the Co nanoparticle suspension. The different order of addition avoids the oxidation of the Co nanoparticles allowing high quality and reproducible hollow gold nanospheres to be generated. In addition, due to Co nanoparticles being magnetic, the use of a magnetic stirrer would result in the formation of chain structures instead of individual nanospheres, especially when less sodium citrate is used.[109] (Figure 19) Therefore, the magnetic stirrer was removed when HGNs with localised surface plasmon resonances larger than 800 nm were desired. The issue of achieving suitable mixing to form a homogeneous solution was solved by continuously bubbling argon through the solution while simultaneously providing manual agitation of the flask. These modifications in the synthetic protocol created extremely red-shifted HGNs.(Figure 20)

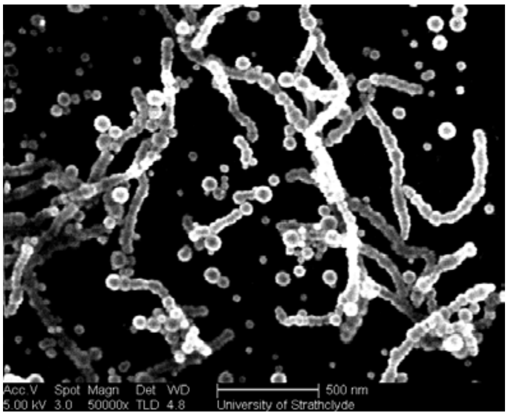

Figure 19 SEM image of HGN with less amount of citrate presented under the external magnetic field generated by a magnetic stirrer.

The reproducibility of the synthesis is determined by several factors. First, the glassware should be clean without any organic residues. This can be done by rinsing the glassware with aqua regia following by piranha solution. (Caution: the aqua regia should be completely removed and rinsed with water several times before the addition of the piranha solution.) Secondly, the quality of the hollow gold nanospheres is decided by the quality of the cobalt nanoparticles. Sometimes, after the addition of 1 mL of 0.1 M $NaBH_4$, a grey coloration was obtained which meant highly poly-dispersed Co nanoparticles. This can be solved by further removing the dissolved oxygen in the main solution and increasing the mixing speed. $NaBH_4$ was dissolved in oxygen free water which also enhances the synthesis quality. Bubbling Argon into the solution is a good way of mixing when a magnetic stirrer needs to be avoided to solve both mixing and dissolved oxygen problems. Finally, although reducing the amount of sodium citrate can increase the size of the Co nanoparticles which would produce more red-shifted hollow gold nanospheres, the Co nanoparticles would aggregate if insufficient citrate were present. Therefore, a balance should be found here. Occasionally, when the flask was replaced, different results were obtained. This is probably due to the presence of scratches inside the original or replacement flask which might change the reaction dynamics and therefore the result. However, the exact mechanism is still unknown. To obtain constant results, the same flask is recommended but the different results between flasks can be compensated by tuning the amount of sodium citrate and the concentration of the gold ions. In addition, both Milli-Q water and double distilled water were used for the synthesis and no differences were found.

Figure 20a shows the tunable localised surface plasmon resonances of the prepared HGNs which ranged from 610 nm up to 1320 nm. When the LSPRs are below 750 nm, the shells were found to be nearly complete as they did possess some non-obvious pin-holes on the surface (Figure 20b) which is consistent with previous reports.[99,105] Interestingly, when the LSPRs of the HGNs were red-shifted, not only did the overall size of the nanosphere increase slightly; from 53 ± 8 nm for a LSPR of 650 nm to 87 ±16 nm for a LSPR of 1320 nm, (Table 2) but the pin-holes grew to be quite substantial holes. Figure 20c shows a TEM image of HGNs with a LSPR of 1320 nm. Surprisingly, the overall size of these HGNs is relatively small with a diameter of just 87 ± 16 nm; unfortunately, the shell thickness is hard to measure precisely due to the porous structure. An image showing the details of this type of HGNs is shown in Figure 20d, the hole sizes range from several nanometers up to 25 nm. Importantly, the hole size can be controlled by the addition of different concentrations of Au^{3+} solution which also tunes the localised surface plasmon resonance. The presence of surface cavities provide a more red-shifted localized surface plasmon resonance[110] and that is the reason that these HGNs can generate the extremely red-shifted localised surface plasmon resonance yet keep their overall size small compared to other nanospheres in the literature.[88] In addition, as seen in Figure 20a, when the LSPRs of the HGNs are red-shifted, their extinction spectra become broader and a small shoulder at ~700 nm is observed in the case of HGNs with a LSPR of 1320 nm. The observed shoulder is probably due to the polydispersity of the Co nanoparticle sizes during the synthesis resulting in a sub-population of smaller sizes of hollow gold nanospheres. The broader spectrum effect is an inherent property of LSPR at longer wavelength but could also be due to the surface cavities present which create less well-defined structures, especially in the NIR region.

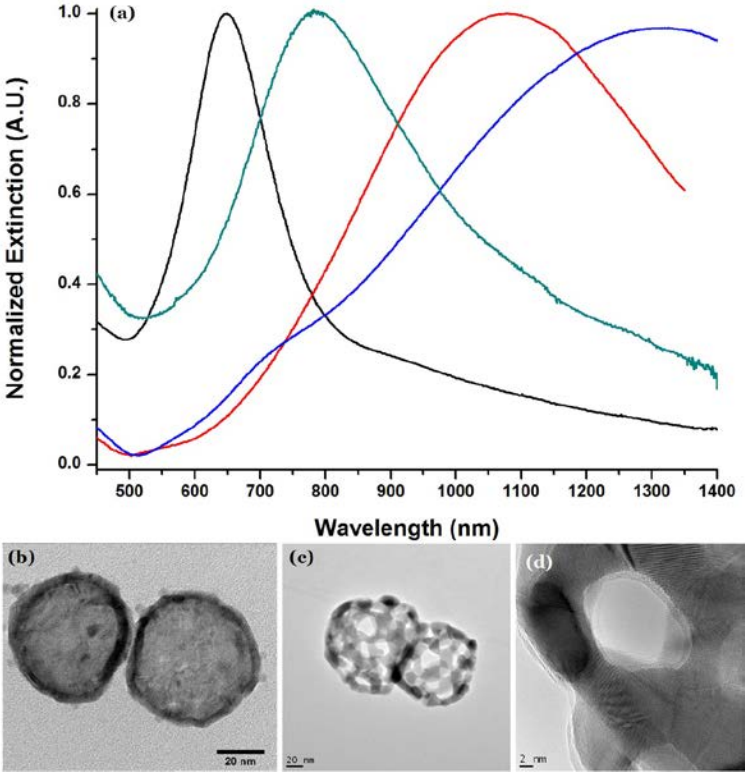

Figure 20. Normalized extinction spectra of synthesized hollow gold nanospheres associated with representative TEM images. a) Normalized extinction spectra of differently prepared hollow gold nanospheres; b) Representative TEM image of hollow gold nanospheres with a SPR of 750 nm; c) representative TEM images of hollow gold nanosphere with a SPR of 1320 nm; d) close up TEM image of a part of c.

2.3.2. SERS Investigation of Hollow Gold Nanospheres

2.3.2.1. Characterization of hollow gold nanospheres

Two different sizes of hollow gold nanospheres, HGN1 and HGN2, with LSPRs overlapping standard laser excitation wavelengths were synthesized according to the above section. Their normalized extinction spectra are shown in Figure 21. HGN1 is resonant with 632.8 nm laser excitation and has an average size of 54±6 nm with a shell thickness of 8.3±0.6 nm while HGN2 is resonant with 785 nm laser excitation and has an average size of 65±9 nm with a shell thickness of 6.5±1.3 nm.[60,111] In addition to the localised surface plasmon resonance of the nanoparticles, SERS is dependent on the number of nanoparticles present within the laser volume and the enhancement factor of each particle or cluster.[19] Therefore, to compare the SERS properties of different kinds of nanoparticle solutions, it is important to normalise the particle concentration. HGN1 was firstly diluted by half then further diluted by 1000x while HGN2 was diluted by 1000x directly before imaging was carried out using a Nanosight®LM10. The final concentrations of diluted solutions were found to be 3.33×10^8 particles/mL for HGN1 and 3.46×10^8 particles/mL for HGN2 under the same imaging conditions. Thus HGN2 had a very slightly higher particle concentration than HGN1 (diluted by half) but the difference in practical terms was deemed to be negligible.

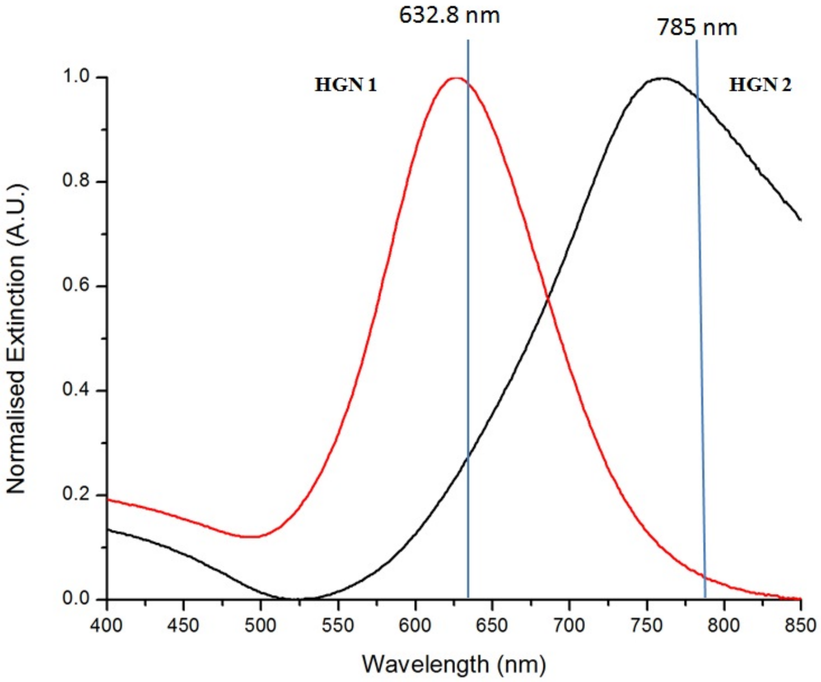

Figure 21. Normalised extinction spectra of two types of hollow gold nanospheres. The laser excitations used in the SERS experiments are marked.

2.3.2.2. Aggregation profiles of hollow gold nanospheres

It has been stated that the majority of the SERS signal in an aggregated sample originates from a very small number of molecules on the surface of the nanoparticles.[112] Aggregation of nanoparticles results in the coupling of plasmons between particles leading to the formation of "hot spots" where the electromagnetic field is significantly enhanced.[77] Aggregation is achieved by the addition of an electrolyte, normally a simple inorganic salt, which screens the Columbic repulsion energy between the nanoparticles. The van der Waals attraction then dominates and coagulation of the colloid occurs.[113] Partial aggregation can create effective "hot spots" consisting of dimers and trimers.[114] Importantly, the formed suspension does not contain large clusters, which would sediment, and therefore it remains stable for a period of time, which is preferred for further analysis. A very low concentration of analyte, 10 nM final concentration, which is insufficient to significantly affect the columbic repulsion was used to avoid any aggregation caused by the addition of reporter molecules ensuring all aggregation was only induced by the salt.[115,116] The partial aggregation extinction spectra of HGN1 and HGN2 are shown in Figure 22 and Figure 23. For HGN2, a big blue shift was observed after the addition of analyte but there was a negligible change for HGN1. The aggregation profiles of hollow gold nanospheres are quite different from that of normal gold and silver nanoparticles. A blue shift instead of red shift was observed upon aggregation,[117] HGN2 showed a much larger shift compared to HGN1. The coupled LSPR of hollow gold highly depends on the thickness of the shell,[111] thus, from the extinction spectra it can also be concluded that HGN2 has a thinner wall compared to HGN1. Upon aggregation of thin-shell HGNs, a pronounced, newly formed longitudinal LSPR that was blue-shifted with respect to the transverse LSPR of isolated HGNs was observed.[118] Importantly, the concentration of analytes was extremely low, this trend was found to be analyte independent; therefore only nanospheres functionalised with malachite green are shown as an example.

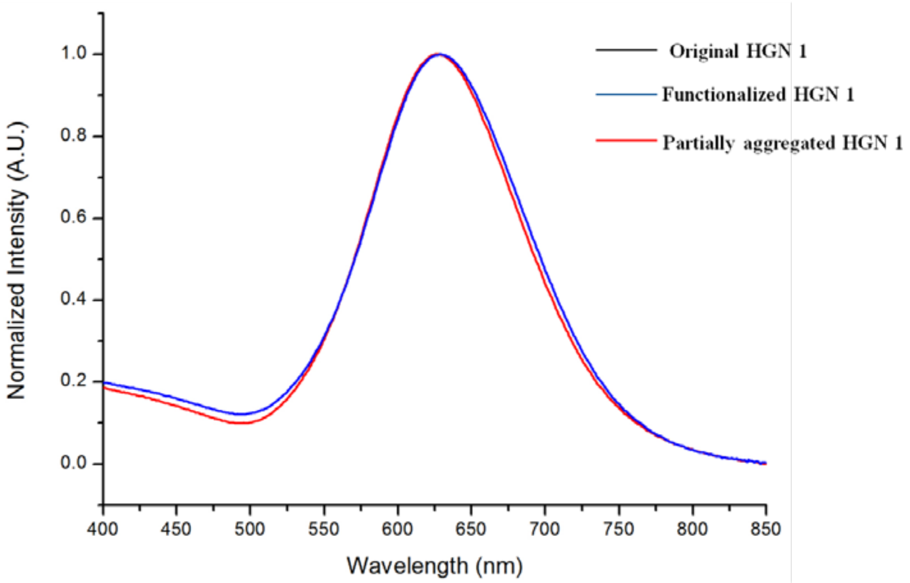

Figure 22. Normalized extinction spectra of isolated HGN1, functionalized HGN1 and partially aggregated HGN1.

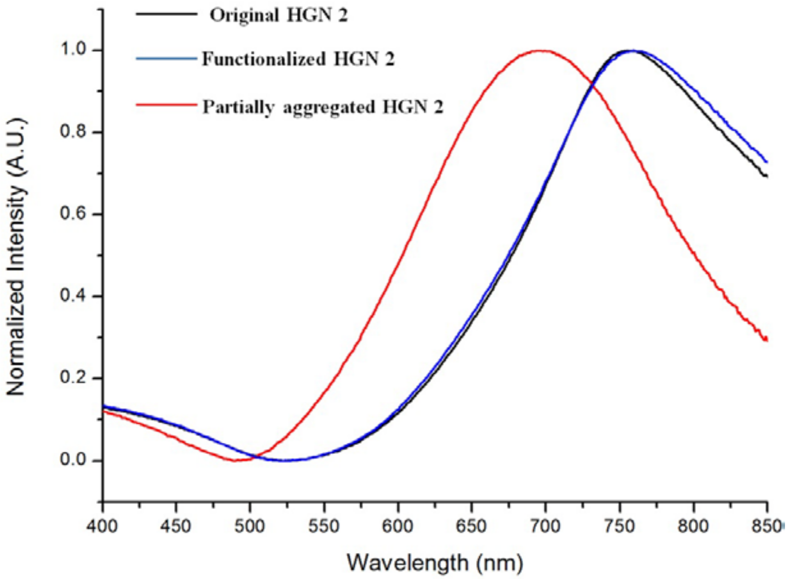

Figure 23. Normalized extinction spectra of isolated HGN2, functionalized HGN2 and partially aggregated HGN2.

The aggregation states of HGNs pre-functionalized with Raman reporters were investigated by SEM. HGNs were deposited on PDDA functionalized silicon wafers, which were positively charged and could therefore capture the negatively charged nanoparticles. Deposition was carried out under a water-saturated atmosphere over 15 min to avoid the formation of large surface aggregates due to the drying of nanoparticle suspensions. Figure 24 shows typical SEM images of partially aggregated HGN1 and HGN2 samples. For clarity, dimers and trimers are marked with different shapes. Through careful examination of the original SEM images it could be seen that the surface of HGN1 particles were complete while there were several obvious cavities on the surface of the HGN2 particles.(Figure 25) The number and size of the aggregates formed were counted and the percentages of particles involved in each sample are reported in Table 1. The approach we have undertaken was found to ensure that the observed aggregates deposited onto the surface were representative of those in solution due to a controlled deposition time and by focusing on the use of comparative studies rather than absolute assignment of aggregate morphology percentages.

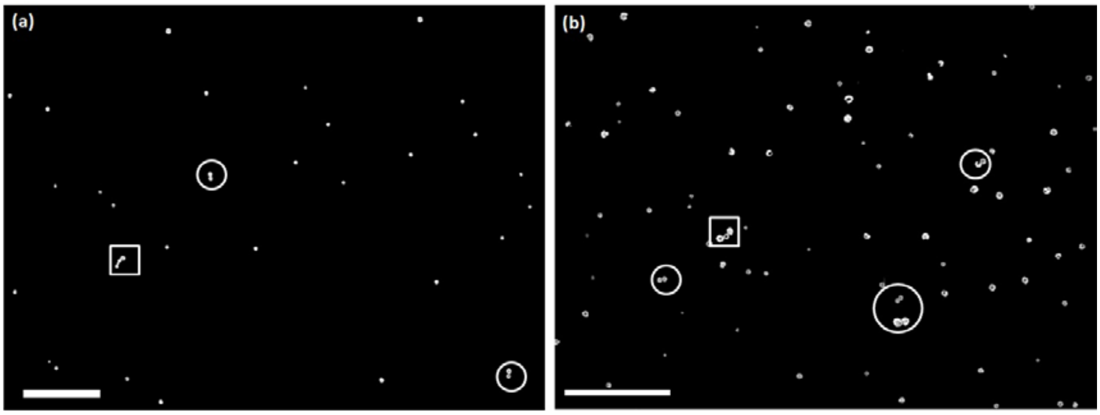

Figure 24. SEM images of partial aggregates of HGN1 (a) and HGN2 (b). The scale bar in each image is 1 μm; for clarity dimers are circled, and trimers are boxed.

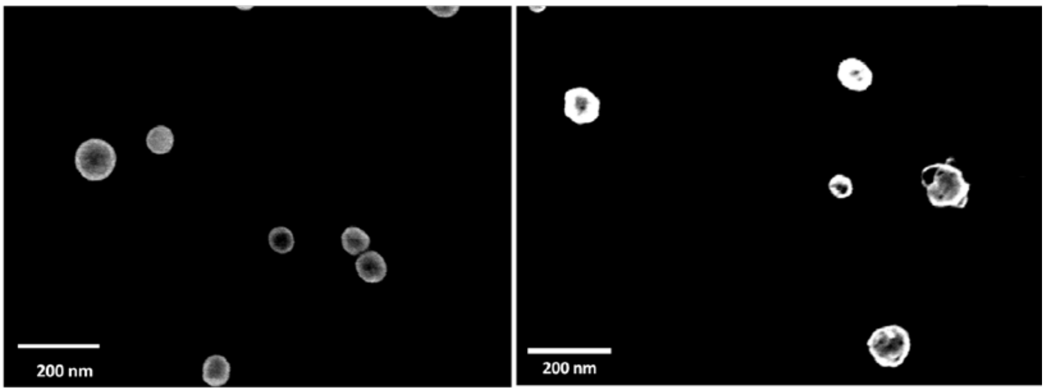

Figure 25. High magnification SEM of isolated HGN1 (left) and HGN2 (right).

Table 1. SEM cluster analysis, values are percentages of nanoparticles involved in each cluster type

	monomers (%)	dimers (%)	trimers(%)	tetramers(%)	small aggregates (5-10) (%)	total colloid particles (%)
Isolated HGN1	96.3	2.3	1.4			218
Partially aggregated HGN1	75.0	14.1	5.4	2.4	3.1	540
Isolated HGN2	95.5	2.0	1.0	1.0	0.5	201
Partially aggregated HGN2	78.1	15.8	4.5	1.0	0.6	494

Note that the result of counting the aggregates immobilized on a surface from an HGN2 suspension and characterized by SEM is not consistent with its extinction spectrum (Figure 23). The large blue shift of the spectrum should be normally caused by the presence of a large portion of aggregates; however, Table 1 shows the majority of the colloidal suspension is made of monomers and the reasons for this needs further investigation.

The isolated HGNs, without salt addition, were found to contain small numbers of dimers and trimers, but the vast majority of particles existed as monomers. The addition of a salt concentration of 30 mM KCl reduced the percentage of monomers and increased the percentages of dimers, trimers and tetramers. As the number of aggregates formed is sensitive to the concentration of nanoparticles and equilibration time, differences between HGN1 and HGN2 should be small since their concentrations were very similar before salt addition. In addition, as a low concentration of Raman reporters (10 nM final concentration) was used, the aggregate status was found to be analyte independent.

2.3.2.3. SERS performance of hollow gold nanospheres

Malachite green is resonant with 632.8 nm excitation therefore an extra enhancement is expected from the dye. The LSPRs of isolated and partially aggregated HGN1 show that this substrate is also resonant with the excitation wavelength (Figure 22). Although the isolated HGN2 has a LSPR of 760 nm, a large blue shift (around 100 nm) caused by the addition of 30 mM KCl brought it close to the resonance region of 632.8 nm excitation (Figure 23). Figure 26 shows the offset SERS spectra of malachite green from the different substrates using 632.8 nm excitation. Unlike isolated HGN1 (Figure 26b), non-aggregated HGN2 (Figure 26d) gave negligible SERS presumably due to the small overlap between the LSPR and the excitation wavelength. Both partially aggregated HGN1 and HGN2 samples show increased signal compared to when they were non-aggregated. As previously described, nanoparticle aggregates form “hot spots” where the electromagnetic field is significantly increased. Importantly, when HGN2 was partially aggregated, its LSPR was close to the 632.8 nm laser excitation. (Figure 23) However, even when partially aggregated, the SERS signal intensity of HGN2 was of a similar level to isolated HGN1 under the same experimental conditions.

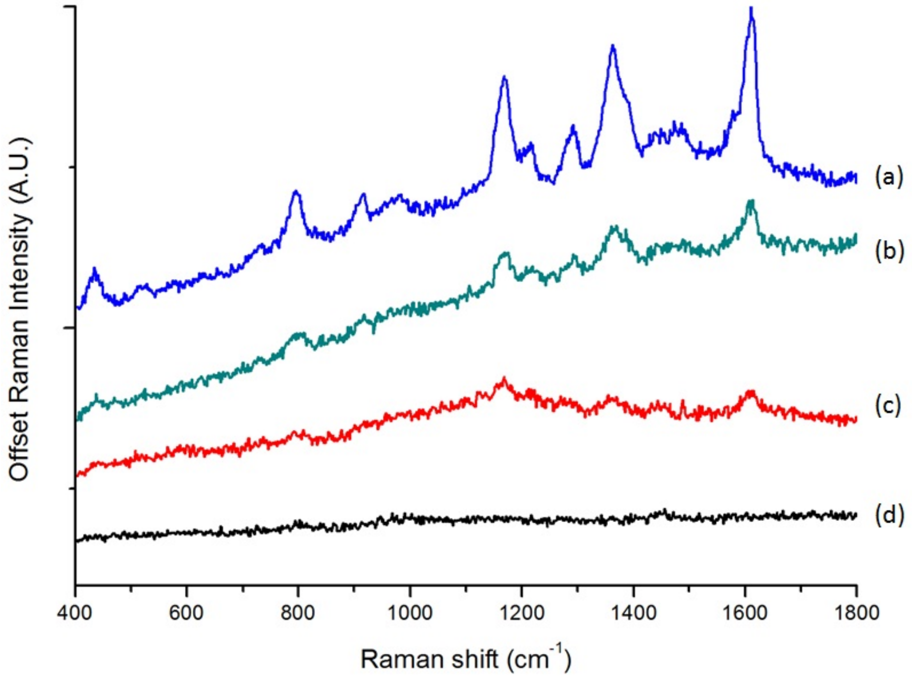

Figure 26. SERS spectra of malachite green using 632.8 nm excitation wavelength, spectra have been offset for clarity. a) partially aggregated HGN1; b) isolated HGN1; c) partially aggregated HGN2; d) isolated HGN2.

When the non-resonant reporter molecule trans-1,2-bis(4-pyridyl)-ethylene (BPE) was added to HGN and 632.8 nm excitation was used, the signal was significantly weaker but still distinguishable above the background (Figure 27). Partially aggregated HGN2 generated the same signal intensity as the isolated HGN1 sample. The similar trends observed regardless of whether resonant or non-resonant molecules were analyzed suggest that the effect is molecule independent.

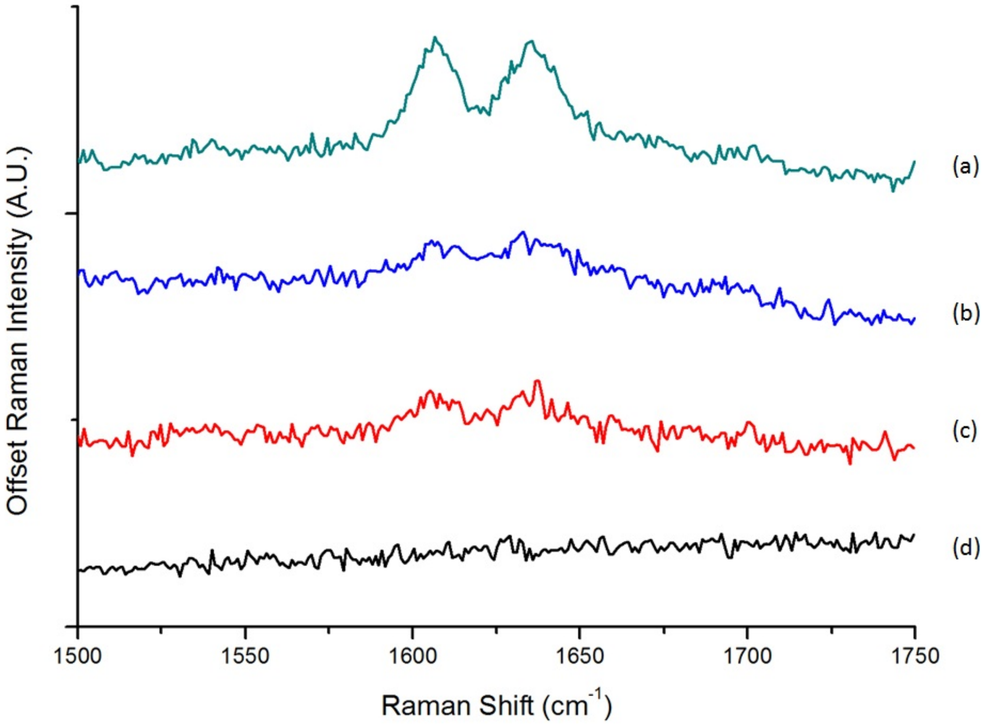

Figure 27. SERS spectra of BPE at 632.8 nm excitation. a) partially aggregated HGN1; b) isolated HGN1; c) partially aggregated HGN2; d) isolated HGN2.

When the laser excitation was changed to 785 nm, isolated and partially aggregated HGN1 were no longer resonant (Figure 22) however the isolated HGN2 were in resonance (Figure 23). Surprisingly, isolated HGN2 functionalized with BPE still gave negligible signals (Figure 28d). As shown in Figure 28, the partially aggregated HGN1 (Figure 28a) still gave the highest SERS intensity despite having a SPR maximum away from the laser excitation wavelength.

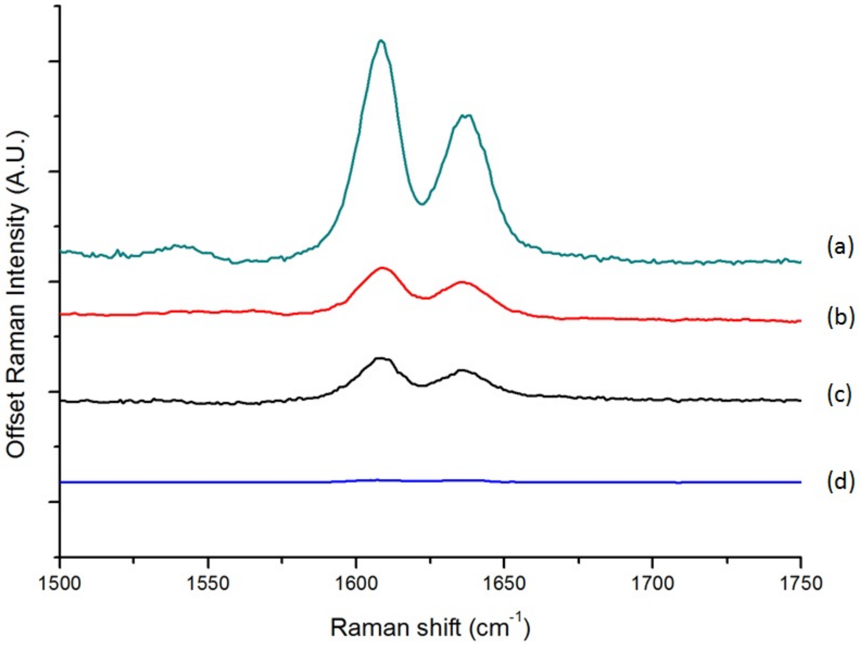

Figure 28. SERS spectra of BPE at 785 nm excitation. a) partially aggregated HGN1; b) isolated HGN1; c) partially aggregated HGN2; d) isolated HGN2.

To rule out the influence of the reporter molecule, NIR-797 dye which is resonant with 785 nm excitation was used and a similar trend was observed. (Figure 29) In addition, different batches of HGN1 and HGN2 were used to repeat the experiments under the same conditions. Although slight SERS intensity variations were observed, the same trends were obtained.

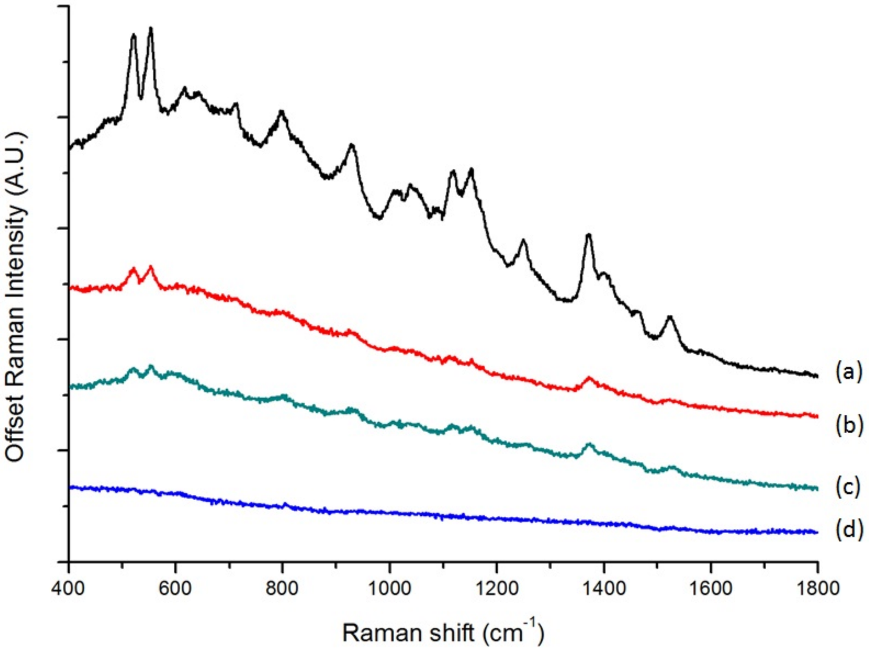

Figure 29. SERS spectra of NIR-797 at 785 nm excitation. a) partially aggregated HGN1; b) isolated HGN1; c) partially aggregated HGN2; d) isolated HGN2.

2.3.2.4. Discussion of SERS properties of hollow gold nanospheres

From the SERS results, HGN1 was observed to generate a higher SERS performance than HGN2 irrespective of whether it was isolated or partially aggregated or its LSPR was resonant with the laser excitation or not. Recently, Chandra *et. al.* simulated the electric field spatial profiles of HGNs with fixed outer diameters but different wall thicknesses.[118] For isolated HGNs, when the shell became thinner, the outer electric field decreased when compared to thicker shell particles.[118] The same theoretical results were also obtained for hollow nanoframes.[119] In the work reported here, the reporter molecules were attached to the outer surface thus it is reasonable to expect that HGN1, with its thicker shell, generates higher SERS signals than HGN2. When isolated HGNs became partial aggregates, the particles were in contact as seen by the blue shifts in the extinction spectra.[117,118] In electric field calculations of touching nanoshells, a significantly increased electric field was observed along the cavity walls when HGNs with thinner shells were in contact with each other. In contrast, HGNs with thicker shells exhibited the majority of the electric field intensity at the conical region at the particle interface.[118] Therefore, an increase in signal was observed for every SERS measurement carried out in partially aggregated samples compared to the isolated HGN samples. The signal differences obtained between partially aggregated HGN1 and HGN2 is assumed to be because of the intrinsically weak electric field distribution of HGN2. In addition, surface pin-holes formed during the synthesis are considered to generate an extra enhancement in the surface electric field.[64,111] In fact, from SEM images, obvious cavities were observed on the surface of HGN2 (Figure 25). Although surface cavities can provide a red-shifted surface plasmon resonance,[110] these holes are too big to play a role in enhancing the surface electric field. In addition, HGN2 is larger than HGN1 and has a larger surface area therefore, with the same analyte concentration, HGN2 should load at least an equal amount of analyte on the surface yet it generates lower signals. Hence, although HGN2 with its thinner shell generates a red-shifted SPR, it is not a good choice for a SERS substrate based on the experimental results which are also backed up with the previously published electric field distribution stimulations.

2.4. Conclusions

In this chapter, an improved synthesis of hollow gold nanospheres, which extends their localised surface plasmon resonances up to 1320 nm, has been demonstrated. HGNs with different localised surface plasmon resonances were functionalized with different Raman reporters. HGNs and Raman reporters on and off resonance with standard laser excitations were systematically interrogated in isolated and partially aggregated situations respectively. HGN1 which had a thicker shell always gave higher SERS performance than HGN2 independent of whether it was isolated or in a partially aggregated state or if its SPR was resonant with the laser excitation or not. For isolated HGNs, when the shell thickness becomes thinner, the outer electric field decreased. When isolated HGNs became partially aggregated, a significant electric field was observed at the particle interface. The signal differences between HGN1 and HGN2 in the partially aggregated situation is due to the intrinsically weak electric field distribution of HGN2. This suggests that it may be worth trying functionalization of the inner wall of thin shelled HGN based on the spatial electric field distribution maps.

In the following chapter, the further SERS study of HGNs at longer excitation will be discussed. In addition, after comparing the SERS activities between different types of HGNs, it is important to know how these nanomaterials actually perform comparing to the standard solution based SERS substrates such as solid gold and silver nanoparticles. Therefore, in the next chapter, the comparison of optical properties among different types of nanoparticles will also be presented.

Chapter 3. Comparison of Optical Properties in the NIR Region between Hollow Gold Nanospheres and Standard SERS Active Nanospheres

3.1. Introduction

1064 nm excitation provides a better penetration ability in turbid media such as human tissues (Figure 30), [100] however, the scattering intensity depends on the 4th power of the excitation frequency,[120] therefore Raman scattering at this wavelength tends to be weak. To take advantages of 1064 nm excitation wavelength for sensing, an appropriate SERS substrate to enhance the weaker scattering at this wavelength is needed. Several efforts have been put into developing new SERS substrates suitable for this excitation wavelength including gold nanoshells,[121] carbon nanotubes,[122] silver colloid,[123] and gold nanorods.[124]

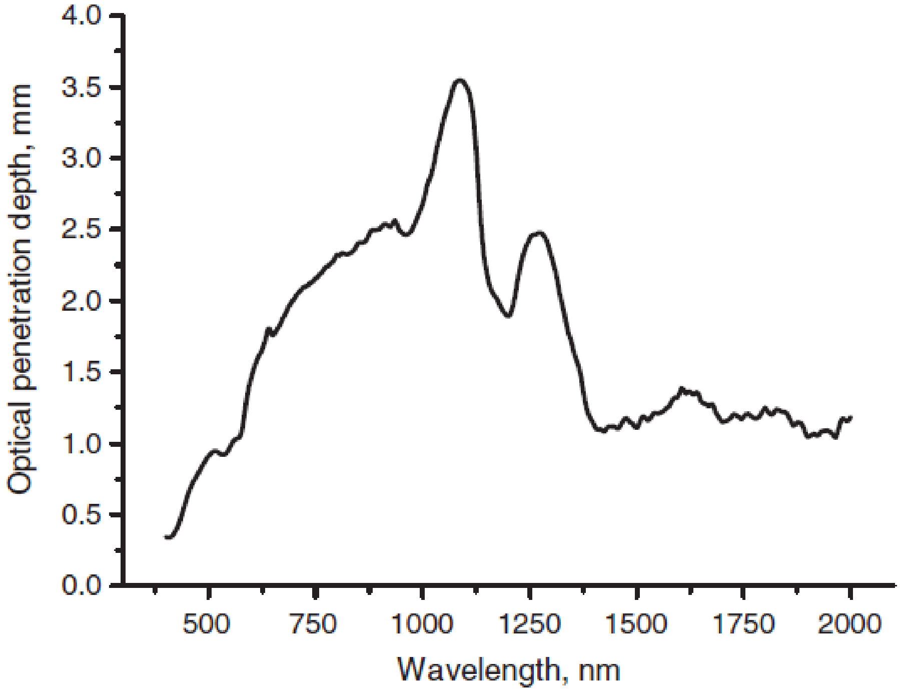

Figure 30 The optical penetration depth δ of light into skin over the wavelength range from 400 to 2000 nm.[100]

Hollow gold nanospheres (HGNs) demonstrate tunable localised surface plasmon resonances from the visible to NIR range which is favorable for biological sensing.[51] In section 2.3.2, we have already investigated the SERS properties of two different types of HGNs with LSPRs overlapping standard laser excitation wavelengths (632.8 and 785 nm). To further demonstrate the increased optical sensing abilities of HGNs in the NIR region, different types of HGNs with the same concentration are coupled with non-resonant Raman reporter molecules and measured at an excitation wavelength of 1064 nm. Furthermore, SERS comparison results with citrate reduced gold and silver nanoparticles of similar physical sizes and surface properties are measured using a 1064 nm excitation wavelength. Finally, the absorption properties of HGNs are probed using their photothermal responses under a continuous illumination with 785 nm excitation. This study provides insights into the interesting optical properties of hollow gold nanospheres in the near infrared region.

3.2. Experimental

3.2.1. Synthesis of different types of nanoparticles

The synthesis of HGNs has been shown in Section 2.2.1.

45 nm Au nanoparticles were synthesized using a two-step method.[9] Gold nanoparticles of 14 nm diameter with a narrow size distribution were prepared following the Turkevich-Frens preparation method introduced in section 1.1.1. 38.1 μmol (15 mg) of $HAuCl_4$ trihydrate were dissolved in 150 mL of milli-Q water and heated until boiling. Subsequently, 4.5 mL of the 1% w/w aqueous trisodium citrate solution, previously warmed to ca. 70 °C was added, and the mixture was refluxed for 30 minutes. The solution was then allowed to cool to room temperature under vigorous stirring.

37 μmol of $HAuCl_4$ trihydrate was added to 125 mL of Milli-Q water and heated until boiling. Subsequently, 5 mL of gold colloidal dispersion (14 nm sized nanoparticles acting as seeds) was added, followed by the addition of 1% w/w aqueous trisodium citrate (638 μL). The mixture was refluxed for 30 min under vigorous stirring. To ensure the stability of the colloidal dispersion, 4.9 mL of 1% w/w aqueous trisodium citrate was then added and further refluxed for 1 h. The colloidal dispersion was filtered through a 0.45 μm Millipore filter before centrifugation.

Silver colloid preparation was synthesized according to a previous report.[114] Briefly, 90 mg of silver nitrate was added to 500 mL of water at 45 °C, this was then rapidly heated to boiling, whereupon 10 mL of 1% sodium citrate was added and the temperature reduced to 98 °C for 90 minutes. After this time, the heating was removed and the solution allowed to cool to room temperature. The colloidal dispersion was filtered through a 0.45 μm Millipore filter before centrifugation.

3.2.2. Characterization

Before SERS and photothermal measurements, the concentrations of the different types of nanoparticle solutions were adjusted to the same level with the aid of a

Nanosight LM10 via the procedure described in the instrument technical notes which has been described in Section 2.2.2. The required dilution factor was then applied to the rest of the samples.

Investigations into the SERS properties of HGNs and citrate reduced gold and silver nanoparticles at 1064 nm excitation were carried out by mixing 140 µL of the nanparticle solution with 10 µL of 1.5 µM 4,4′-Azopyridine (Sigma-Aldrich) in water. This was followed by 150 µL of distilled water or 100 mM KCl solution; the samples were left for 8 min before SERS measurements. The Raman measurements at 1064 nm excitation wavelength were made using a Real Time Analyzer FT-Raman spectrometer. A 10 s acquisition time with a laser power of 420 mW was used for all measurements.

The photothermal studies were carried out on an instrument of in-house design. Briefly, a 785 nm fibre coupled laser (B&W TEK Inc, USA) was used. The laser, with a power of 250 mW, was focused into a 1 cm sample cuvette using a standard f=100 mm UV fused silica plano-convex lens (1” diameter). The micro cuvette contained 700 µL of ~0.2 nM nanoparticle suspension. A thermocouple from a heating mantle was inserted into the solution perpendicular to the path of the laser light, ~1.5 cm above the laser focus point. The temperature was allowed to stabilize for 3 min before the laser block was removed and the solution illuminated, it was then measured over a period of 45 min with water forming the control.

3.3. Results and Discussion

3.3.1. Comparison of SERS properties of hollow gold nanospheres and standard gold and silver nanospheres at 1064 nm excitation

Three different types of HGNs with LSPRs of 650, 775 and 1080 nm (HGN-650, HGN-775, HGN-1080), as well as citrate reduced gold and silver nanoparticles were mixed with 4,4’-azopyridine at a final concentration of 100 nM which is a non-resonant Raman reporter at 1064 nm excitation. To make a reliable comparison, several parameters of the nanoparticles were tuned; such as particle concentrations, zeta potentials and average particle sizes (Table 2).

Table 2. Physical details about the nanoparticles.

	Zeta potentials (mv)	Outer Diameters (nm)	Shell thickness (nm)	Concentrations (particles/mL)
Ag nanoparticles	-40.8±3.20	46±2	NA	2.02×10^{11}
Au nanoparticles	-40.2±3.15	45±5	NA	1.92×10^{11}
HGN 650	-42.9±3.36	53±8	8.3 ± 0.6	1.89×10^{11}
HGN 775	-42.0±3.48	66±11	6.5 ± 1.3	$\sim1.99\times10^{11}$
HGN 1080	-39.1±3.27	67±14	NA	$\sim2.28\times10^{11}$

The average particle sizes were obtained by counting at least 200 nanoparticles from the SEM images using Image J. Particle concentrations were tuned with the aid of the Nanosight. Due to the limitation of the laser excitation wavelength (685 nm) inside the nanosight instrument, it is not sensitive enough to give accurate concentration results for nanoparticles with a LSPR larger than 800 nm and therefore these are approximate values. As shown in Figure 31, no SERS signals were observed when the nanoparticles existed as monomeric suspensions for any of the nanoparticles. This is due to the combinition of the weak enhancement from the individual nanoparticles and the longer excitation wavelength used. From Figure 32, after the addition of 100 mM potassium chloride, a strong SERS signal was observed using 1064 nm excitation from HGN-650 and a weaker, yet observable signal was detected from HGN-775. However, no obvious signals were observed in the case of standard gold, silver or HGN-1080.

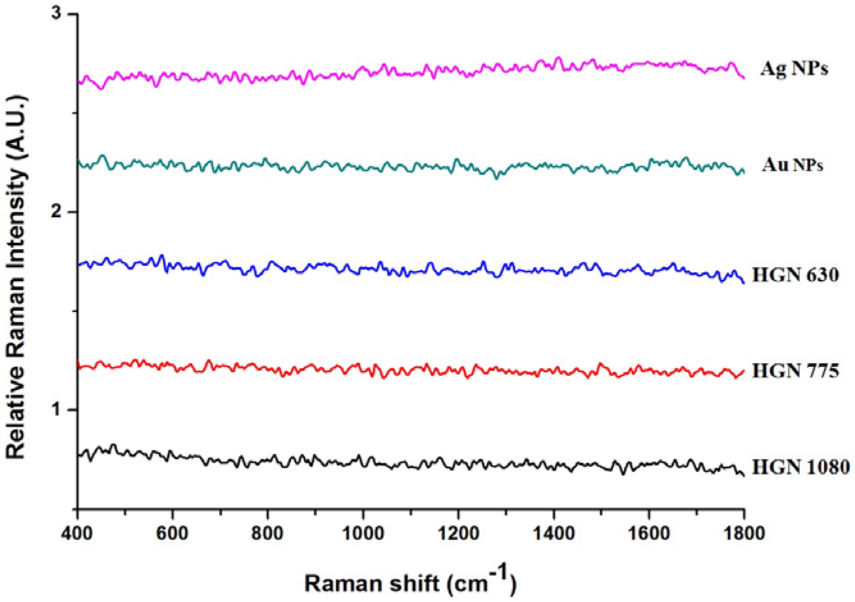

Figure 31. SERS spectra of 4,4’-azopyridine adsorbed onto the different types of nanoparticle suspensions, spectra were recorded at 1064 nm excitation with no additional salt. HGN 650, HGN 775, and HGN 1080 mean hollow gold nanospheres with LSPRs of 650, 775, and 1080 nm respectively.

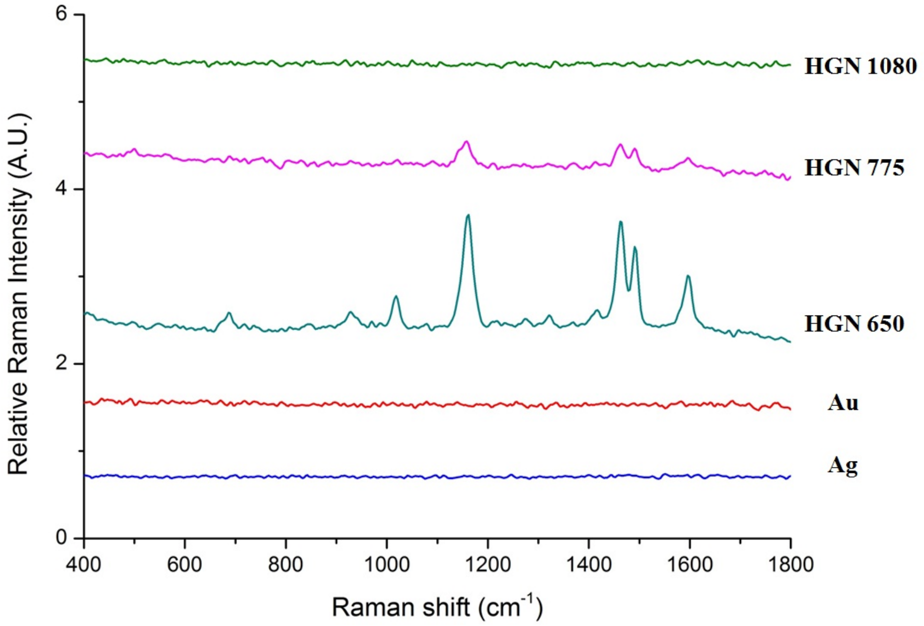

Figure 32. SERS spectra of 4,4’-azopyridine with different types of nanoparticle suspensions at 1064 nm excitation after the addition of potassium chloride. HGN-650, HGN-775 and HGN-1080 refer to hollow gold nanopsheres with LSPRs of 650, 775 and 1080 nm respectively.

Salt induced aggregation creates SERS “hot spots” which are highly localized EM fields between metal nanoparticles, molecules placed in these areas generate large Raman signals.[81] Therefore, after the addition of 100 mM potassium chloride, “hot spots” were formed which allowed the SERS signals for some of the nanoparticles to be obtained using 1064 nm excitation wavelength. The characteristic peaks of 4,4’-azopyridine are in the region of 650 cm^{-1} to 1650 cm^{-1} which equates to a Stokes-shifted range, with a 1064 nm excitation source of 1143 to 1290 nm. The extinction spectra of the nanoparticles before and after the addition of salt are shown in Figure 33. In the region of 1143 to 1290 nm, the extinction values of aggregated HGNs are much larger than the values of aggregated gold and silver nanoparticles. The extinction spectrum is the combination of scattering and absorption properties of the sample, and the scattering effect dominates in terms of SERS. Based on figure 3a, both the scattering and absorption properties of Au and Ag nanoparticles at 1064 nm are weak. However, for hollow gold nanospheres, with more red-shifted LSPRs, the absorption value dominates the overall extinction value,[125] this is one reason why HGN-775 and HGN-1080 have higher extinction values in the 1143-1290 nm region, but generated weaker or non-observable SERS signals compared to HGN-650. As mentioned in section 2.3.2.4, based on the recent electric field simulation of hollow gold nanospheres, the outer electric field decreased when the shell became thinner compared to particles with thicker shells,[118] and the surface cavities which were observed in the HGNs with NIR LSPRs are too big to play a role in enhancing the surface electric field. Recently, Gibson *et al* performed SERS mapping on silver nanotriangle arrays and correlated these with AFM images.[126] The correlated images revealed that the highest intensity of Raman scattering came from the network of Ag triangles and the holes (gaps) in the arrays demonstrated no Raman amplification.[126] Although our current system is different from the reported substrate, the structural similarity provides evidence that highly porous noble metallic nanoparticles are not good SERS substrates. Therefore, it is reasonable to expect the HGNs with more red-shifted LSPRs will generate weaker SERS enhancement under the same conditions compared to HGNs with LSPRs close to the visible range with respect to the 1064 nm excitation source.

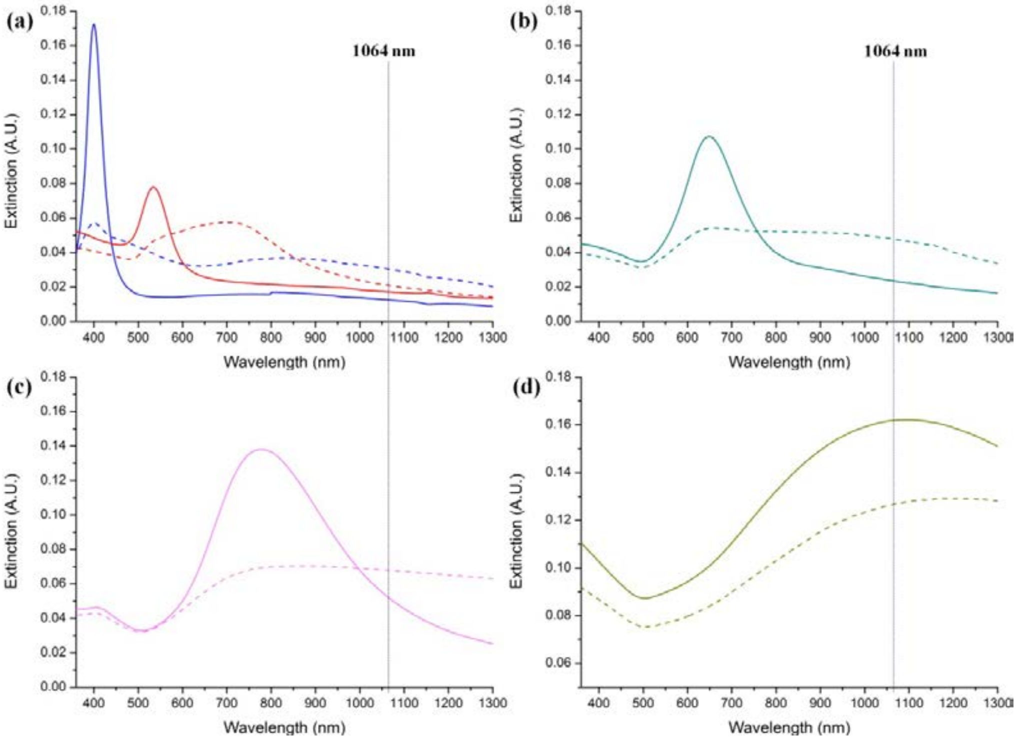

Figure 33. Extinction spectra of different types of nanoparticle suspensions before (solid lines) and after (dashed lines) the addition of 100 mM potassium chloride. a) citrate reduced silver (blue lines) and gold (red lines) nanoparticles; b) HGN-650; c) HGN-775; d) HGN-1080.

3.3.2. Comparison of photothermal properties of hollow gold nanoshperes and standard gold and silver nanoshperes

The photothermal effect is a process where by a suitable material converts incident photons into heat therefore it is highly dependent on the absorption properties of the materials under study. Due to the interest in photothermal therapies using HGNs, the photothermal properties of these new red-shifted HGNs were investigated. The HGN suspensions, which had been normalized to have similar concentrations of ~0.2 nM, were compared to standard citrate reduced gold and silver nanoparticles. The samples (700 µL) were illuminated by a continuous laser source at 785 nm excitation, which is the most common excitation source for NIR imaging, for 45 min. It should be noted, the thermocouple was 1.5 cm above the laser beam to avoid direct exposure to the beam; therefore the measured temperatures were from the bulk solution. From Figure 34, HGNs resonant with the excitation wavelength elevated the solution temperature from 20 °C to 50 °C within 45 min while standard citrate reduced gold and silver nanoparticles only elevated the temperature 3.9 °C and 3.3 °C above the control (water) respectively. Although HGN-1080 was further away from the excitation wavelength compared to HGN-650, the HGN-1080 sample resulted in a significantly higher temperature than the HGN-650 sample. This is consistent with the previous discussion that for red-shifted HGNs, the absorption value dominates the overall extinction value and in this case generates more heat under the same conditions. The extinction spectra of these nanoparticle suspensions before and after the photothermal study are shown in Figure 35. At 785nm the absobance of HGN-1080 is larger than HGN-650 which explains the reason that HGN-1080 generated higher temperature than HGN-650 at 785 nm excitation. In addition, there was no obvious change for any of the spectra after being illuminated by a continuous 785 nm laser source for 45 min suggesting the original nanostructures were not damaged.

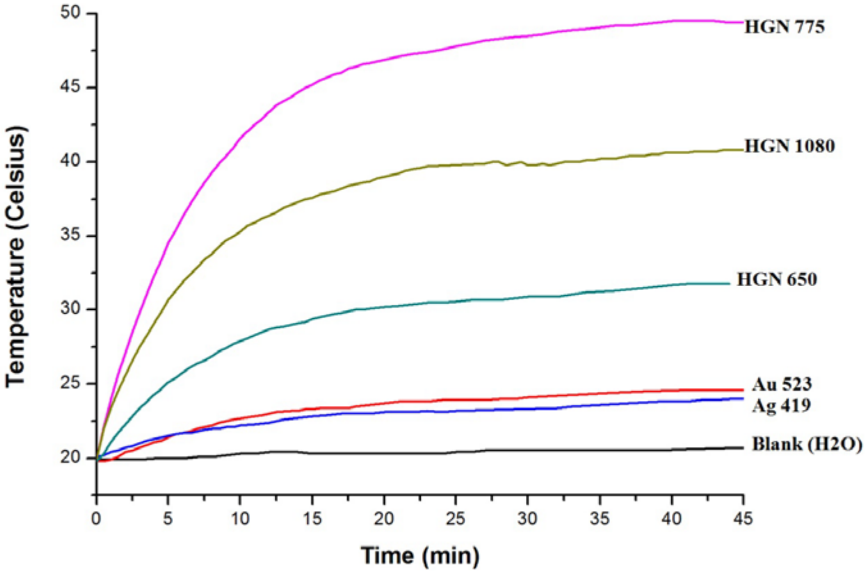

Figure 34. Photothermal study of the different types of nanoparticles. The colloid suspensions were illuminated by a 250 mW continuous laser at 785 nm for 45 min. The recording interval was 30 s during the first 15 min and 1 min there after.

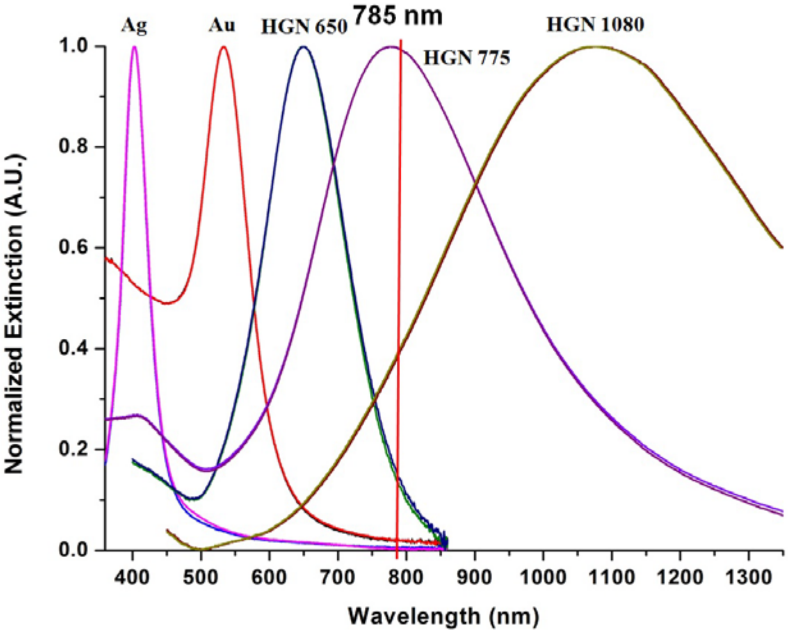

Figure 35. Normalized extinction spectra of the different types of nanoparticle suspensions before and after being illumination by a continuous 785 nm laser for 45 min. Most part of the spectra (before and after the illumination) are overlaid and there are only slight changes in the longer wavelength regions of the traces.

3.3.3. Derivation of the absorption efficiency

The photothermal efficiency of a nanoparticle is related to its ability to convert an absorbed photon into heat. However, the absorption efficiency value of the nanoparticle provides the upper threshold for the photothermal efficiency, i.e. the photothermal efficiency is calculated with respect to the absorbed photons not the photons that are being delivered to the sample. Therefore, any material with a larger absorption efficiency will possess a greater potential photothermal effect at the same laser power i.e. a greater temperature increase (as we experimentally demonstrated in this paper) or the same photothermal effect at a lower laser power.

The experimental absorption efficiency η is determined by equation 1 ,

$$\eta = \frac{C_{water} \times m_{water} \times \Delta T}{N_A \times C_{NPs} \times V \times CSA_{NPs} \times P \times t} \tag{1}$$

where C_{water} is the specific heat capacity of water; m_{water} is the mass of water; ΔT is the temperature change; N_A is Avogadro constant; C_{NPs} is the concentration of the nanoparticles; V is the illuminated volume; CSA_{NPs} is the cross sectional area of a nanoparticle; P is the power density of the illuminated volume and t is the illumination time. To deduce this equation, the following approximations were made: all the incident photons falling on a nanoparticle are absorbed; the loss of heat to the surroundings is minimal and the Brownian motion of the nanoparticles did not influence the experimental result. The detailed derivation of this equation is shown below.

Volume of the focus beam $V = 3.21 \times \lambda^3 \times \left(\frac{f}{D}\right)^4$ (2)

The focal length of field penetration of the laser into the sample

$$h = n \times \frac{\lambda}{N.A.^2} \tag{3}$$

$$N.A. = \frac{1}{2 \times f_{ND}} \tag{4}$$

$$f_{ND} = \frac{f}{D} \tag{5}$$

Cross sectional area of the laser beam (CSA)= $\frac{V}{h}$ (6)

Power density in the focus area= $\frac{laser\ power}{CSA}$ (7)

CSA of a nanoparticle = $\pi \times r^2$ (8)

Work= CSA of nanoparticle × Power density × Time (9)

Number of nanoparticles= $N_A \times C \times V$ (10)

Total theoretical work= Work× Number of nanoparticles (11)

Actual work=$C_{water} \times m_{water} \times \Delta T$ (12)

Efficiency η=$\frac{Actual\ work}{Total\ theorectical\ work}$ (13)

$$\eta = \frac{C_{water} \times m_{water} \times \Delta T \times D^2}{4 \times N_A \times C \times \pi r^2 \times n \times P \times \lambda \times f^2 t} \quad (14)$$

λ is the excitation wavelength; f is the focal length; D is the lens diameter; n is the refractive index of the surrounding media; N.A. is the numerical aperture; r is the average radius of the nanoparticles; C is the concentration of the nanoparticles. Equations 2-5 are from Ref. 120.

To test the accuracy of this equation, the efficiencies of gold and silver nanoparticles were firstly calculated. Absorption efficiency values of 0.16% for gold and 0.12% for silver were obtained which closely matches the previous simulation results carried out at 785 nm excitation.[127] Finally, the absorption efficiency of the most photothermally active HGN, HGN-775 was calculated to be 0.81% which is more than 5 times higher than the efficiency of gold nanoparticles under the same conditions. To be noted, the values we are discussing are the absorption efficiencies, however for gold nanoparticles with an absorption efficiency of 0.16% the photothermal efficiency has been recorded as ~80%.[127] This means that 80% of the photons absorbed are converted to thermal energy, however only 0.16% of the total photons entering the sample are absorbed. Therefore even if the photothermal efficiency of the HGN-775 sample was less than the gold nanoparticles, due to the larger absorption efficiency, i.e. the greater number of photons the material can absorb, it should still result in a greater photothermal effect. However, to produce an actual photothermal value, the theoretical absorption efficiency of the prepared novel nanoshells would need to be calculated, this is a focus of future work in our lab. Recently, Chen *et al.* investigated the photothermal conversion efficiencies of gold nanocrystals including different sizes of nanorods and nanospheres.[128] Gold nanorods resonant with the excitation wavelength showed the highest photothermal conversion efficiency up to 95%, however, as mentioned previously, these nanorods were covered by surfactants which are toxic and not easy to replace. In addition, in our system, the concentration of each nanoparticle suspension was tuned to be the same and each type of nanoparticles had similar surface properties, which makes our comparison more robust.

3.4. Conclusions

In this chapter, the scattering properties of different types of hollow gold nanospheres were demonstrated through their surface enhanced Raman scattering (SERS) activity at 1064 nm excitation wavelength and compared to standard gold and silver nanoparticles of similar physical size and surface properties. After the addition of salt, a strong SERS signal was observed from hollow gold with a LSPR of 650 nm and a weaker SERS signal from HGNs with a LSPR of 775 nm. However, no obvious SERS signals were observed in the case of standard gold, silver or HGN with a LSPR of 1080 nm. This is due to the combined effects of the different extinction values in the range of 1143 to 1290 nm and the surface structure of the HGNs with a LSPR of 1080 nm. The absorption properties of HGNs are exhibited by their photothermal response. Different nanoparticle solutions including standard gold, silver, and HGNs were illuminated by a continuous laser source at 785 nm excitation wavelength for 45 min and the absorption efficiencies were found to be 0.16%, 0.12% and 0.81% (HGN-775) respectively. HGNs will make superior substrates over standard solid nanoparticle substrates for photothermal and SERS applications and the detailed synthesis described in the previous chapter can be used to tune the SPR to the required position allowing their activity to be maximized.

Chapter 4. Deciphering SERS Properties of Gold Nanoworms and Their Applications

During the synthesis of individual HGNs, a chain structure consisting of connected HGNs were accidently obtained. In chapter 4, we will discuss the SERS properties of these interesting structures and illustrate the relationship between nanostructures and SERS activities through the optical correlations.

4.1. Introduction

SERS "Hot spots" are the regions where the electromagnetic field is significantly enhanced beyond the average field intensity surrounding a nanoparticle and results in much greater SERS activity from these areas. The hottest sites (with local enhancement factors > 10^9) account for just 63 in 1,000,000 of the total potential sites but contribute 24% to the overall SERS intensity.[81] Therefore, creating and exploring "hot spot" structures has attracted much attention.

So far, a lot of work has focused on building dimers and trimers of metallic nanoparticles which are the basic units for SERS "hot spots". Chen *et al.* used differential centrifugation to produce dimer and trimer enriched solutions of Au-Ag core-shell nanoparticles for a SERS study.[129] Reich and co-workers obtained SERS-active silver nanoparticles through controlled linking, polymer encapsulation and small-molecule infusion.[130] In order to investigate the SERS "hot spot" structure, SERS maps have been previously correlated with TEM images of salt induced silver nanoparticle aggregates and reported the relative SERS activities.[131] The resulting SERS-active order was found to be: aggregates of 10-20 silver particles > aggregates of 4-9 particles > trimers > dimers > single particles.[131] Recently, Van Duyne and co-workers probed the SERS "hot spot" structures required for single molecule detection[132] and described the relationship between structure and SERS activity for gold nanoparticle dimers and trimers.[84] The most active "hot spots" were found to be two particles which were in subnanometer proximity or had fully coalesced to form crevices.[84] Although dimer and trimer SERS systems have been well interrogated, the exploration of higher order SERS-active structures in a non-uniform nanosystem is still rare.

SERS substrates are generally based on noble metals and their enhancement relies on the optical absorption of the formed substrate.[19] Hollow gold nanospheres are particularly good SERS substrates in the near infrared region as they exhibit a tunable localised surface plasmon resonance from 550 nm to 820 nm by controlling their inner diameter and wall thickness.[60,111] Generally, single hollow gold nanospheres have a lower Raman activity than that obtained from random aggregates of silver or gold nanoparticles however their SERS responses are more uniform than any other nanoparticle substrate.[104] While different shapes and sizes of noble metal nanoparticles have been achieved, manipulation of these particles into higher ordered structures remains challenging.[133] Recently, Schwartzberg *et al.* reported that gold nanotubes could be formed during the synthesis of hollow gold nanospheres in the presence of a relatively strong magnetic field.[109] This work focused on the synthesis and possible formation mechanism. In the first part of this chapter, we use the formed chain structures as a basis for a SERS investigation and add to the growing body of evidence in relation to nanostructures and surface enhancement of Raman scattering.

Unlike colloidal suspensions, immobilization of nanoparticles onto a two dimensional planar substrate can provide a fixed geometry, as opposed to the complex dynamics that may exist in colloidal solutions.[19] This can provide a consistent enhancement from the probe volume unlike the ever-changing enhancement seen in solution where different sized aggregates can diffuse in and out of the laser spot. Such consistency with respect to enhancement is important for fundamental SERS studies.

Solid SERS substrates fabricated from electron beam lithography[134] and nanosphere lithography[135] generate well-controlled substrates with high SERS enhancement factors. However, the cost of the required instrumentation hinders their wider application. Placing nanoparticles on a porous substrate to create a SERS-active substrate has been applied to flow systems for biological applications.[136]

Several attempts have been made to fabricate a SERS-active porous substrate.[137] Xu *et al.* directly reduced silver ions on an Au-supported polyaniline membrane.[138] These homogeneous three-dimensional Ag nanostructures were found to be highly efficient SERS substrates. Silver or gold has been deposited on different nanoporous templates such as ceramics[139] and anodic alumina oxides[140] with notable SERS effects being obtained. However, fabrication of these substrates requires a relatively complicated process. Recently, gold nanorods adsorbed on filter paper were used for trace detection using SERS.[141] Although it provides a cost-effective SERS substrate, preparation of this substrate takes two days to allow sufficient coverage of nanorods and a strong Raman background was observed from the filter paper, which limits its applications.

In the second part of this chapter, the use of gold nanoworms as the basic SERS enhancing unit, coupled with assembly on a membrane by simple filtration to produce a large SERS response is investigated. Gold nanoworms are immobilised on a commercial membrane surface by simple filtration. The interactions between individual nanoworms resulted in additional SERS enhancement compare to the SERS performance of individual nanoworms on ITO glass substrates. In addition, the order of analyte introduction into the immobilized nanoworm system is also investigated.

4.2. Experimental

4.2.1. Synthesis of gold nanoworms

The synthesis of gold nanoworms was carried out in a standard Schlenk line under Ar, and the procedure was similar to that of gold nanotubes reported by Schwartzberg *et al.*.[109] In a typical synthesis, 100 µL of 0.4 M cobalt chloride hexahydrate (Fisher Scientific, 99.99%) and 100 µL of 0.1 M trisodium citrate dihydrate (Sigma-Aldrich, >99%) were added into 100 mL of deionized water and degassed several times. 1 mL of 0.1 M sodium borohydride (Fisher Scientific, 99%) was injected into the solution in the presence of an external magnetic field. This solution was allowed to react for 50 min, (under constant argon flow) until hydrogen evolution ceased, indicating complete hydrolysis of the reductant. The external magnetic field was then removed and 33 mL of 2.5×10^{-4} M chloroauric acid trihydrate (Fisher Scientific, ACS reagent grade) was injected under vigorous stirring. This mixture was reacted for a further 10 min under argon before being exposed to air until a colour change (from grey to light green) was observed. Finally, 500 µL of 0.1 M sodium citrate was added to stabilize the gold nanoworms.

After synthesis, the solution was filtered (Fisher Scientific qualitative filter paper) and concentrated through centrifugation (3466 ×g). The precipitate was redispersed into 10 mL of 0.6 mM sodium citrate solution.

Investigations into SERS properties of gold nanoworms were carried out by mixing 250 µL of the concentrated gold nanoworm solution, 245 µL of deionized water and 5 µL of different Raman reporters: 10^{-4} M 4-mercaptobenzoic acid (Sigma-Aldrich, 90%) in ethanol, 10^{-4} M NIR-797 isothiocyanate (Sigma-Aldrich, ≥70%) in ethanol, and 1.2×10^{-5} M Malachite green isothiocyanate (Sigma-Aldrich, ≥96.0%) in ethanol. For multiplexing, a mixture of 4-mercaptobenzoic acid and Malachite green isothiocyanate was added into a diluted nanoworm solution.

4.2.2. Characterization of nanoworms

Two excitation wavelengths, 632.8 and 785 nm, were used in the corresponding SERS studies. 632.8 nm solution SERS spectra were recorded using a Renishaw Ramanscope System 2000 and the 632.8 nm line of a helium-neon laser as the excitation source and an Olympus 20×/NA0.4 long-working distance objective for excitation and signal collection in a 180° backscattering geometry from a microcuvette. The unfocused power output was measured to be approximately 4.8 mW at the sample. Dielectric edge filters were used to reject the Rayleigh scattered light. Spectra were accumulated for 10 s, and 5 replicates were carried out at each sample point; the signals were normalized to a silicon standard.

785 nm solution SERS spectra were recorded on a 785 nm fibre optically coupled probe system attached to a Renishaw inVia microscope system. Using an f18 focussing/collection lens, power at the sample was measured at approximately 90 mW and a 1200 groove diffraction grating was used. Spectra were accumulated for 10 s, and 5 replicates were carried out at each sample point; the signals were normalized to a cyclohexane standard.

Solid phase SERS was carried out on polyelectrolyte functionalized indium tin oxide (ITO) coated glass slides.[108] The detailed description has been shown in section 2.2.2. 100 μL of each sample was put onto the PDDA functionalized ITO coated glass surface for half an hour under a water saturated atmosphere. The sample was then washed off and dried in a N_2 flow. A TEM copper grid was mounted over each sample for indexing purposes. The SERS maps and dark-field images were performed on a WITec alpha300-R equipped with a MPLanFL N 100×/NA 0.9 for SERS mappings and a ZEISS EC EPOPLAN dark-field 50×/NA 0.7 for dark-field imaging. A 632.8 nm line of a helium-neon laser with a power of ~ 250 μW and a 785 nm line of a diode laser with a power of ~ 750 μW were used as the excitation sources. The integration time per point was 0.25s for 632.8 nm maps and 0.3s for 785 nm maps. The geometry of scanned areas was 25 μm × 25 μm with 50 points per line.

SEM correlations were carried out on a Sirion 200 Schottky field-emission electron microscope operating at an accelerating voltage of 5 kV. The samples did not require additional metallic coating before imaging except the membrane samples which required additional gold sputter coating. The samples were investigated at high resolution using a scanning/transmission electron microscope (S/TEM – FEI Titan 80-300) operated at 300 kV. It is equipped with a Cs-corrector on the imaging lens and a post-column electron energy-loss spectrometer (Gatan Tridiem 865). Electron energy-loss spectra (EELS) were acquired using convergence and collection angles of 13 mrad and 21 mrad, respectively.

4.2.3. Pre-functionalization of nanoworms for membrane study

2.5 mL of the concentrated gold nanoworm solution, 2.45 mL of deionized water and 50 μL of different concentrations (10^{-4} and 10^{-5} M) of 4-mercaptobenzoic acid (in ethanol) were mixed together followed by 10 seconds of vortexing and left for 30 minutes before measurements were taken.

4.2.4. Fabrication of nanoworm membrane

5 mL of pre-functionalized nanoworm solution was filtered using a polyvinylidene fluoride (PVDF) 13 mm diameter membrane with a pore size of 450 nm (Fisher Scientific FDR-272-010X). The membrane was then rinsed with deionized water and dried under nitrogen before measurements.

4.2.5. Post-functionalization of nanoworm membrane

5 mL of non-functionalised nanoworm solution was immobilised onto a membrane and then immersed into 5 mL of 10^{-6} M of 4-MBA water solution for 30 minutes. It was then rinsed with deionised water and dried under nitrogen before measurements.

4.3. Results and Discussion

4.3.1. Synthesis of gold nanoworms

During the synthesis of individual hollow gold nanospheres, some chain structures were accidentally found in the presence of a magnetic stirrer. One of them is shown in Figure 36. Hollow gold nanoparticles in this image are fused together to form a worm structure with a length of 5 um.

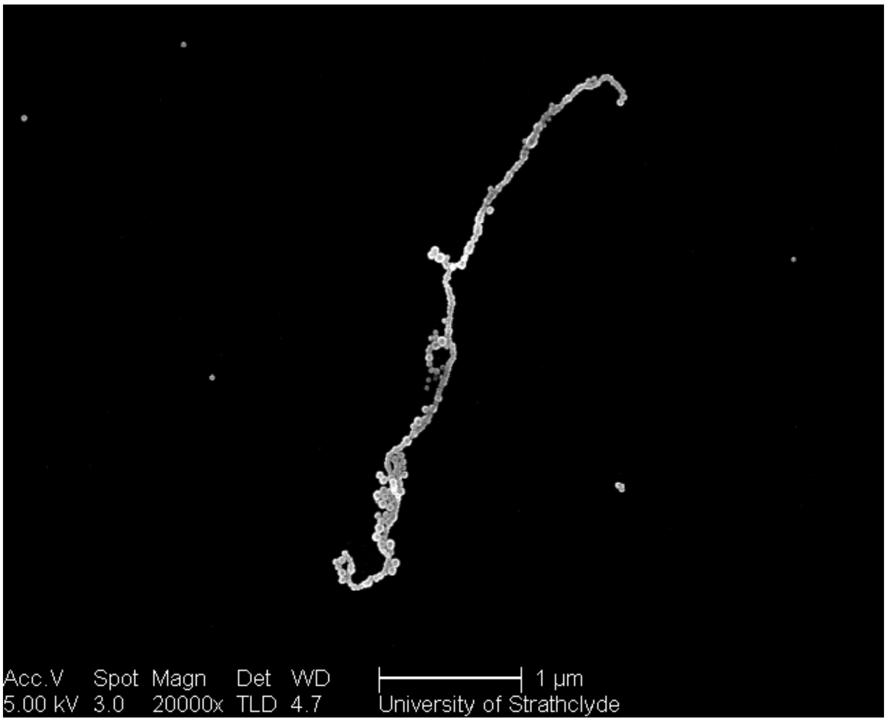

Figure 36 SEM image of a typical nanoworm synthesized under external magnetic field.

There are two reasons for the formation of this chain structure. First, it is due to the presence of the external magnetic field. With increasing the intensity of the magnetic field, the ratio of chain structure increases. However, this structure can not be obtained all the time, even under a strong external magnetic field. Therefore, there must be some other factors to affect the formation. The most probable reason is the amount of sodium citrate which plays a complexation role during the reaction.

To test this hypothesis, experiments using different amounts of sodium citrate under the same conditions were performed.

From Figure 37, for the sample of 600 μL 0.1 M sodium citrate, no chain structure is observed. However, decreasing the amount of sodium citrate increases the percentage of chain structures. For the sample using 100 μL of 0.1 M sodium citrate, the majority are long chain structures. However, if there is no sodium citrate presented, only black sediments (aggregated Co nanoparticles) were found and formed a colourless solution suggesting the stabilization function of citrate. When the insufficient amount of citrate ions was present, their coordination with cobalt ions in the suspension was not complete. After these incomplete cobalt ions being reduced into Co nanoparticles, they can be easily manipulated by the external magnetic field.

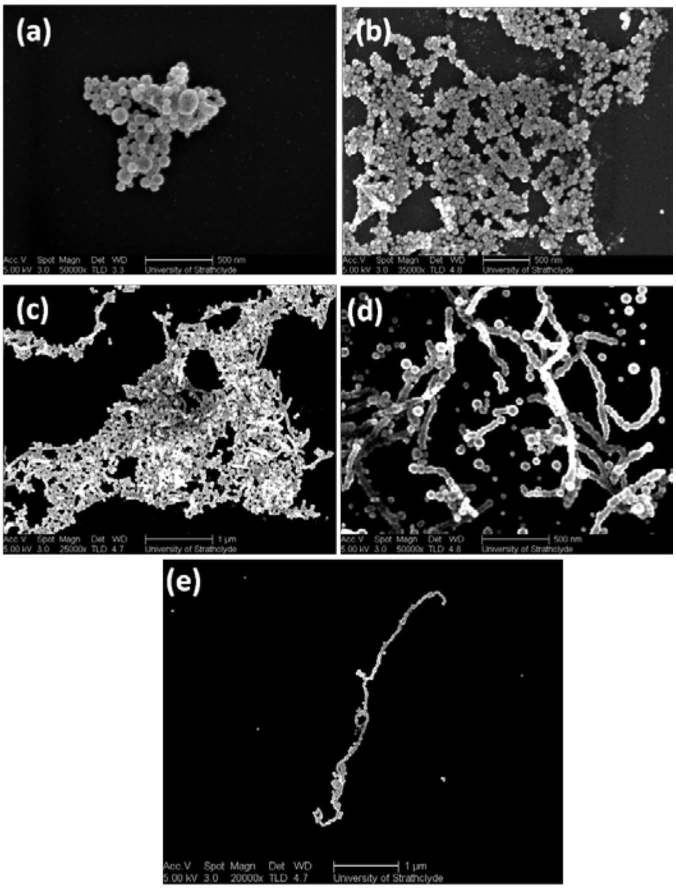

Figure 37 SEM images of samples with different amount of sodium citrate under the same conditions. A) 600 µL B) 400 µL C) 300 µL D) 200 µL E) 100 µL 0.1 M sodium Citrate.

The probable mechanism of formation of the chain structure under an external magnetic field is shown in Figure 38. Followed by the injection of sodium borohydride, cobalt ions will be reduced to magnetic Co NPs which align according to the magnetic field. After the addition of chloroauric acid trihydrate to the Co NP suspension, gold ions are reduced onto the surface of aligned cobalt particles forming the nanoshell. In the final stage, cobalt naopartices will be oxidized by dissolved oxygen forming the hollow structure.

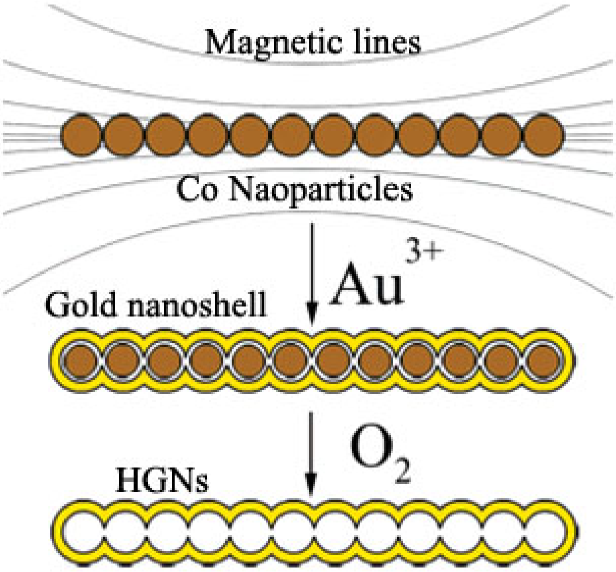

Figure 38 Schematic of the formation of chain hollow structure.[109]

4.3.1Characterization of gold nanoworms

The bright field TEM image (Figure 39a) of a single chain exhibits contrast that is consistent with the chain being formed from hollow gold nanoparticles. The circle of dark contrast corresponds to the shell being approximately aligned along the electron beam direction and suggests that the inner diameter of the HGNs are in the range of 20-60 nm, with an average wall thickness of approximately 8 nm (Figure 40). The lack of dark contrast at the contact point of some adjacent HGNs suggest that some parts of the nanoworm are tube-like as previously reported.[109] However, in most cases it is clear that the nanoworms are formed by connection of individual hollow nanospheres without the loss of the wall between them which could have important implications for their resultant SERS activity. The STEM high-angle annular dark field image, which is sensitive to atomic number, shown in Figure 39b further confirms that the majority of nanoworms are made up of connected individual hollow nanospheres without loss of the joining wall. The composition of the nanoworm was investigated using electron energy-loss spectroscopy (EELS), and no evidence of cobalt or oxygen was found at any position along the line of the spectrum image indicated by the arrow in Figure 39b (Figure 41).

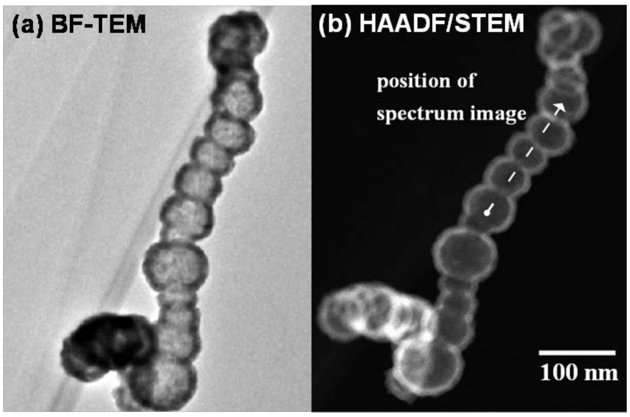

Figure 39. Electron microscopy study of a single nanoworm chain. (a) Bright field (BF) transmission electron micrograph, and (b) the corresponding high angle annular dark-field (HAADF) image illustrating the position and direction of the EEL spectrum image.

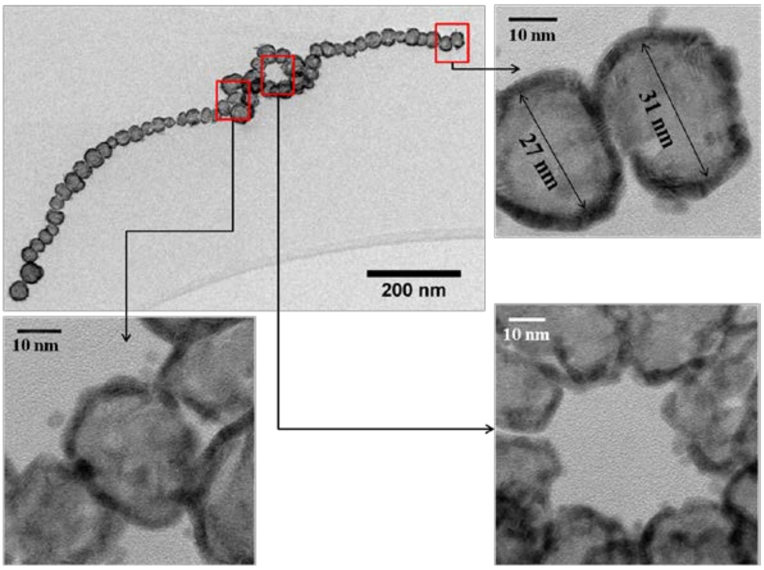

Figure 40. TEM image of a typical gold nanoworm with HRTEM images of constituent parts.

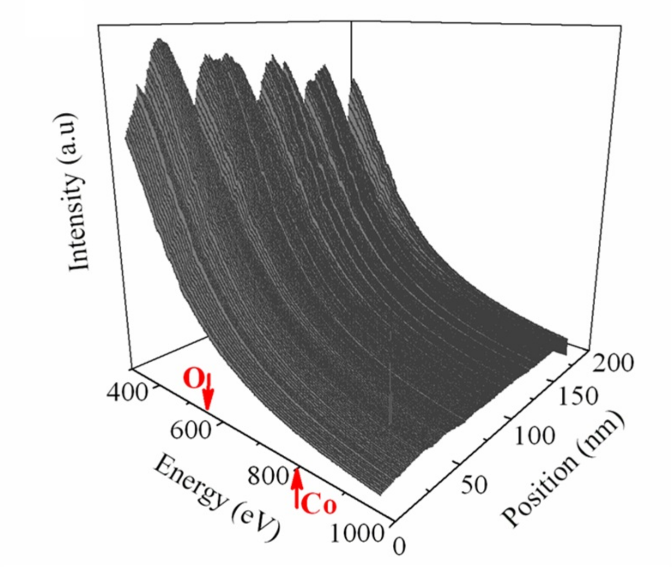

Figure 41. 3D surface plot representation of the EEL spectrum image. The arrows in (c) indicate the ionization edges for Co and O, which are absent from the spectra.

Interestingly, when a concentrated gold nanoworm solution was aged for more than 15 hours, two layers naturally formed, which could be discerned by eye. The upper fraction was light purple and consisted of individual nanospheres with an average diameter of 56 ± 18 nm which was calculated based on SEM imges. The bottom fraction was dark green and contained almost exclusively nanoworm structures of various lengths (Figure 42). The average diameter and the ensemble extinction spectrum of the upper fraction (Figure 43) indicate that these nanospheres are hollow.[61] Gravitation is the most likely cause for self-separation as the nanoworms are micrometers in length and therefore much heavier than the individual nanospheres. It should be noted that the proportion of the mixture that consists of HGNs as opposed to nanoworms depends on the levels of dissolved oxygen during synthesis. The proportion of individual particles will increase as the amount of dissolved oxygen present increases due to the oxidization of Co NPs. Therefore, to ensure reliable results during the subsequent analysis stages, the sample was shaken to ensure a homogeneous solution before every SERS experiment.

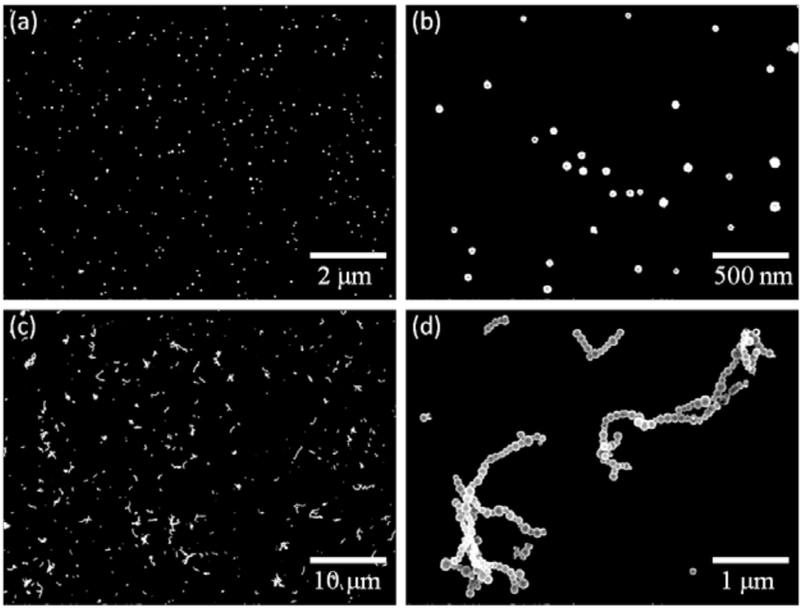

Figure 42. SEM images of naturally occurring fractions of a concentrated nanoworm solution. (a) a large scale SEM image of upper fraction; (b) detail of the upper fraction; (c) a large scale SEM image of the bottom fraction; (d) detail of the bottom fraction.

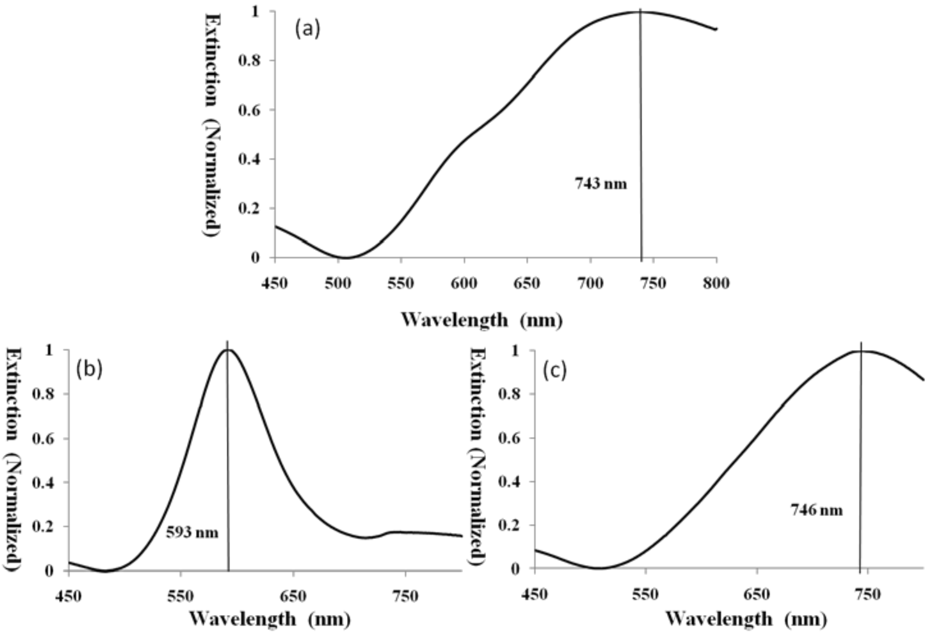

Figure 43. Extinction spectra of different fractions. (a) the ensemble nanoworm solution; (b) the upper fraction; (c) the bottom fraction.

4.3.2. Optimization of mapping conditions

To facilitate correlation between SERS mapping and SEM images, a TEM grid was fixed onto the indium tin oxide (ITO) glass surface as an indexing reference. ITO glass was chosen as a substrate due to its conductive surface essential for SEM, as well as its lower Raman background compared to silicon substrates. The drying of nanoparticle solutions results in the formation of large surface aggregates which are detrimental when trying to carry out correlation studies. Therefore, gold nanoworm solutions with different Raman reporter molecules were deposited on poly(diallyldimethylammonium) (PDDA) functionalized ITO glass surfaces, which were positively charged and could therefore capture the negatively charged gold nanoworms. Deposition was carried out under a water saturated atmosphere. The density of nanoworms on a substrate could be controlled by variation of the deposition time, which is a key parameter in terms of successful correlation. If the density is too low, the number of highly SERS-active areas tends to be low making correlation difficult. It was found that a deposition time of 30 minutes was optimal to achieve a suitable balance between correlation and density of highly SERS-active areas. A typical density illustration is shown in Figure 44, due to the micron dimensions of some of the nanoworms it was possible to observe them in bright field images (Figure 46 A). This allowed correlation of the optical and electron microscopy without the addition of positional markers as previously reported.[131]

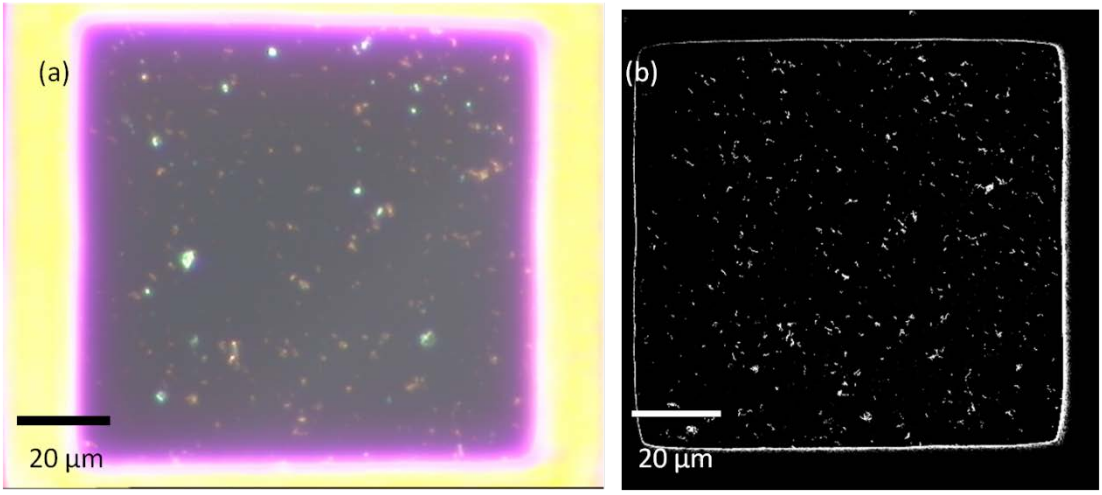

Figure 44. Demonstration of the coating density after half an hour. (a) dark-field image of one TEM square; (b) SEM image of the same square.

Laser power and integration time, not only determine the SERS intensity but also affect the scanned nanostructures. It was found that too high a laser intensity would alter the nanostructures and destroy their optical properties. Signals from the nanostructures became unreliable when their original morphology was changed. Figure 45 illustrates an example of a nanoworm melt by high laser power. Although a SERS signal was recorded during the first map, when a second scan was performed, there was no SERS signal from it. The laser power was therefore reduced to ~750 μW for 785 nm excitation and ~ 250 μW for 633 nm excitation and the integration time was decreased to 0.3s and 0.25s respectively. After optimization of these conditions, the mapping results obtained from the same area can be almost identical after a second scan.

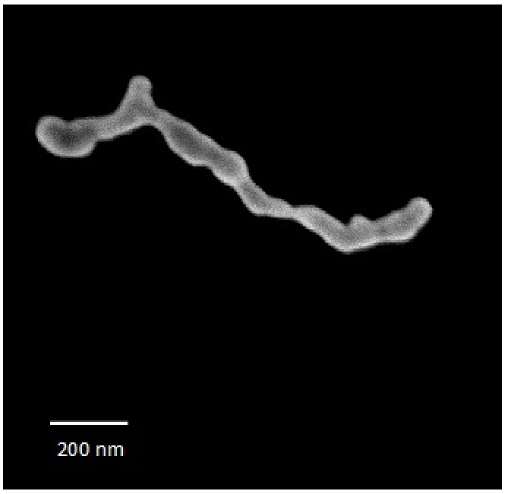

Figure 45. An example of a nanoworm when the laser power was too strong.

4.3.3. Correlation of SERS maps with SEM images

Three different types of Raman reporter molecules were used for SERS measurements. They were 4-mercaptobenzoic acid (MBA) which is non-resonant with the laser wavelengths used, Malachite green (MG) which is resonant with the 633 nm excitation and NIR-797 isothiocyanate which is resonant with the 785 nm excitation. The ensemble extinction spectrum of a nanoworm solution (Figure 43) shows a main peak at 743 nm and a small shoulder around 600 nm. Therefore, there will be some substrate resonance contribution with both laser wavelengths used in this study.

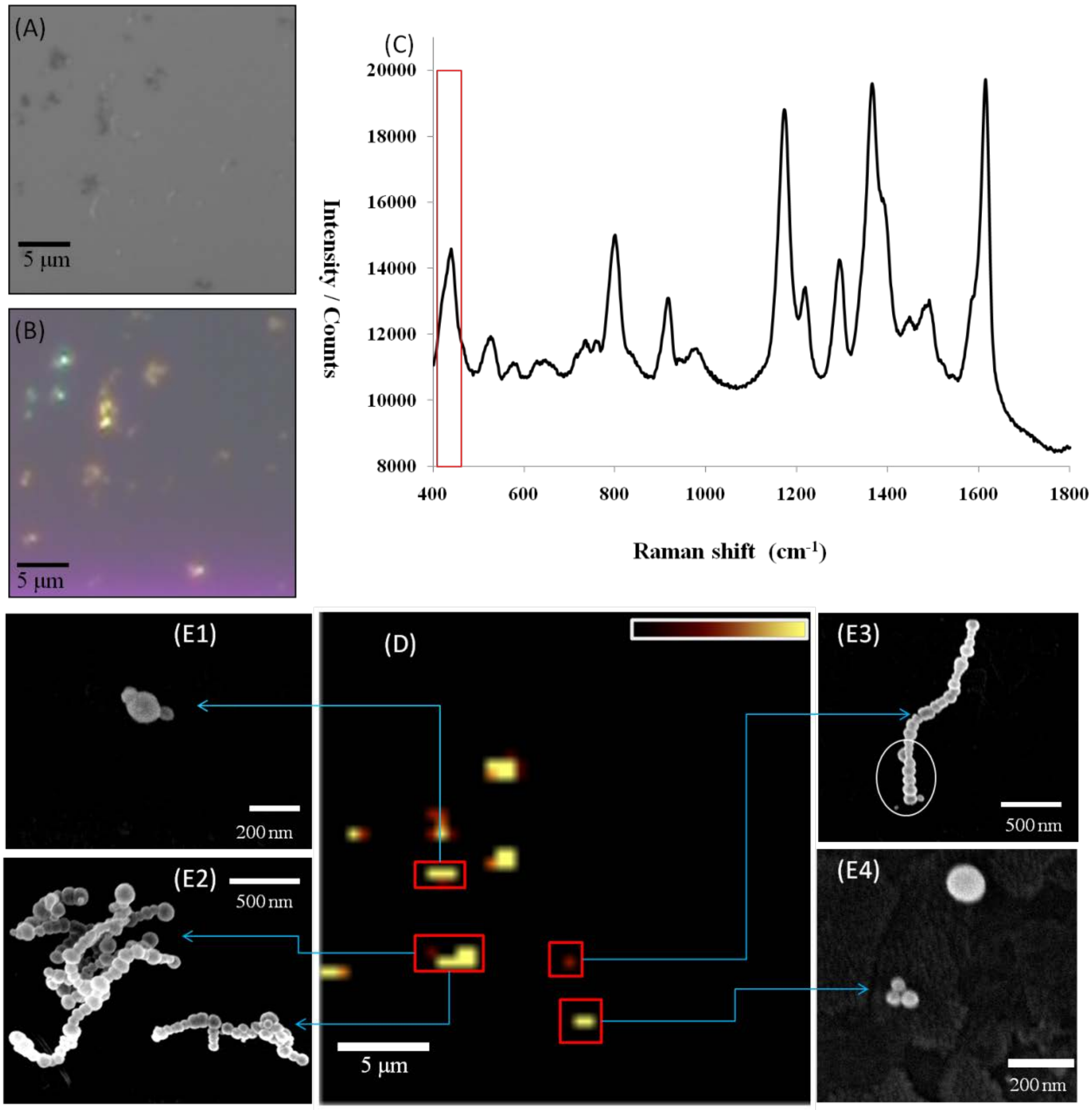

Figure 46. Correlation of a SERS map with SEM images. Malachite green was used as a resonant reporter molecule at 633 nm. (A) bright-field image of the mapping area; (B) dark-field image of the exact same area; (C) solution SERS spectrum of MG using 632.8 nm excitation. The marked peak was monitored in the SERS mapping; (D) SERS map of MG using 632.8 nm excitation; yellow indicates highest SERS intensity. (E) SEM images of correlated nanostructures.

Figure 46 shows the correlation between nanostructures and SERS intensity using 633 nm excitation and Malachite green. The dark-field image is particularly useful as the colour represents the scattering property of the nanostructures. In this case, the green and yellow/orange points observed in Figure 46B correlate to approximate scattering wavelengths of 540 nm and 590 nm for these nanostructures.[142] It should be noted that the LSPR of the same nanostructures in air are usually blue-shifted compared to those in water due to the changing of the refractive indexes of the media.[143] The red fringe in the dark-field image is due to reflection from the copper TEM grid. In addition, due to the optical limitations of our system, not all nanostructures were visible in both bright field and dark-field images.

ITO coated glass has a weak Raman background between 1200 cm^{-1} and 1600 cm^{-1}, therefore the peak between 400 and 450 cm^{-1} was monitored (Figure 46C). The intensity scale bar shown in the top right of Figure 46D indicates that the bright yellow spots represent the highest SERS intensity. The panels in E illustrate some nanostructures which gave different SERS activity. The intensity of the monitored peak for each structure was extracted from every pixel around the correlated spot to give an approximate quantitative comparison between different structures (Figure 47).

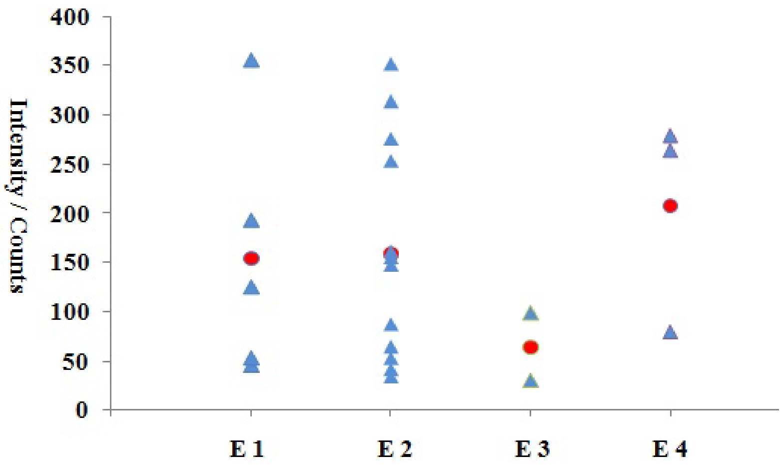

Figure 47. SERS intensity comparison of different nanostructures in Figure 46. The intensity values of the monitored peak were extracted from every relevant pixel. A red circle represents the average value of each nanostructure, and a blue triangle represents the peak intensity from the nanostructure at an individual pixel. However, more accurate results proabably can be obtained using statistic methods such as student's T test.[144]

Trimers in Figure 46 E1 and E4 showed strong SERS signals and this is confirmed by the extracted peak intensities (Figure 47). For E1, the diameter of the centre particle is around 100 nm and the two smaller nanospheres are 42 and 50 nm. And for E4, the diameters of the nanospheres are 42, 45 and 60 nm. The resolution of the reproduced image in Figure 46B is too low for these trimers to be clearly observed but through careful examination of the original image, it can be concluded that the LSPRs of these two trimers are close to 633 nm due to the yellow scattered light observed using dark field microscopy. Based on the densely packed structure, the interparticle gaps are very small which has previously been shown to be an essential condition to achieve maximum SERS enhancements.[84] In addition, the sizes of these trimers in the SERS map are larger than their physical sizes. This is due to the theoretical optical diffraction limit of the objective used being 352 nm for a 633 nm laser line. In fact, the actual value will likely be bigger than this. As described in Figure 48, the SERS signals can be generated when the laser spot is either positioned directly over the nanostructure or close to it, which leads to a blurring effect in the resultant maps.

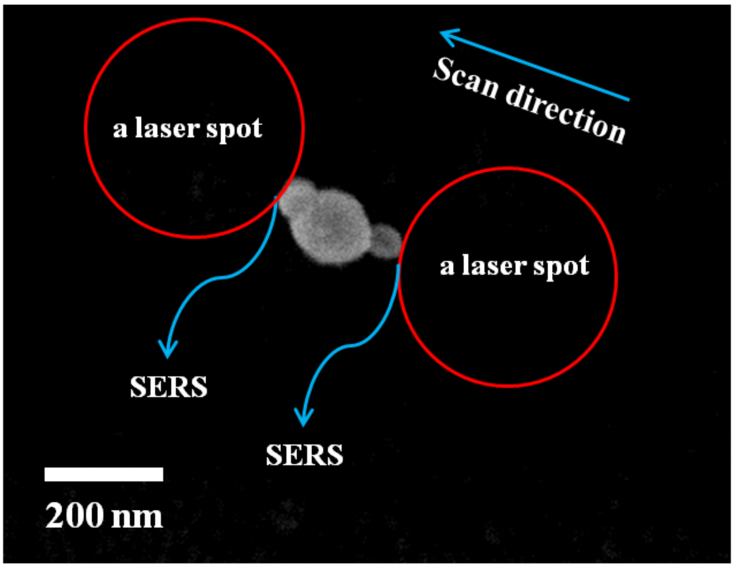

Figure 48. Schematic of deviation between the mapping size and actual size. For a 100×/N.A.0.9 objective, the theoretical optical diffraction limit is 352 nm with a 633 nm laser line and 436 nm with a 785 nm laser line respectively.

Owing to the deviations between size in the SERS map and actual size, the shapes shown in a SERS map cannot represent the actual shape of a nanostructure. Although only four SEM images are shown in Figure 46, all the visible spots in the mapped area were correlated with their SEM images (Figure 49), and no signal was observed from a single nanosphere which is consistent with previous reports.[84,131,132]

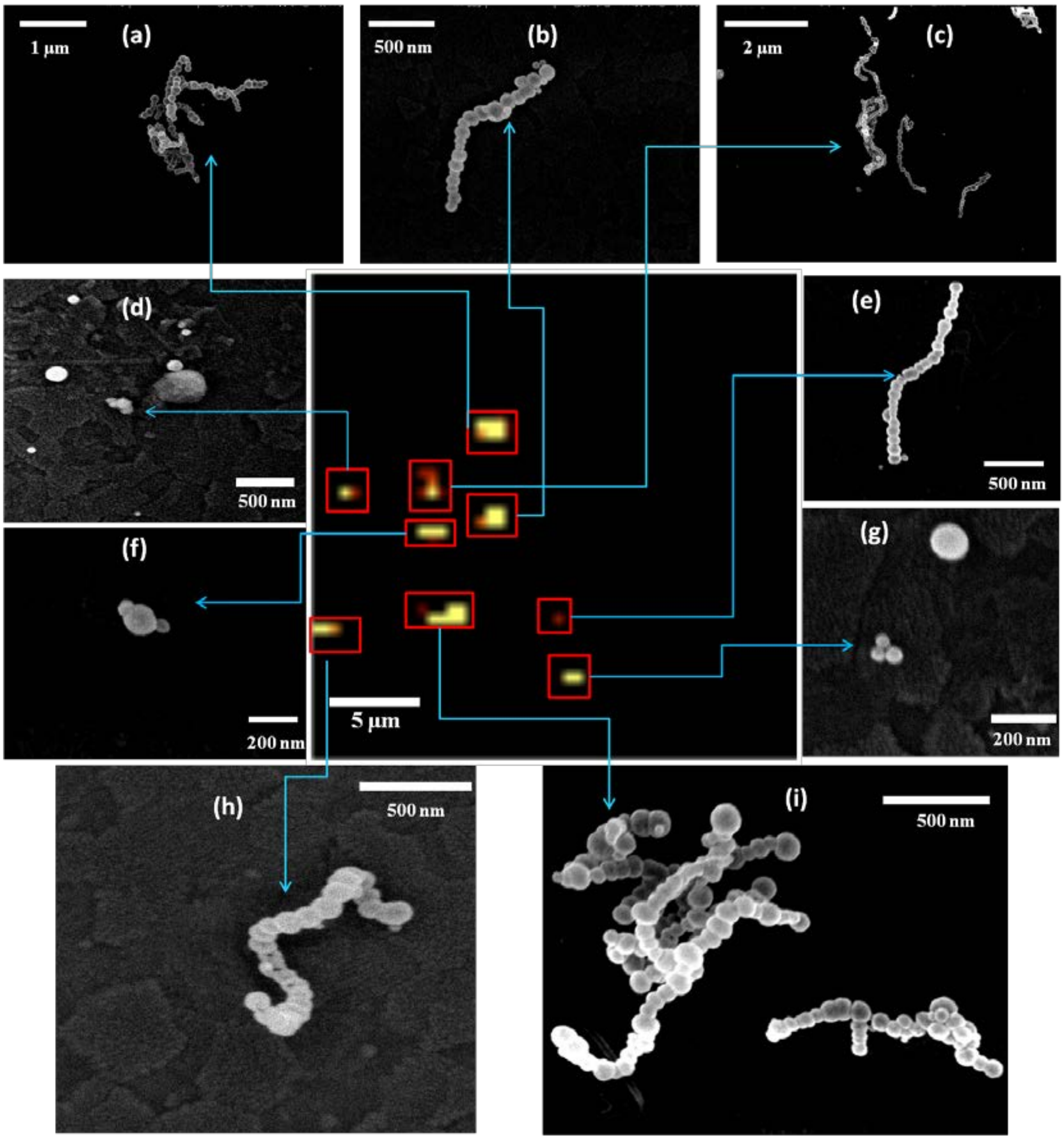

Figure 49. Illustration of all the visible spots in the mapping result for MG using 633 nm excitation. In panel (d) it appears that nanospheres were artificially deposited close to one another in a defect within the ITO glass slide. Therefore, this area was not used for analysis.

In Figure 46 E2, both structures show SERS activity, these are small clusters with some parts bent or with intra-worm contacts which create additional “hot spots”. The single chain structure illustrated in E3 gave the lowest signal among the four structures. The main contribution to the recorded signal for this structure is circled and contains two small gold nanospheres connected to the side of the main nanoworm creating two trimer type structural motifs within the lager nanoworm structure.

When the laser excitation was changed to 785 nm, Malachite green was no longer in resonance. Figure 50C shows a solution MG SERS spectrum using 785 nm excitation. As described previously, the same peak was monitored to create the SERS map. Some nanostructures correlated to the mapping spots are illustrated in Figure 50E. The structures of bright spots all show inter/intra nanoworm interactions or consist of additional individual HGNs positioned on the flanks of the nanoworms. The intensity of the monitored peak for each structure was extracted using the same previously described method used for the 633 nm mapping (Figure 51). E1 and E4 are small clusters with inter/intra worm interactions which are expected to produce “hot spots” as previously discussed. Figure 50 E3 shows the same side attached nanospheres as seen in Figure 46 E3. There are two different types of structures shown in E2 which generate different SERS intensity. The left hand nanoworm structure gives much higher SERS intensity than the right hand chain structure which can be clearly seen from the SERS map and Figure 51. The full SERS spectra extracted from the highest intensity pixel of the two structures and normalized to the same scale are shown in Figure 52. The cluster like structure gives nearly all the characteristic Raman peaks of Malachite green; however, these characteristic peaks are obscured by the background in the spectrum from the single chain structure, except the monitored peak at 400 cm^{-1}. This clearly demonstrates the additional enhancement achievable within a structure which contains inter particle gaps compared to a simpler one dimensional linear chain consisting of fused particles. In addition, the spectrum differences between Figure 52 and Figure 50 are mainly due to the changes of medium (from the solution to air) and instrumentation. All the visible spots in the SERS map (Figure 50D) were correlated with their corresponding structures and are shown in Figure 53, j and k should be high SERS-active structures based on the previous discussion. However, some parts of these structures are over aggregated which physically reduced the collectable SERS signal. Importantly, none of them were due to individual nanospheres.

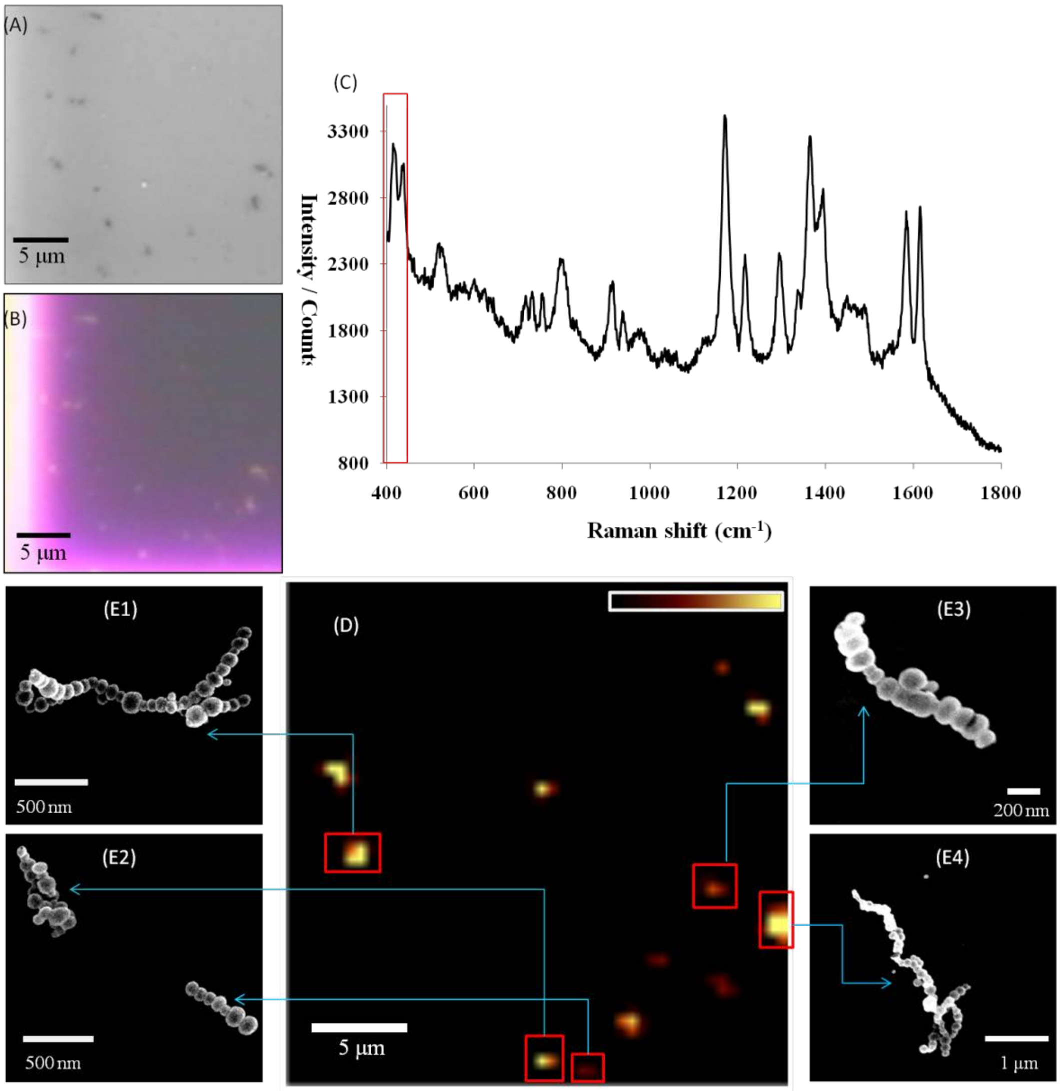

Figure 50. Correlation of a SERS map with SEM images. Malachite green was used as a non-resonant reporter molecule for 785 nm excitation. (A) bright-field image of the mapping area; (B) dark-field image of the exact same area; (C) solution SERS spectrum of MG using 785 nm excitation. The marked peak was monitored in the SERS mapping; (D) a SERS mapping of MG using 785 nm excitation; yellow indicated highest SERS intensity. (E) SEM images of correlated nanostructures.

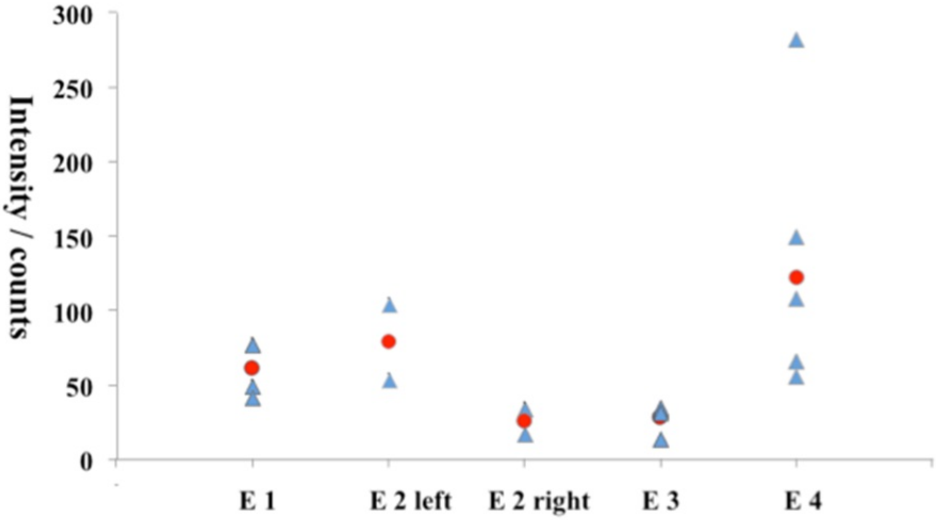

Figure 51. SERS intensity comparison of different nanostructures in Figure 50. The intensity values of the monitored peak were extracted from every relevant pixel. A red circle represents the average value of each nanostructure, and a blue triangle represents the peak intensity from the nanostructure at an individual pixel.

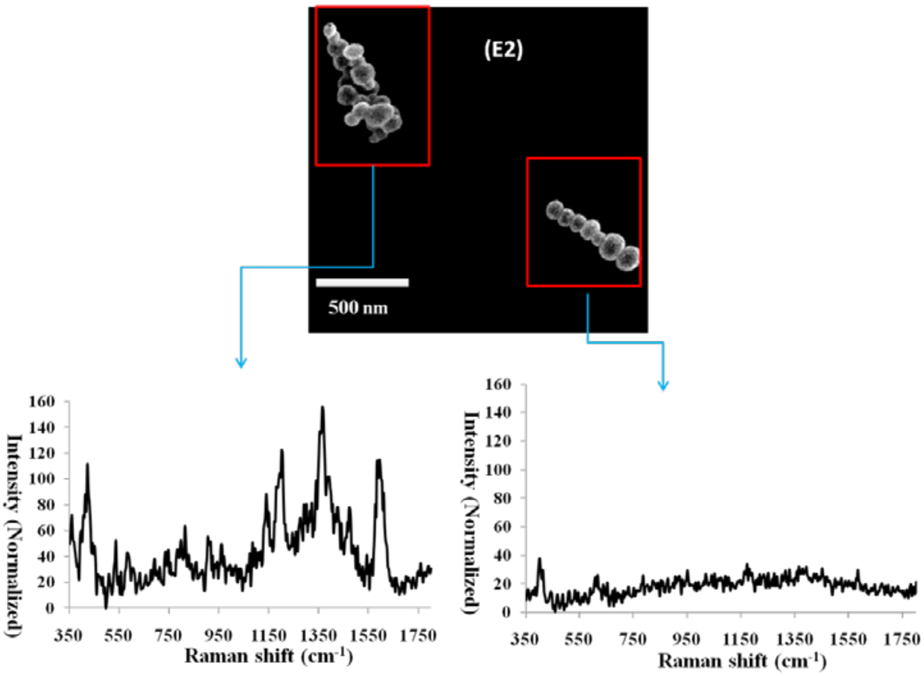

Figure 52. Raman spectra extracted from the highest intensity pixel of the correlated structures. They were both normalized to a same intensity scale.

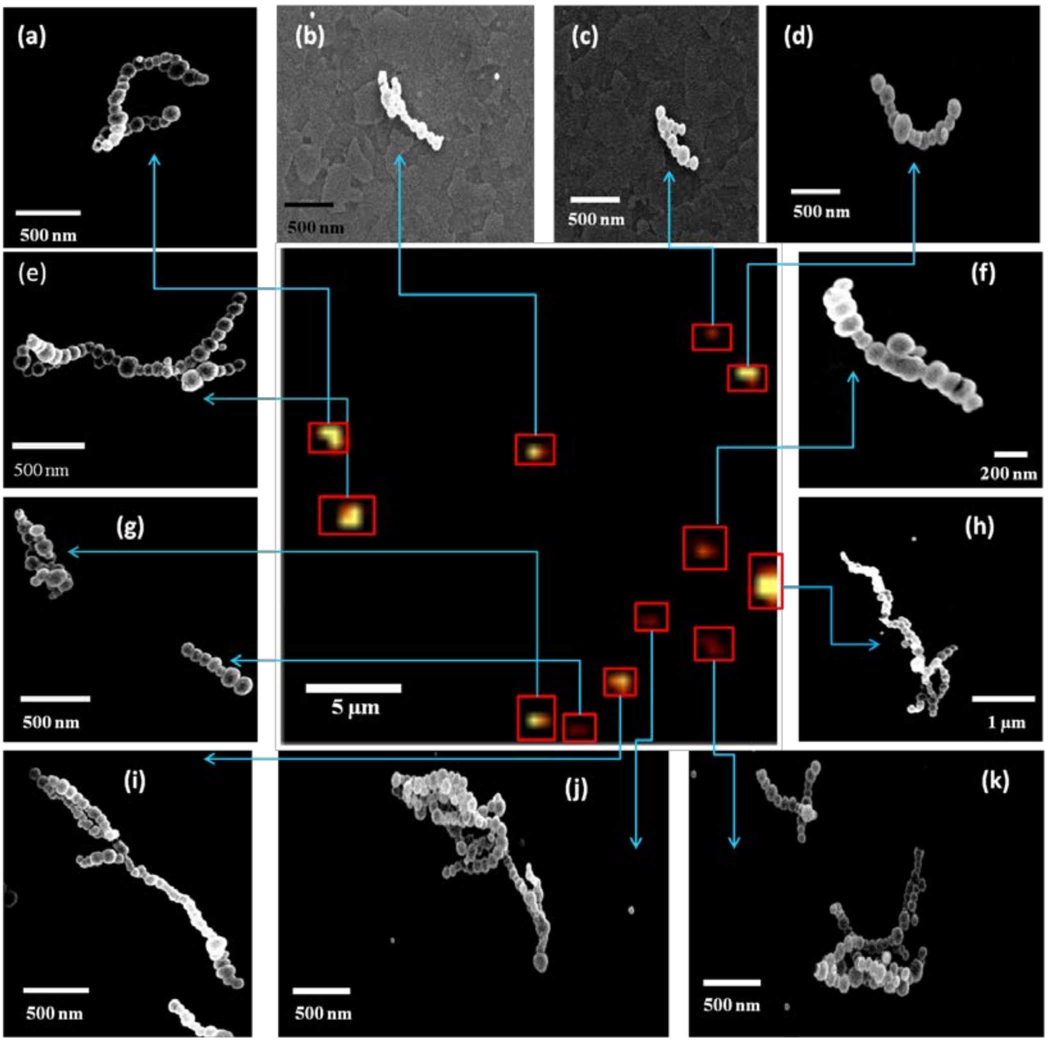

Figure 53. Illustration of all the visible spots in the mapping result for MG using 785 nm excitation.

These findings were additionally confirmed with correlated SERS and SEM analysis using two alternative analytes; 4-mercaptobenzoic acid (Figure 54) and NIR-797 isothiocyanate (Figure 55) which were also mapped using 785 nm excitation. All the highest intensity bright spots in the resultant SERS maps were observed to come from inter/intra worm clusters which is in agreement with the previous experiments using MG.

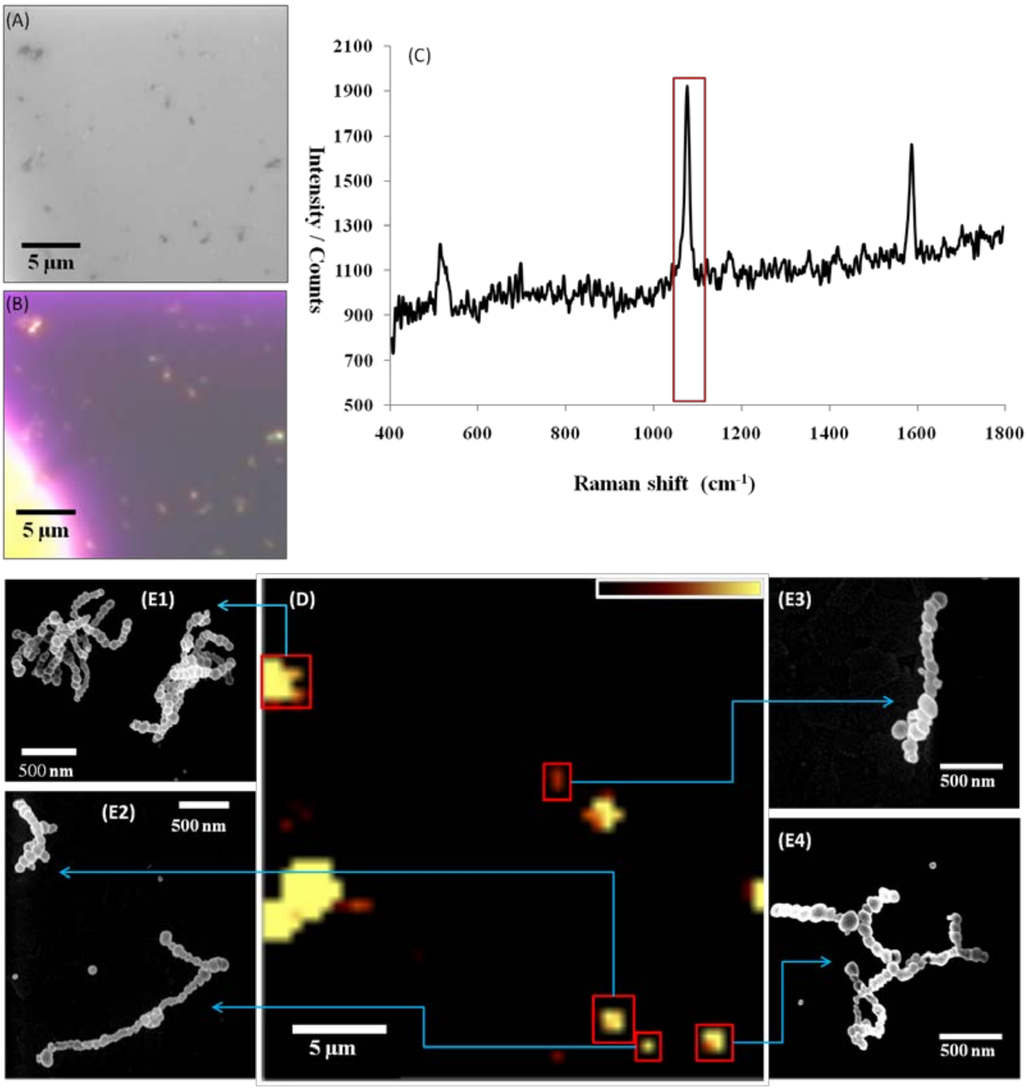

Figure 54. Correlation of a SERS map with SEM images. 4-mercaptobenzoic acid (MBA) was used as a reporter molecule for 785 nm excitation. (A) bright-field image of the mapping area; (B) dark-field image of the exact same area; (C) solution SERS spectrum of MBA using 785 nm excitation. The marked peak was monitored in the SERS mapping; (D) SERS mapping of MBA using 785 nm excitation; yellow indicates highest SERS intensity. (E) SEM images of correlated nanostructures.

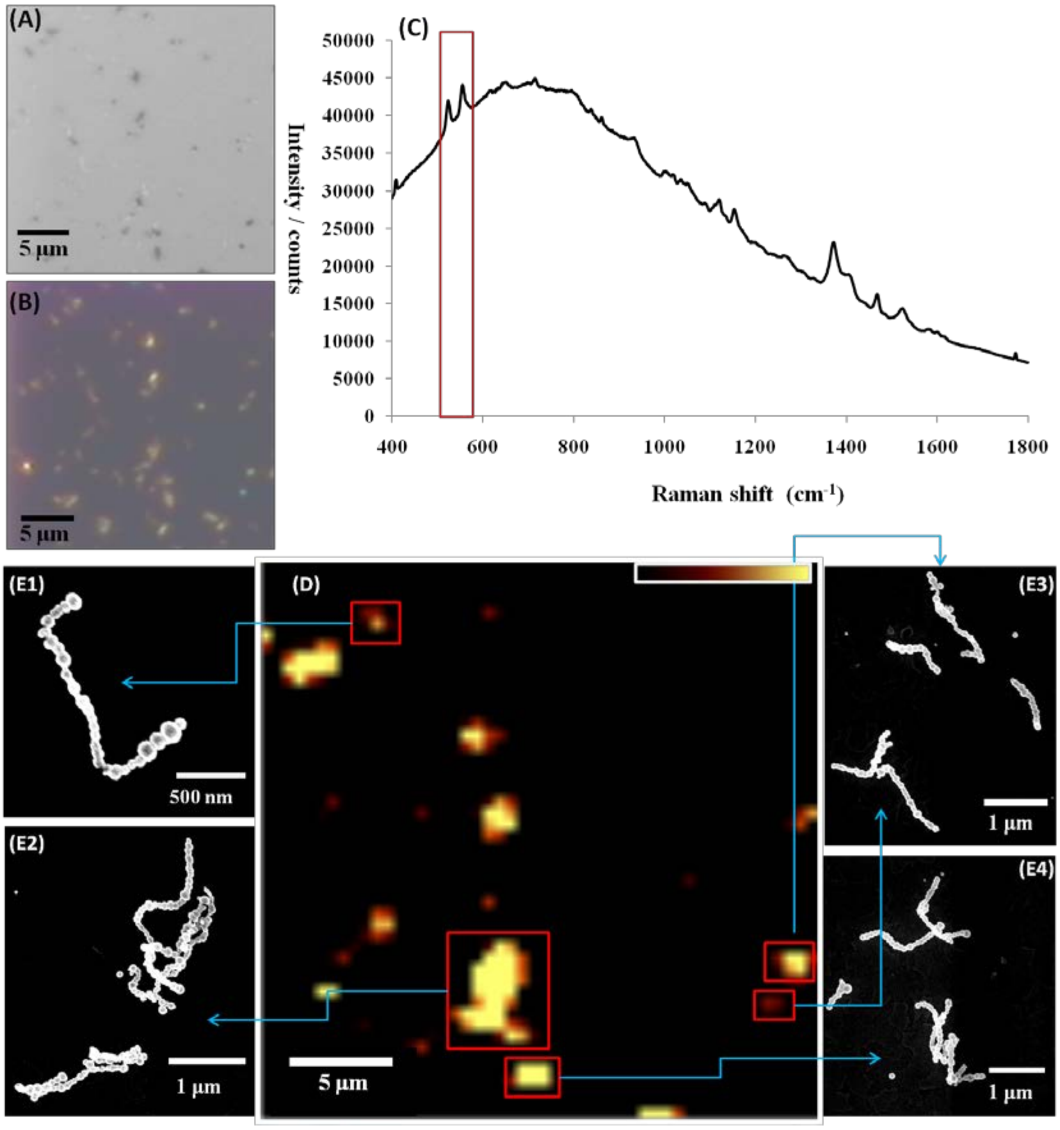

Figure 55. Correlation of a SERS map with SEM images. NIR-797 isothiocyanate was used as a reporter molecule for 785 nm excitation. (A) bright-field image of the mapping area; (B) dark-field image of the exact same area; (C) solution SERS spectrum of NIR-797 using 785 nm excitation. The marked peak was monitored in the SERS mapping; (D) SERS mapping of NIR-797 using 785 nm excitation; yellow indicates highest SERS intensity. (E) SEM images of correlated nanostructures.

Due to the sharper spectral features obtainable using SERS, there is a greater potential for multiplexing compared to fluorescence.[79,145] In order to test the multiplexing ability with nanoworms, a highly concentrated (1 µM final concentration) 4-mercaptobenzoic acid (MBA) and Malachite green (MG) mixture was added to the nanoworm solution, ensuring that the nanoworms were fully coated before deposition on the ITO glass slide. Figure 56 shows maps with SERS spectra extracted from selected regions. Nearly all bright spots showing MG (blue) activity also contained MBA (pink) except one area near the top edge. Figure 56c shows the SERS spectrum extracted from this area and none of the MBA peaks could be observed. Considering the concentrations of both analytes are quite high (around 1 μM final concentration), this shouldn't be counted as a sign of single molecule detection.[146] The most probable reason is that the Raman cross-section of MG is significantly higher than MBA.[19] Although both analytes were in high concentration and the solution aged for a long time, the peaks of MG will be dominant.

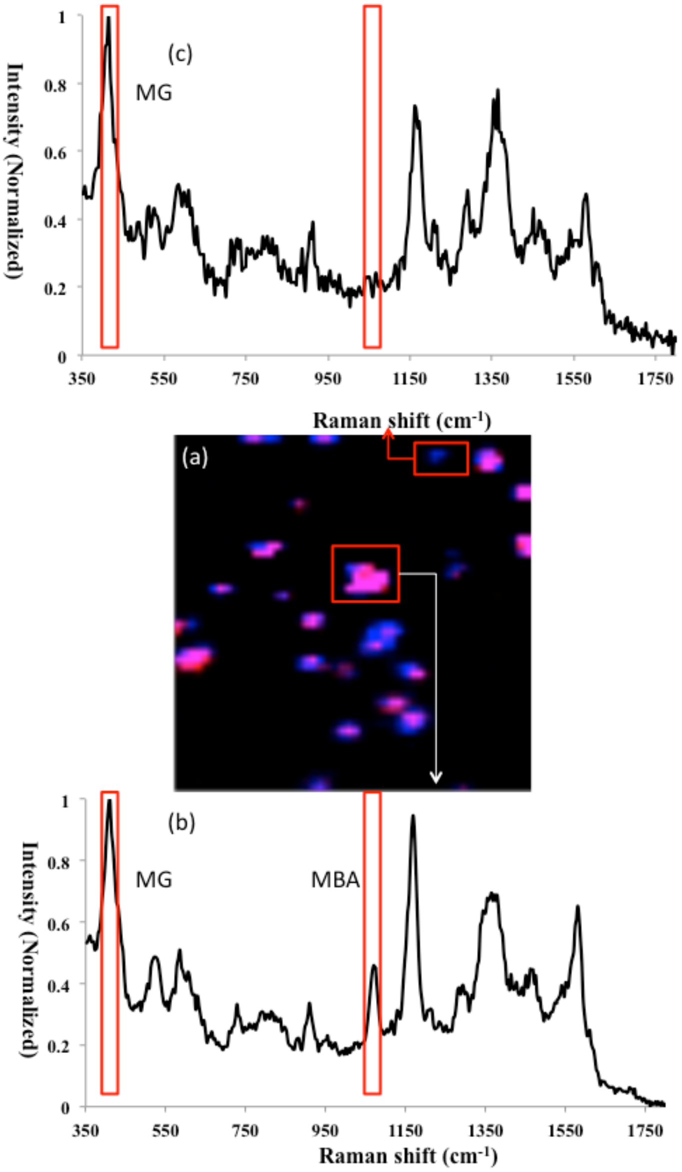

Figure 56. Illustration of the multiplexing property of nanoworms. (a) mapping results of MG (blue) and MBA (pink) mixture using 785 nm excitation; (b), (c) Raman spectra of the marked areas. The marked peaks were monitored.

4.3.4. Discussion of high SERS intensity structure

The highly SERS-active, “hot spot” structures, are where enhanced electromagnetic fields are generated. The tiny gap (around 1 nm) between two gold or silver nanoparticles is used as the simplest model of a hot spot. From TEM and

SEM analysis of these nanoworms, the single chain structure can be considered as a linear assembly of fused individual hollow gold nanospheres. Recently, Wang *et al.* have done theoretical calculations based on a gold nanochain.[147] They showed field enhancement within the gaps of a gold particle chain would maximize at a particle number larger than two.[147] The single chain naoworm such as the right hand structure in Figure 52 shows that only a weak SERS signal is generated from a chain of fused particles. All the structures correlated to the brightest points in the SERS maps were small clusters with inter/intra worm interactions (i.e. with nanogaps being present). Single fused particle chains which showed enhanced SERS activity were observed to have additional nanospheres attached to the flanks of the main chain. These findings were independent of the excitation wavelength and Raman reporter molecules. However, weak SERS signals were observed from single chains which were not as intense as the cluster like structures. The simplest example of a 3D array which contains nanogaps is a trimer as shown in Figure 46 E1 and E4. Undoubtedly, the inter/intra worm cluster structures are also in this 3D array category and contain nanogaps between the worms or between a worm and additional HGNs (i.e. Figure 50 E3). Additionally, bent or distorted structures (Figure 49h) can also be classified as approaching a more complex 3D array where constituent building blocks spatially separated within the linear nanoworm chain end up creating nanogaps within the structure. There are two probable reasons for the observed results. Firstly, the three dimensional array creates enhanced electromagnetic fields due to additional coupling as a result of the nanoworm geometry. Secondly, the chain structures are produced during the synthesis unlike salt induced aggregation which tends to occur after analyte addition. It is reasonable to assume that the inter-particle gaps are blocked during the synthesis of the nanoworms therefore no analyte molecules will be present at the interstices, as parts of the nanoworms are also seen to be tube-like as the inter-particle gap between two hollow nanospheres becomes depleted.

Nanoparticle aggregates work well for SERS because there is a small gap between particles, but contain no direct metal-metal contact in general. In this case, all the hollow gold structures in the chain are fused. This means that at the junctions of the particles, there may be small hot spots, but this isn't nearly as strong as particle-particle junctions in aggregates. The enhancement in this case is coming from worm-worm interactions where there are junctions without metal-metal contact. In other words, a single nanoworm has a structure which results in a SERS signal strength between that of an isolated nanoparticle and a nanoparticle aggregate. However, the interaction between several nanoworms starts to create junctions similar to those found in an aggregate.

In addition, from dark-field images of each correlation, all the bright spots in the SERS maps are yellow/orange which means their scattering wavelengths are less than 650 nm (red light).[142] Although the LSPR of a nanostructure shows a little deviation of its maximum scattering wavelength, the structures present on ITO glass are all off resonance with the 785 nm excitation medium.[148] Recently, Van Duyne and co-workers discovered that enhancement factors for SERS were not highly correlated to the localised surface plasmon resonance wavelength of metallic nanoparticles, but they were crucially dependent on the size of the interparticle gap through finite element calculations.[84] Hence, in our case, the major contribution for bright spots in the 785 nm SERS maps were the three dimensional array structures containing decreased interparticle gaps and therefore structural “hot spots”, instead of the localised surface plasmon resonance of the nanostructures.

Recently, there is a debate about the correlation of nanostructures and SERS activities utilizing electron microscopies. It is common to find a large SERS intensity variation for the extremely similar nanostructures.[84,131,132,149] The reasons are still not clear. However, the development of super-resolution SERS may provide an answer in the near future.[150-152]

4.3.5. Enhancing the SERS Properties of Nanoworms by Matrix Formation

As mentioned above, the formed gold nanoworms have a three dimensional array structure and demonstrate outstanding individual SERS properties. In this section, gold nanoworms were immobilised on a commercial membrane surface by simple filtration to produce a simple and cost-effective porous SERS surface for use and quantitative analytical procedures.

Background signals from the substrate can have a significant effect on the application of such SERS substrates. The filter membrane used in this study was made of polyvinylidene fluoride and showed negligible Raman scattering after deposition of the gold nanoworms (Figure 57). As shown in Figure 58b, the immobilisation of several high-density layers of gold nanoworms on the membrane produces a black colouration despite the original nanoworm solution being green. The manufacturer specified pore size of the membrane was ~450 nm, which allowed some individual particles and small nanoworms to pass through. Therefore, although the native nanoworm solution has quite a broad plasmon peak (Figure 59), only a red colouration was seen under dark-field illumination of the nanoworms on the membrane (Figure 60) which indicates that the localized surface plasmon resonance of the deposited nanoworms was around 650 nm.[153] From the SEM images (Figure 58d) it can be seen that the porous membrane is fully coated with gold nanoworms. This nanoworm matrix provides an excellent substrate for SERS as it creates additional hot spots among the already SERS-active individual nanoworms due to the inter-worm electromagnetic couplings.

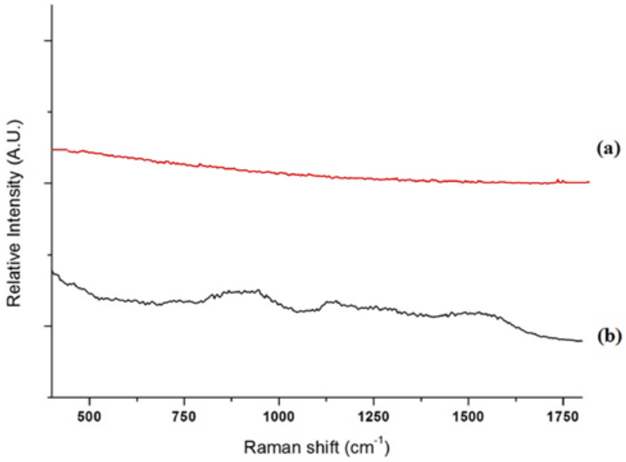

Figure 57. Average Raman backgrounds of a blank membrane (a) and a nanoworm membrane (b). The spectra are the averaged of the spectra obtained over a whole SERS mapping area containing 625 individual spectra. They have been offset for clarity.

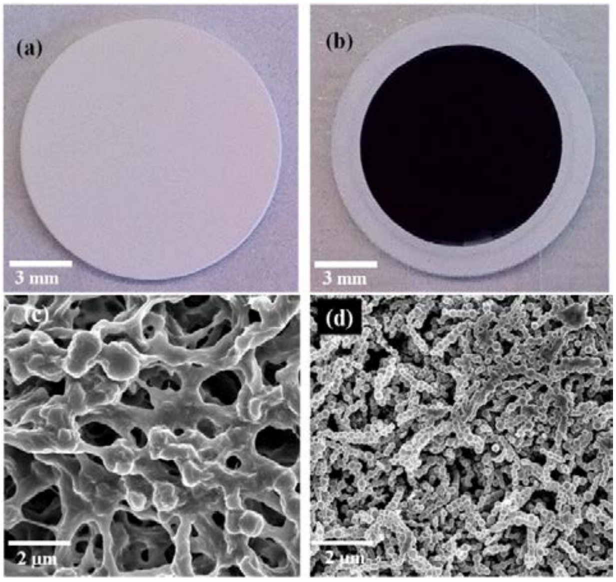

Figure 58. Characterisation of a nanoworm membrane. (a) Image of membrane; (b) image of gold nanoworms deposited on membrane; (c) SEM image of membrane; (d) SEM image of gold nanoworms deposited on membrane under the same magnification.

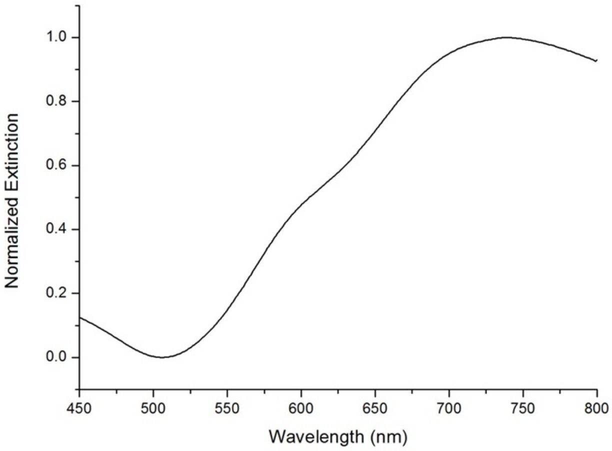

Figure 59. Extinction spectrum of the nanoworm solution with localized surface plasmon resonance around 745 nm.

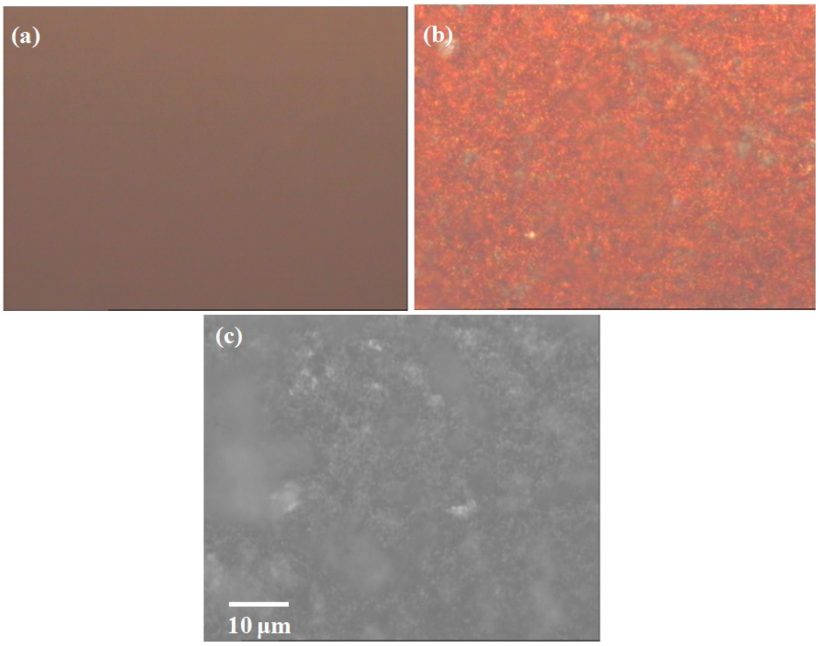

Figure 60. (a) Dark-field image of an empty membrane; (b) Dark-field image of a nanoworm coated membrane; (c) Bright-field image of a nanoworm coated membrane.

Due to the variable height of the nanoworm matrix on the membrane, it is difficult to keep the sample in focus during large scale (>25 μm) SERS mapping. (Figure 60 C) Therefore, the average spectrum was extracted from a map with dimensions of 25×25 μm. To demonstrate the different SERS properties between the nanoworm membranes and nanoworms in suspension, 5 mL of nanoworm solution with a final concentration of 100 nM 4-mercaptobenzoic acid (MBA) was prepared. From Figure 61, it is seen that the nanoworm solution does not give any MBA signals when the spectrum was accumulated for 10 seconds. However, when the pre-functionalised nanoworm solution was immobilized onto a membrane, strong characteristic MBA peaks at 1586 and 1076 cm^{-1}, which are assigned to the ν_{8a} and ν_{12} aromatic ring vibrations,[154] were observed . The upper spectrum in Figure 61 was the average across the whole mapped area as extracted by the instrumentation software. The highlighted peak was monitored during all subsequent SERS mapping experiments.

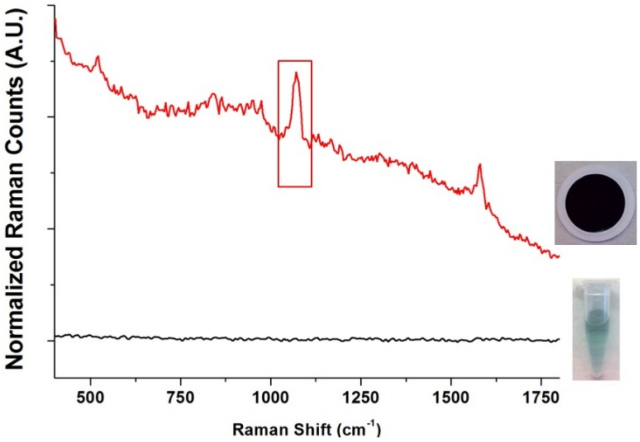

Figure 61. SERS comparison between a nanoworm membrane and a nanoworm solution at an excitation wavelength of 785 nm. 100 nM 4-mercaptobenzoic acid was used as a Raman reporter in both measurements. The highlighted peak was monitored during subsequent SERS mapping. The spectra were normalized to a silicon standard under the experimental conditions.

The optical properties of individual gold nanoworms have been previously investigated. However, the interactions between nanoworms, which could result in improved SERS properties are yet to be suitably probed. Therefore, to separate the individual from the collective enhancement, a comparison between these two systems was carried out. Nanoworms pre-functionalized with MBA were immobilized on a membrane and ITO coated glass respectively. The density of nanoworms on the ITO glass was such that individual nanoworms could be interrogated (Figure 62) unlike in the case of the membranes where a multilayered matrix was formed. Three 25 × 25 μm SERS maps of different regions on each substrate were performed under the same experimental conditions. Typical SERS maps of the nanoworm membrane and nanoworm ITO glass are shown in Figure 63 a and b. The intensity of the monitored peak was extracted from the maps. A base value was set at the background intensity/noise level; only values 3 times larger than the base number around the structures were treated as active pixels. It is important to note that for the nanoworm on ITO glass substrates, only the active pixels were selected to calculate the average intensity of the monitored peak since we wish to compare only individual and cooperative effects rather than the signal across the whole area. Although the membrane maps encountered a problem with focusing on the rough surface (Figure 60 C), the peak intensities extracted from the average spectra are still seven times higher than the intensities extracted from active pixels on the ITO glass substrate. In addition, when the peak intensity was extracted only from the brightest spots (4 times larger than the cut-off number) in the nanoworm membrane maps, they are nearly ten times higher than the signal from individual nanoworms on ITO glass. Importantly, based on the standard deviations of the intensity of the monitored peak shown on Figure 63c, the signal homogeneity from the membranes is much better than the active pixels extracted from ITO glass substrates. The reason for the observed increase is due to the formation of a densely packed nanoworm matrix on the membrane, which creates additional electromagnetic couplings between individual nanoworms resulting in a large enhancement of the Raman signals. However, for the ITO glass, the major enhancement originates from the geometries of individual nanoworms which is weaker.[107]

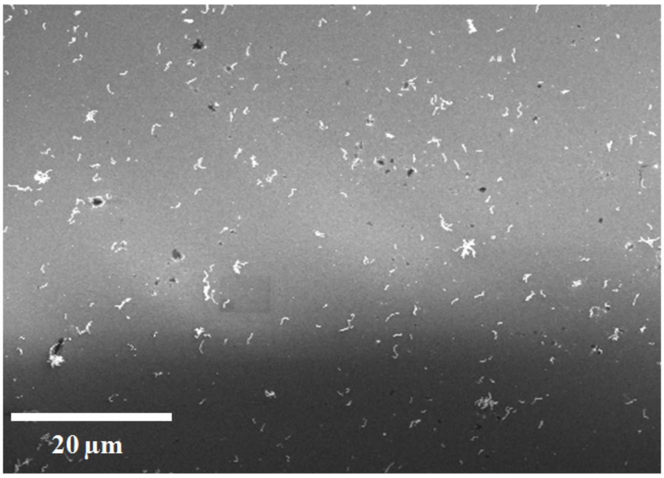

Figure 62. Illustration of the density of nanoworms on an ITO glass substrate.

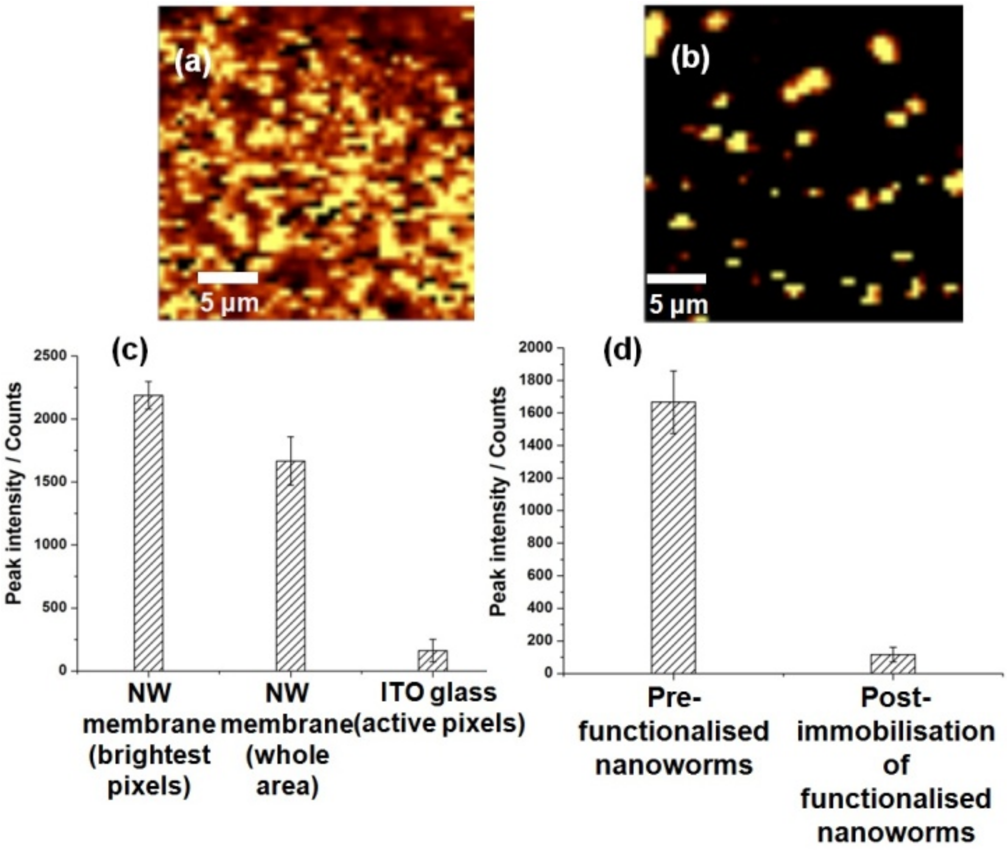

Figure 63. (a) SERS map of a nanoworm membrane with dimensions of 25×25 μm at the excitation wavelength of 785 nm with 0.3 s integration time and ~750 μw laser power; (b) SERS map of individual nanoworms deposited on ITO glass under the same experimental conditions; (c) comparison of different intensities of the monitored peak. Three SERS maps of different areas of the same substrate were carried out; (d) Comparison of intensities of the monitored peak between different methods.

The order of analyte addition to the nanoworms was also investigated. The first method involved gold nanoworms being incubated with 1 µM (final concentration) of MBA in solution before being immobilised on the membrane. The second method was to immerse a non-functionalised nanoworm coated membrane into the MBA solution for the same amount of time as used in method 1 which is more realistic for practical applications. From Figure 63d, a large difference in the recorded SERS intensity was observed. One possibility for this is that in method one, the full nanoworm can become coated with analyte molecules. Any analyte-induced aggregation in solution does not need to be considered since the solution will be aggregated upon immobilization on the membrane surface by filtration. Upon nanoworm immobilisation, additional inter-nanoworm interactions will occur, these sites will contain more analyte molecules which will benefit from the increased electromagnetic field. However, for method two, pre-immobilization of the nanoworms on the membrane leads to densely packed nanoworm layers whose inter-nanoworm interaction sites are physically blocked, making the diffusion of analyte molecules into them very difficult. A second possibility is due to the absorption kinetics of MBA, when in solution both analyte molecules and nanoworms will have significant motional freedom, unlike when the nanoworms are fixed on a membrane. Therefore, although the final concentration of MBA and reaction time were the same for both methods, it is reasonable to assume different final MBA coverage.

4.4. Conclusions

Gold nanoworms have been synthesized by the addition of an external magnetic field during the synthesis of hollow Au nanospheres. Their compositions as well as their SERS properties, including their multiplexing ability have been investigated. The structures of the nanoworms were correlated with SERS maps with the assistance of TEM grids.

From TEM and EELS, nanoworms with fused hollow nanosphere segments but without major tube formation were confirmed and the shell was found to consist of gold with no traces of cobalt. The SERS properties were studied with three different reporter molecules: Malachite green, NIR-797 isothiocyanate and 4-mercaptobenzoic acid and two different laser excitations (632.8 and 785 nm). From the Raman maps and correlated SEM images, the SERS activity was found to be in the order of: single nanospheres < fused nanosphere chains < inter/intra nanoworm interactions. This order is a direct result of the interacting nanoworm structures possessing nanogaps unlike the case of a single fused nanoworm chain where no inter particle gaps exist. The localised surface plasmon resonance of the nanostructure was found to have a minimal effect. This study demonstrates the morphological intermediate case, between single nanoparticles and aggregates with nanogaps, of a linear chain of fused nanoparticles. The SERS response is also found to be intermediate between single nanoparticles and aggregates with nanogaps present.

In addition, the use of gold nanoworms as the basic SERS enhancing unit, coupled with assembly on a membrane by simple filtration to produce a large SERS response was also demonstrated. Gold nanoworms immobilized on the membrane provided significant enhancements of the SERS signal because of the additional electromagnetic couplings created between nanoworms. This study offers a new way to construct simple and cost-effective porous SERS substrates.

Chapter 5. Tracking Bisphosphonates through a 20 mm Thick Porcine Tissue by Using Surface-Enhanced Spatially Offset Raman Spectroscopy

5.1. Introduction

One in eight women is at risk of being diagnosed with breast cancer in their lifetime according to Cancer Research UK and at least 25% of patients with breast cancer develop skeletal metastases resulting in the site of disease generating the greatest morbidity.[155] Skeletal complications include hypercalcaemia, pathological fracture, bone pain requiring radiotherapy, and spinal cord or nerve root compression.[155] Randomised trials in advanced breast cancer have shown that one of these major events occurs, on average, every 3–4 months.[156,157] The average life expectancy from diagnosis of bone metastases is 2 years, with only up to 20% of patients surviving 5 years.[155] There is great clinical need for treatment to reduce skeletal complications and to improve the quality of life in these individuals.

Bisphosphonates (BPs) are an important class of drugs used in the treatment of osteoporosis and other conditions involving bone fragility.[158] Tumour cells in the bone marrow cavity secrete a variety of paracrine factors that stimulate bone formation and the stimulation of osteoclast function is of key importance.[155] This results in osteolysis, which is typically associated with disruption of the normal coupling signals that control the relative levels of osteoblast and osteoclast function. It is in this situation that bisphosphonates are able to offer their therapeutic potential in metastatic disease.[155] To monitor the progress of the disease and the effectiveness of therapy, it is vital to identify the bisphosphonate localization in treatments. Recently, a number of approaches have exploited the specificity of bisphosphonates to create bone imaging reagents[159] such as NIR-bisphosphonate dyes[160] and ^{99m}Tc[161]labeled bisphosphonates. Their success as therapeutic drugs and bone imaging agents relies on their exceptional selectivity and strong affinity for solid-phase calcium hydroxyapatite which is predominantly found in bones.[162] Binding is thought to occur through optimised chelation of the bisphosphonic moiety with superficial Ca^{2+} ions on the bone surface.[163] Recently, Hernandez-Santana *et al.* isolated calcium phosphate crystals from complex biological fluids using bisphosphonate-modified superparamagnetic beads.[163] However, this work focused only on the isolation of the calcium phosphate crystals and lack of subsequent detection limited its further applications.

Surface enhanced Raman scattering (SERS) is a molecular detection technique that can be tuned to the near infrared (NIR) region, which is of significant biological importance as this region provides a clear spectral window for both therapeutic and imaging applications in tissue.[51,97] However, even with an optimized set-up, the depth of penetration (less than 10 mm) remains an obstacle for most *in vivo* SERS applications.[3] An alternative approach is to redesign the instrument and maximize the penetration depth that resulted in the development of spatially offset Raman spectroscopy (SORS). (Figure 64)[164,165] Importantly, the collected signals from the setup shown in Figure 64 contain different relative Raman contributions from the surface and subsurface layers. This is the key effect on which this technique is based. As the collection point is moved away from the probe launch point, the contribution of the spectrum from the top layer diminishes much faster than that from deeper layers.[164] As shown in Figure 64 Raman photons that are generated deeper within the sample are more likely to drift laterally before they are emitted from the sample surface. By collecting a set of spectra at different distances from the launch point and processing them using a multivariate data analysis technique, to the pure Raman spectra of the individual layers can be extracted approximately. A SORS measurement will make at least two Raman measurements; one at the surface and one at an offset position of typically a few millimeters away.[164] This method relies on moving the area of collection of the scattered light away from the laser illuminated zone and allows highly accurate chemical analysis of objects beneath obscuring surfaces, such as tissue, coatings and bottles.[156] Preliminary results from our group in collaboration with Stone and Matousek[166,167] allowed a recognizable signal from SERS active NPs at a depth of around 50 mm in tissues to be obtained.

Subsequent work by Van Duyne on the subcutaneous detection of glucose also shows the great promise of SORS in biological applications.[157,168] In this case, silver film over nanosphere (AgFON) surfaces were functionalized with a mixed self-assembled monolayer (SAM) and implanted subcutaneously in rats. The glucose concentration was monitored in the interstitial fluid of six separate rats using SORS. This approach allows the direct detection of glucose with high accuracy especially in the low glucose concentration range as well as over a long period of time with only a one time calibration.[157,168]

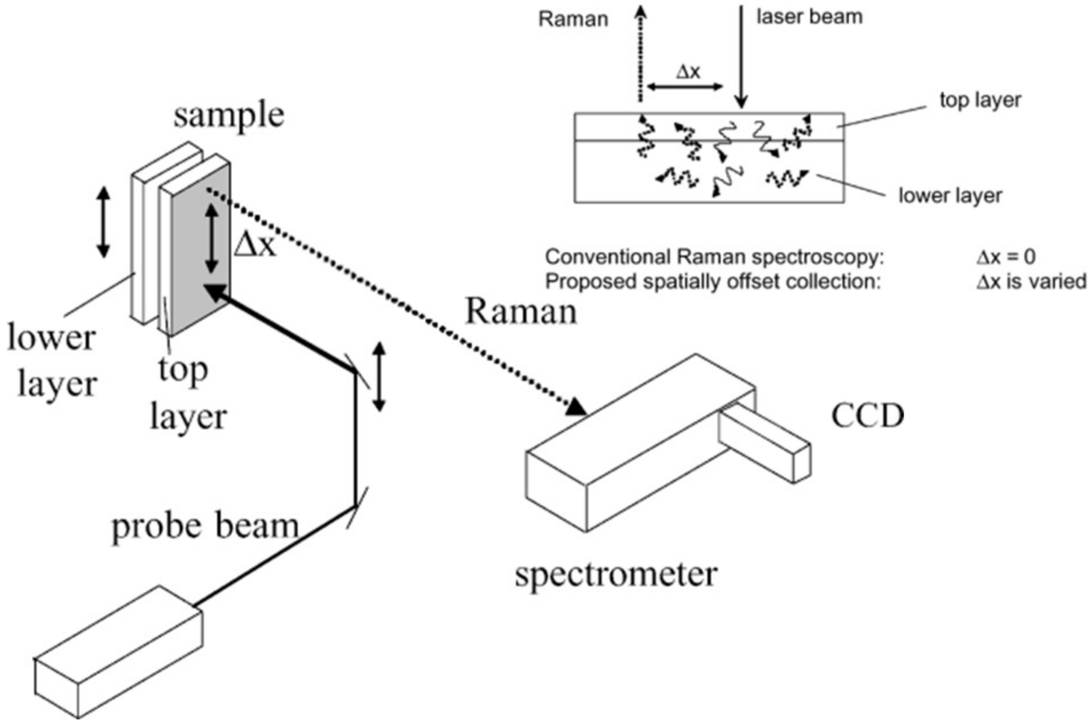

Figure 64. Schematic diagram of the SORS setup. Reproduced from Ref.[164].

A SERS nanotag is produced by placing a label molecule on the surface of an Ag or Au nanoparticle, thereby creating a known SERS spectrum of that molecule. Once this basic structure is in place, a biomolecule recognition unit, such as an antibody, can be added.[169] Mulvaney[170] and Doering[171] firstly reported Silica encapsulated SERS tags which are being commercialized by Cabot as Nanoplex biotags.[172] These biotags are composed of one or more SERS active metal nanoparticles (typically Au, 50–90 nm in diameter), a submonolayer of a reporter molecule adsorbed to the metal surface, and a silica coating, typically 20–50 nm thick.[169] Figure 65 shows a typical TEM image obtained from a set of biotags, showing both the Au core and the silica coating of individual tags.

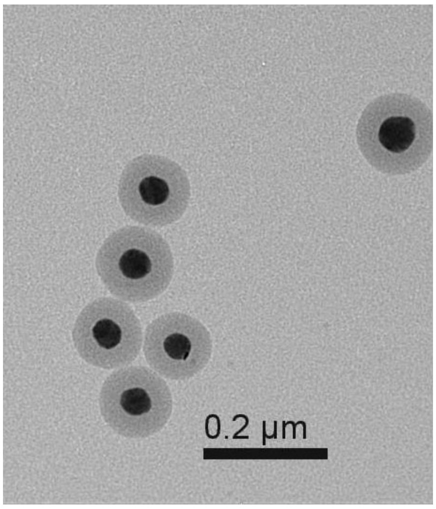

Figure 65 TEM image of typical silica encapsulated SERS nanotags.[169]

Irradiation of these tags with lasers yields the SERS spectrum of the reporter. To make a different tag, one simply employs a different reporter molecule. Since SERS features are narrow compared to fluorescence, and since there is a large spectral window in molecular vibrational spectra, it is possible to create many distinct and simultaneously quantifiable tags.[169] Figure 66 presents Raman spectra from six different Nanoplex biotags, showing the variation in the spectra.[169] Silica encapsulation provides an isolated layer between the Au surface and external solution components. This prevents desorption of the Raman label molecule, adsorption of other potentially interfering. In addition, the silanol surface can be readily functionalized with bioreactive moieties such as thiols or amines using methods similar to those reported by Schiestel *et al.*.[173] Standard cross-linking reagents can then be used to attach proteins or oligonucleotides. For example, one of the preferred routes for attachment of antibodies is to use the heterobifunctional crosslinker sulfosuccinimidyl-4-(N-maleimidomethyl)cyclohexane-1-carboxylate (sulfo-SMCC) to link native amines present on the antibodies to thiol-functionalized tags.[169]

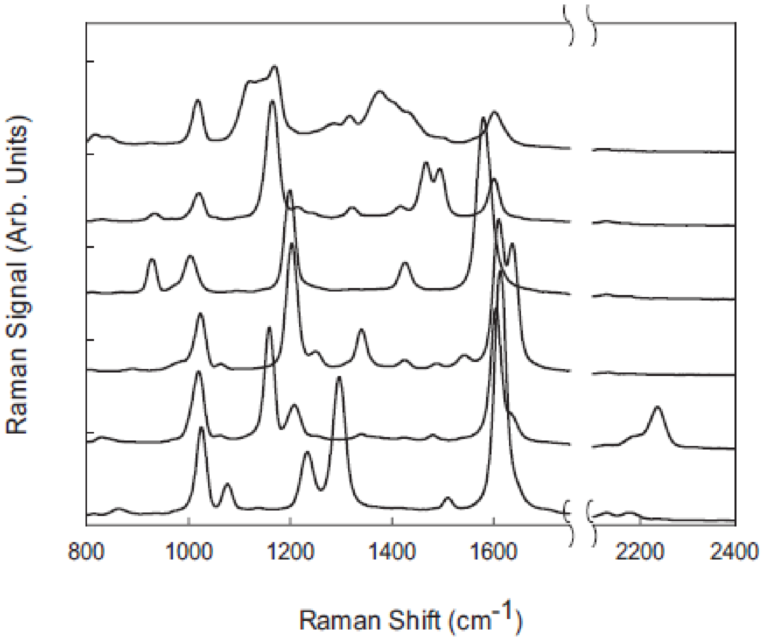

Figure 66 Raman spectra of six different Nanoplex biotags. From top to bottom, the label molecules used were 4-[4-hydroxyphenylazo]pyridine, 4,4′-azopyridine, d_8-4,4′-dipyridyl, bis(4-pyridyl)ethylene, bis(4-pyridyl)acetylene, 4,4′-dipyridyl.[169]

In this work, porcine bones, consisting mainly of calcium hydroxyapatite and bisphosphonate-functionalized SERS nanotags as Raman reporters were used for a simulation study of tracking the bisphosphonate localization through SERS which could be useful both in metastatic breast cancer and bone disease treatments. To demonstrate the *in vivo* application potential, bone fragments pre-incubated with functionalized nanotags were inserted into 20 mm thick specimens of porcine muscle tissue allowing observation of Raman through surface enhanced spatially offset Raman spectroscopy (SESORS). Unlike previous work,[167] a fine distribution of nanotags on the surface of the bone was measured rather than a concentrated droplet injected into the tissue.

5.2. Experimental

5.2.1. Bone conjugation

Porcine bones from a local butcher shop were cut into small pieces with dimensions of around 5×10×10 mm. The bones were sonicated in a slightly basic solution followed by water to remove grease from their surface before further experiments.

Encapsulated SERS active nanoparticles (SERS-440, 20X) produced by Cabot Security Materials Inc. (Mountain View, CA, U.S.A.) were used in this study. Bisphosphonate conjugation was performed according to the technical note accompanying the nanotags. 18.5 µL (5 mg/mL in water) of Neridronate (Sigma) (bisphosphonate) solution was placed in a 0.5 mL microcentifuge tube. 6.5 µL solution of freshly prepared sulfo-SMCC (Thermo Scientific) in water (2mg/mL) was added and gently mixed at room temperature for 60 min. Then, 150 µL of thiol-modified SERS nanotags were added and incubated for 4 hours with gentle shaking at room temperature.

As shown in Figure 67, the amine group in the bisphosphonate was firstly activated by sulfo-SMCC forming the maleimide-activated compound and then it was conjugated with thiol groups on the nanotag surface.

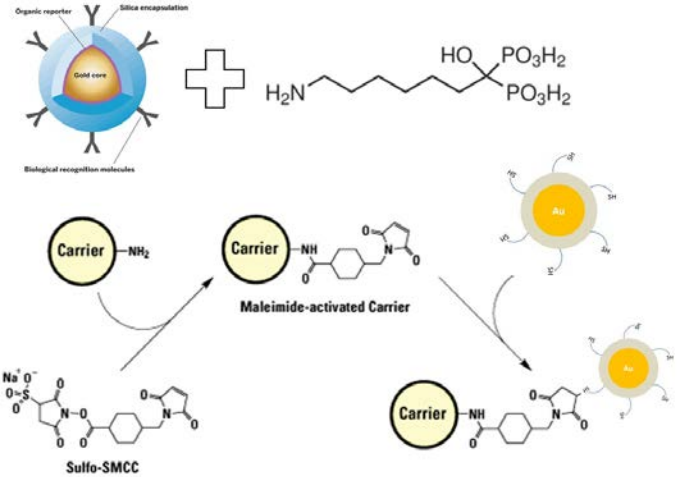

Figure 67 Schematic of functionalization of thiol-modified gold nanotags with Neridronate.

Finally, functionalized nanotags were separate by centrifugation and redispersed in 1 mL water. For the controls, Neridoronate and sulfo-SMCC were replaced with 50 mM borate buffer (pH= 7.2) respectively. Bone fragments were placed in the nanotag solution with gentle shaking overnight and washed with water followed by sonication to remove non-specific binding. Samples were dried under nitrogen before Raman analysis.

5.2.2. Characterization

SERS maps were performed on a WITec alpha300-R equipped with a MSPLan 20×/NA 0.46. A 785 nm diode laser with a power of ~ 750 µW was used as the excitation source. The integration time per point was 0.5 s. The geometry of scanned areas was 50 µm × 50 µm with 50 lines and 50 points per line (2500 spectra per map).

Surface enhanced spatial offset Raman spectra (SESORS) were acquired using the same configuration as outlined in previous papers.[167,174,175] This includes an Innovative Photonics Solutions 830 nm laser as the source which was filtered with two 830 nm laser line filters (Thorlabs), leaving a collimated spot of 4 mm diameter and 219 mW at the sample surface. The transmitted Raman light was collected using a standard 50 mm diameter fused silica lens with a focal length of 60 mm. The scattered light was collimated and passed through a 50 mm diameter holographic notch filter (830 nm, Kaiser Optical Systems, Inc.) to suppress the elastically scattered component of light. The second lens, identical to the first, was then used to image, with magnification 1 : 1, the sample interaction zone onto the front face of a fibre bundle. The laser incident spot was positioned in such a way so that it coincided with the centre of the fibre probe axis projected through the imaging system on the sample. A demonstration of signal obtained through increasing depth was achieved by cutting samples from pork muscle to thicknesses of around 20 mm and mounted in the experimental apparatus.

5.3. Results and Discussion

Commercially available SERS nanotags were functionalized with bisphosphonate (Neridronate), which can provide specific binding to calcium phosphate salts, to provide a SERS specific identification of bisphosphonate localization.

Figure 68a illustrates the functionalisation of encapsulated SERS active thiol-modified nanoparticles through sulfo-SMCC couplings.[176] Bisphosphonate and sulfo-SMCC were replaced with buffer solution in the three different controls to prove that binding of bisphosphonate functionalized nantags to the surface of bones only occurred in positive samples. Bone fragments were placed in the different nanotag solutions mentioned above with gentle shaking overnight and washed with water followed by sonication. Raman spectra of bisphosphonate functionalized nanotag covered bones and blank bones are shown in Figure 68b. The solution SERS spectrum of nanotags is also given as a reference. The bone surface is not completely flat making it difficult to perform Raman maps due to issues with focusing the laser beam onto the rough surface. To minimize this problem, but still gain enough signals, a 20× objective lens was used and the mapping geometry was confined to 50 µm × 50 µm. The peak at around 960 cm^{-1} observed in both samples was due to the phosphate stretch of the bone.[177] This peak was used as an internal reference throughout, thus ensuring the absence of nanotag signal was not because of poor objective focusing.

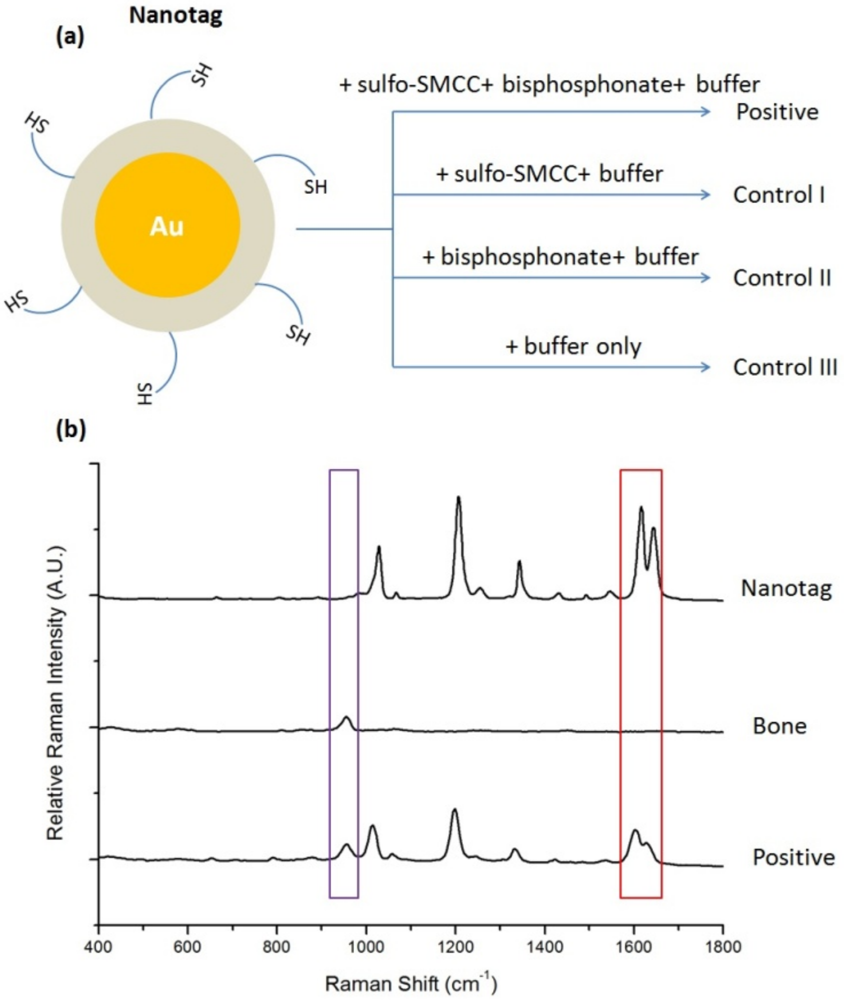

Figure 68. (a) Schematic illustration of the bisphosphonate functionalised nanotags. (b) Raman spectra of nanotag only, bone only and positive samples. The peak at around 960 cm^{-1} due to the phosphate stretch in bone was observed in the positive and bone samples only (highlighted by the purple box) and was used as an internal reference. One of the nanotag characteristic peaks (at around 1600 cm^{-1}) highlighted by the red box was chosen as the monitored peak in the subsequent maps.

False colour SERS maps were constructed using the intensity of the monitored peak of the nanotag (around 1600 cm^{-1}). Three different bone pieces, which were bound to bisphosphonate functionalized nanotags, show very different images compared to the control samples as can be seen in Figure 69. This is due to the chelation of the bisphosphonic moiety with superficial Ca^{2+} ions on the bone surface. The spectra within each pixel of the maps were also checked to ensure that the phosphate stretch from the bone could also be observed, especially for the controls where no nanotag SERS spectrum would be expected, thus ensuring that a signal was being observed from the surface of the bone and the laser was correctly focused on the surface. Despite Figure 69d and e showing some very weak signals because of the non-specific adsorption of a small amount of nanotags, no obvious spots were observed in the control samples. Bone samples were sonicated in water to reduce the non-specific binding, however we assume that nanotags could still be trapped inside the cavities on the bone surface. Nevertheless, a huge discrimination between positive samples and controls was observed. To ensure reproducible results, another two different bone fragments were covered by bisphosphonate functionalized nanotags and the SERS maps were also performed in three different areas of each bone fragment. These SERS maps of positive and control bone samples are shown in Figure 70 and Figure 71. From Figure 70, the nanotag signals were observed in most areas of the maps, however, the control sample maps show almost completely dark images under the same intensity colour scale which was also observed in Figure 69. Therefore, the bisphosphonate functionalised nanotags show strongly specific binding to the bone surface (calcium hydroxyapatite).

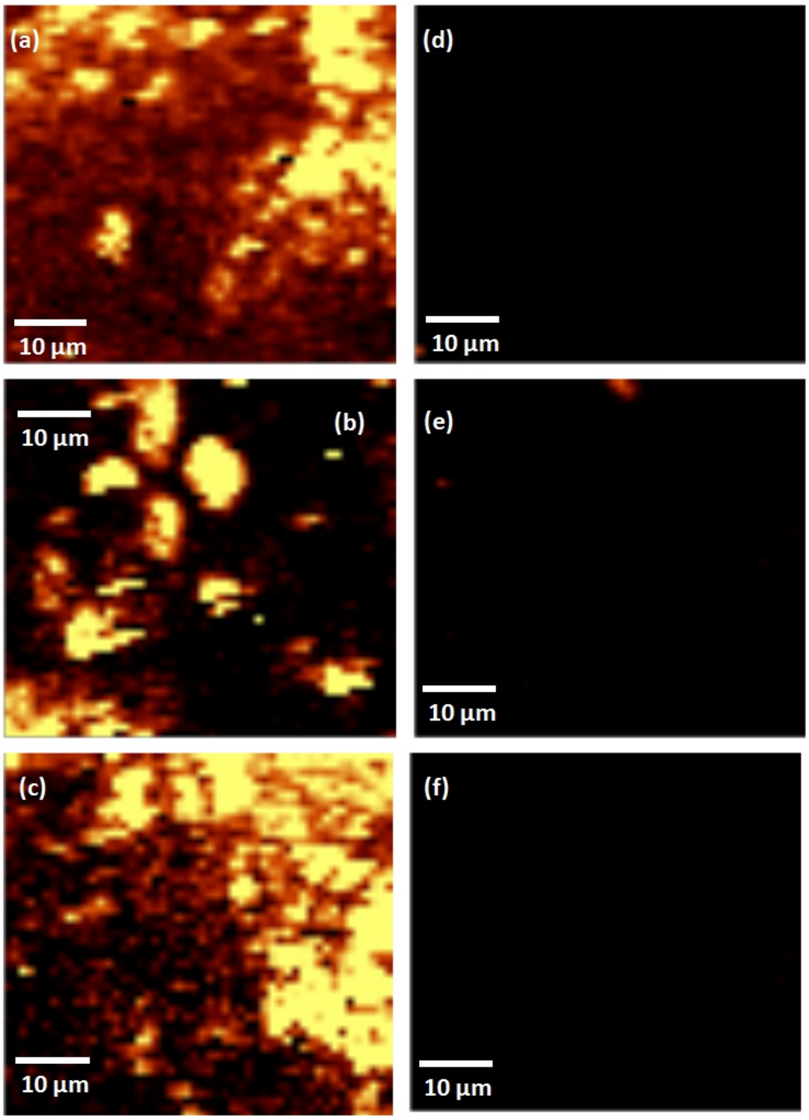

Figure 69. SERS maps of different bone samples using the same false colour scale (λ_{ex}=785 nm). Bright yellow indicates the highest SERS intensity where black indicates the lowest intensity. (a), (b) and (c) are different pieces of bisphonsphonate functionalized nanotag (positive) covered bones; (d) control I; (e) control II; (f) control III.

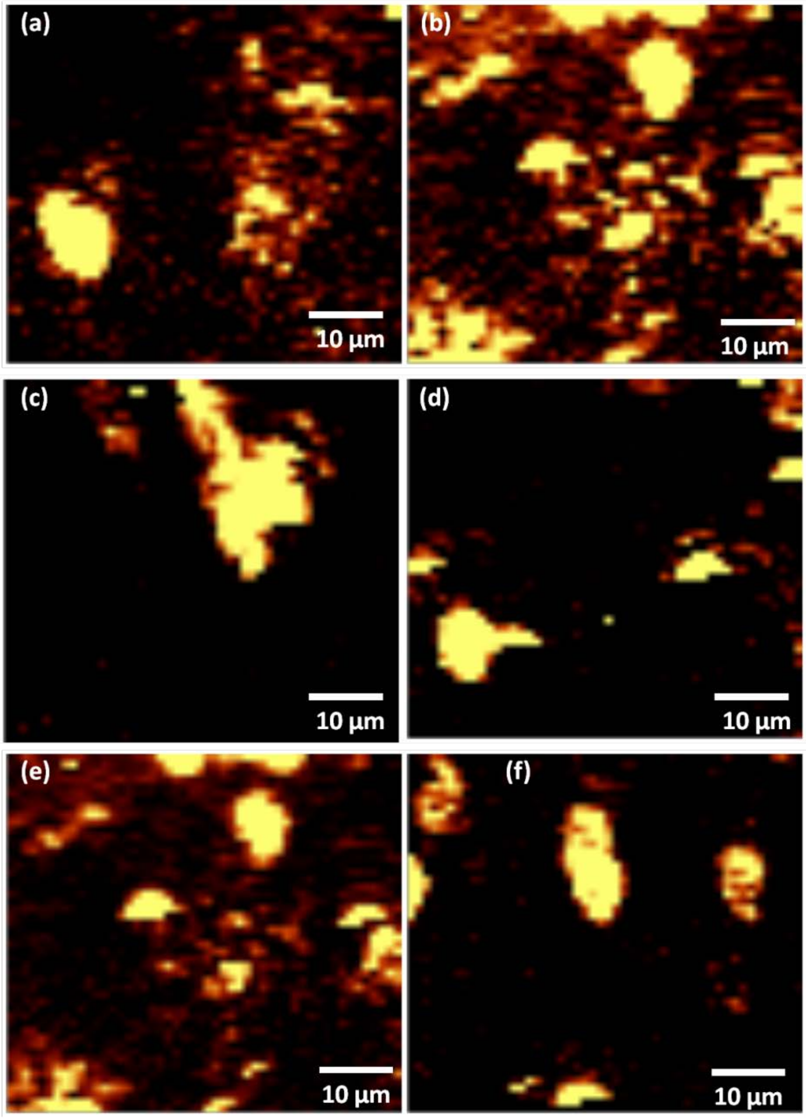

Figure 70. SERS maps of different positive bone samples using the same false colour scale (λ_{ex}=785 nm). Bright yellow indicates the highest SERS intensity where black indicates the lowest intensity. (a) and (b) are from positive bone I; (c) and (d) are from positive bone II; (e) and (f) are from positive bone III.

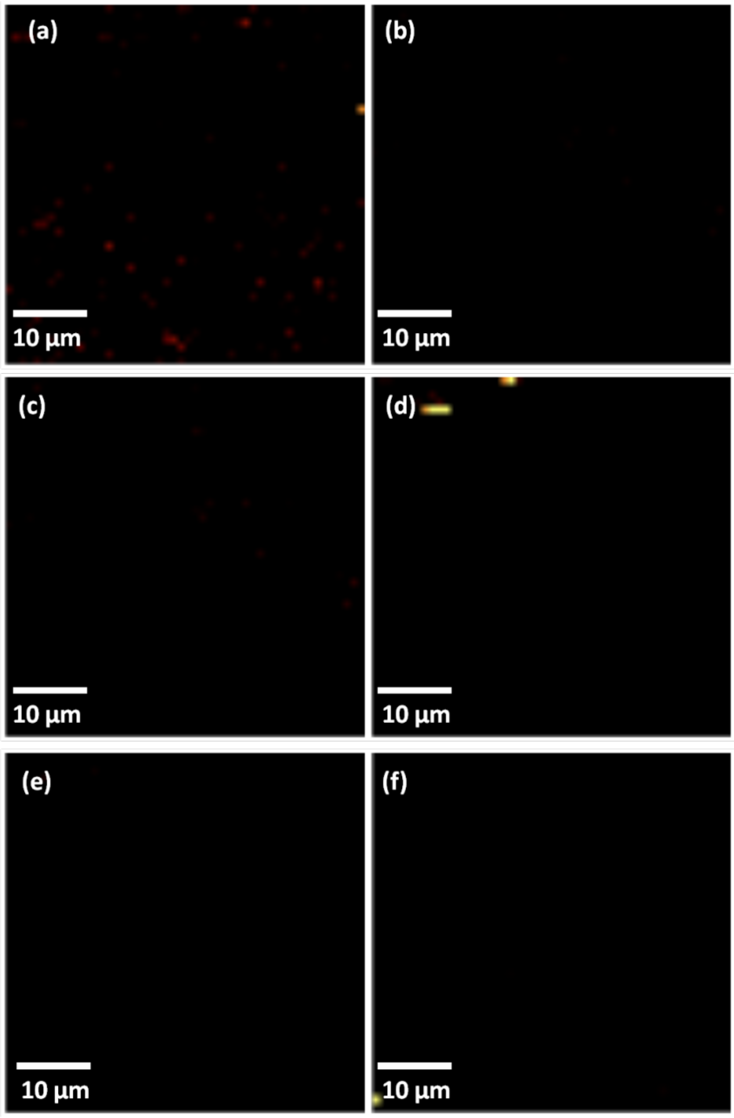

Figure 71. SERS maps of different control bone samples using the same false colour scale (λ_{ex}=785 nm). (a) and (b) are from control bone I without bisphosphonate; (c) and (d) are from control bone II without sulfo-SMCC; (e) and (f) are from control bone III without sulfo-SMCC and bisphosphonate.

To mimic the applications of these nanotags *in vivo*, bisphosphonate functionalized nanotag covered bones were inserted into a 20 mm thick specimen of porcine muscle tissue to simulate the detection of the nanotag functionalized bone through tissue in the case of detecting skeletal metastases (Figure 72). Spatially offset Raman maps were performed across the bone with 2 mm steps 0-20 mm in the x direction and 0-10 mm in the y direction.

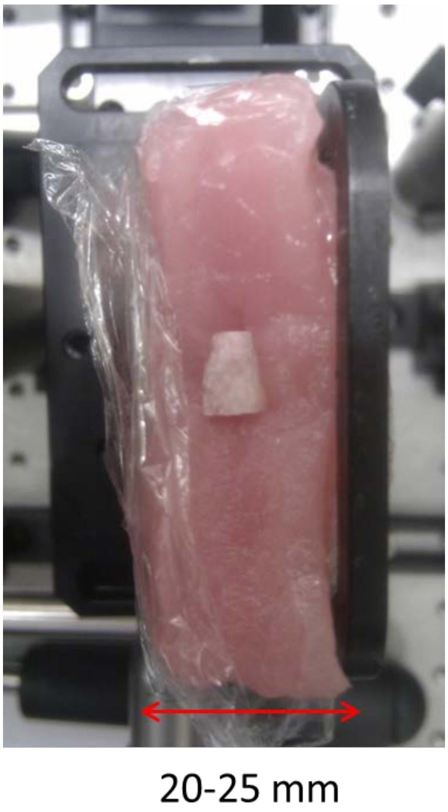

Figure 72. Insertion of positive bone samples into a 20 mm porcine muscle tissue.

The SESORS map shown in Figure 73 was constructed by calculating the principal components of the spectral data set and selecting the one most appropriate to represent the nanoparticle signal from the bone. The second principal component (PC2), which represented the nanoparticle signal from the buried bone, was selected and the loading vector and the scores map is shown in Figure 73, alongside the raw spectrum from the nanotags. The most intense nanotag peak can be seen at around 1200 cm^{-1} and the 960 cm^{-1} signal from the hydroxyapatite is also visible and obviously directly correlated with the raised nanoparticle signal. From Figure 74, the other peaks around 900 cm^{-1} and 1100 cm^{-1} shown in Figure 73 (b) may belong to the porcine muscle tissue. However there is no good correlation between these peaks and spectra of bulk porcine tissue. Unlike previous experiments,[167] a fine distribution of NPs on the surface of the bone was measured rather than a concentrated droplet injected into the tissue. A significant signal reduction particularly above 1250 cm^{-1} was observed through a 20 mm thick tissue when compared to the previous SERS maps carried out on the bone surface directly. Three probable reasons are proposed, first, at these wavelengths both water and myoglobin contribute to the absorption. The 1250 to 1600 cm^{-1} Stokes-shifted range with a 830 nm excitation equals to around 925 to 957 nm, which covers the range where a strong lipid absorption band (~930 nm)[178] and water absorption band (max ~970 nm)[179] are located. Second, a more subtle contribution also comes from a rising absorption in this wavelength region from myoglobin.[180] In addition, the different instrumentation used in SORS measurement and the strong tissue Raman background in this region may also cause this signal reduction.

In the clinical treatment of skeletal metastases, the bisphosphonates would not diffuse through the tissues but angiogenesis derived blood vessels would deliver nanoparticles to the tumor site. The nanotag signals observed through a 20 mm thick porcine muscle tissue shown in Figure 73 provides an alternative way to monitor the disease progress and treatment.

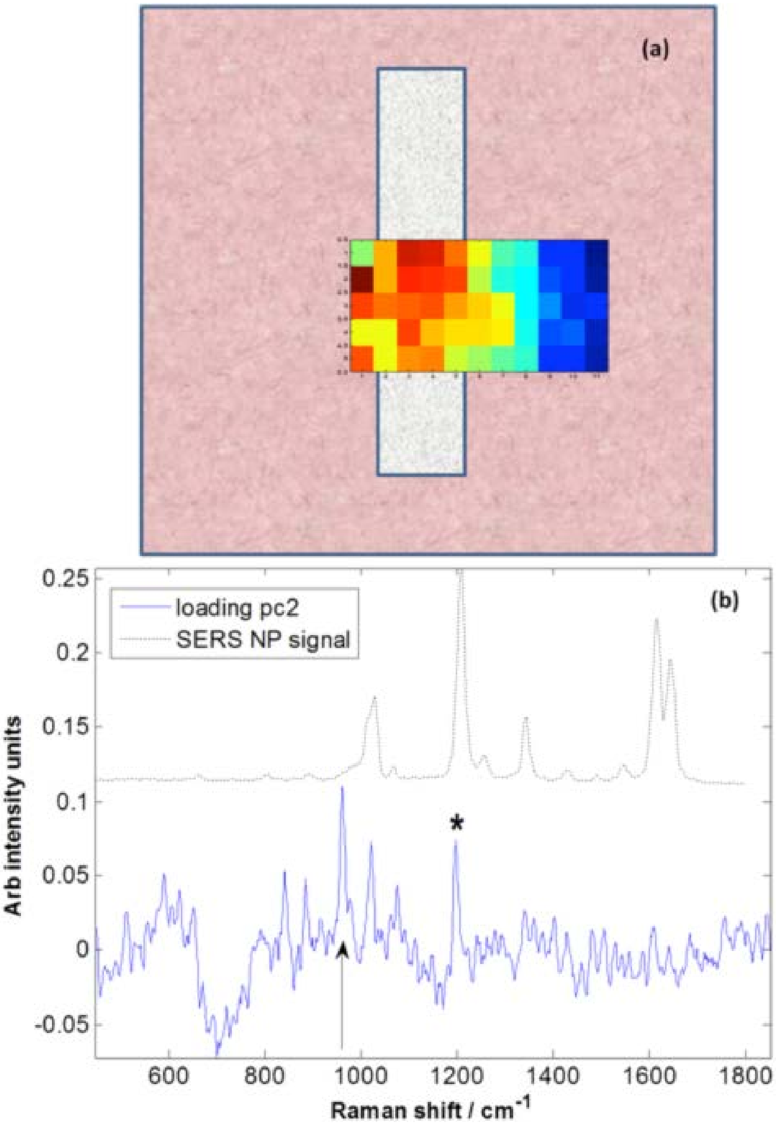

Figure 73. False colour SESORS map of positive nanotag covered bone inserted in a 20 mm thickness porcine tissue (λ_{ex}=830 nm). (a) The grey box represents the bone (approx 8mm across in x dimension, matching 4 pixels in the false colour image). (b) The nanotag characteristic peaks are highlighted in the top spectral plot and the principal component loading plot (bottom) shows the characteristic nanoparticle signal (*) and the hydroxyapatite signal from the bone at 960 cm^{-1} (see arrow). The falsecolour image demonstrates the distribution of the signals as described by PC2.

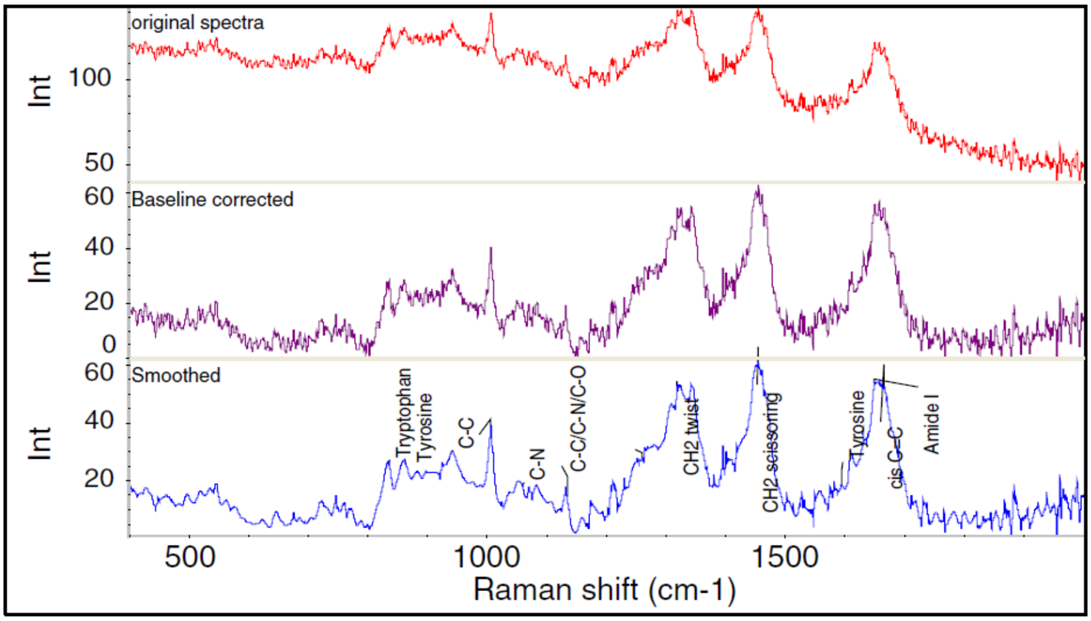

Figure 74. Typical Raman spectrum of pork loins (original, baseline corrected and smoothed).[181]

5.4. Conclusions

In summary, we used porcine bones, containing calcium hydroxyapatite and bisphosphonate-functionalised nanotags as Raman reporters for a simulation study of tracking the bisphosphonate localization through SERS which could be useful both in metastatic breast cancer and bone disease treatments. Functionalized nanotags (positive) specifically bind to bone due to the optimized chelation of the bisphosphonic moiety with superficial Ca^{2+} ions on the bone surface. A recognized nanotag signal was gained from a fine distribution of nanotags on the surface of the bone when placed in a 20 mm thick specimen of porcine muscle tissues through surface enhanced spatially offset Raman spectroscopy (SESORS) demonstrating the great potential for non-invasive *in vivo* bisphosphonate tracking. This work is the first bone/calcium hydroxyapatite-specific tag detectable by SERS/SESORS. The next step is to target tumor calcification *in vitro* using murine osteoblast model with an ultimate aim of targeting tumor calcification *in vivo*.

Chapter 6. Conclusions and Future Work

6.1. Conclusions

In this thesis, the development of an improved synthesis of hollow gold nanospheres (HGNs) is presented, which extended their localised surface plasmon resonances up to 1320 nm with citrate covered surface. HGNs with different surface plasmon resonances were functionalized with different Raman reporters. HGNs and Raman reporters on and off resonance with standard laser excitations were systematically interrogated in isolated and partially aggregated situations respectively. HGNs with a thicker shell always gave higher SERS performance than HGNs with a thinner shell independent of whether it was isolated or in a partially aggregated state or if its LSPR was resonant with the laser excitation or not.

The SERS activity of different types of hollow gold nanospheres was compared to standard gold and silver nanoparticles of similar physical size and surface properties using 1064 nm excitation wavelength. After the addition of salts, a strong SERS signal was observed from hollow gold with a LSPR of 650 nm and a weaker SERS signal from HGNs with a LSPR of 775 nm. However, no obvious SERS signals were observed in the case of standard gold, silver or HGN with a LSPR of 1080 nm. The absorption properties of HGNs were demonstrated by their photothermal response. Different nanoparticle solutions including standard gold, silver, and HGNs were illuminated by a continuous laser source at 785 nm excitation wavelength for 45 min and the photothermal efficiencies were found to be 0.16%, 0.12% and 0.81% (HGN-775) respectively.

The hollow gold nanosphere system was further extended to the higher order structures called “nanoworms” which consisted of connected hollow gold nanospheres. Their compositions as well as their SERS properties, including their multiplexing ability were investigated. The structures of the nanoworms were correlated with SERS maps with the assistance of TEM grids. From the Raman maps and correlated SEM images, the SERS activity was found to be in the order of:

single nanoparticles < fused nanoparticle chains < inter/intra nanoworm interactions. This order is a direct result of the interacting nanoworm structures possessing nanogaps, unlike the case of a single fused nanoworm chain, where no inter particle gaps exist. The localized surface plasmon resonance of the nanostructure was found to have a minimal effect. In addition, a highly SERS-active substrate was fabricated by trapping gold "nanoworms" on commercially available filter membranes providing significant enhancement of the Raman signal as a result of the electromagnetic couplings induced by the dense packing.

Finally, we used porcine bones, containing calcium hydroxyapatite and bisphosphonate-functionalised nanotags as Raman reporters for a simulation study of tracking the bisphosphonate localization through SERS which could be useful both in metastatic breast cancer and bone disease treatments. A recognized nanotag signal was gained from a fine distribution of nanotags on the surface of the bone when placed in a 20 mm thick specimen of porcine muscle tissues through surface enhanced spatially offset Raman spectroscopy (SESORS) demonstrating the great potential for non-invasive *in vivo* bisphosphonate tracking.

In summary, this thesis provides insights into the interesting optical properties of hollow gold nanospheres in the near infrared region and extends the understanding of highly active SERS regions present within a complicated nanosystem. In addition, it also illustrates the first demonstration of a bone/calcium hydroxyapatite-specific tag detectable by SERS/SESORS showing a great potential for non-invasive *in vivo* bisphosphonate tracking in relation to cancers

6.2 Future work

1. Hollow gold nanotags

SERS study in the NIR region attracts a lot of attentions due to the interesting optical sensing window for bioimaging. In section 3.3.1, we already demonstrated the excellent SERS performance of hollow gold nanospheres with a LSPR of 650 nm at 1064 nm excitation. A further idea is to construct highly SERS active hollow gold nanotags using controlled aggregation agents. The ideal way is to use a relatively high concentration of 4-azopyridine which can cause limited aggregation and generate Raman signals at the same time. The SH-PEG-COOH can be used to encapsulate the small aggregates and the presence of the carboxylic acid group provides an opportunity for further surface functionalisations. Preliminary results showed these nanotags generated very intense signal at 1064 nm and it is reasonable to assume that these nanotags could also work at 1550 nm which is an eye-safe wavelength.[182]

2. Utilization of photothermal properties of hollow gold nanospheres

In Figure 34, we showed hollow gold nanospheres with NIR localized surface plasmon resonances demonstrated outstanding photothermal performances. The temperature measured in that experiment was from the bulk solution and therefore, the next step is to quantify the localised temperature. The anti-stokes shift is very sensitive to temperature and we can use the ratio of anti-stokes and stokes shift to get an estimation of the localized temperature on the nanosphere surface.[183] In addition, we can also do some thermo-dependent organic reactions to investigate the approximate localised temperature.

3. Tracking bisphosphonate *in vitro* and *in vivo*

We already demonstrated that the bisphosphonate functionalised nanotags can specifically bind to bone due to the optimized chelation of the bisphosphonic moiety with superficial Ca^{2+} ions on the bone surface. The next stage is to test whether we can use these functionalized nanotags to track the cell life cycle of osteoblast cells using SERS mapping and then create a connection with the disease diagnosis.

However, these steps are not easy due to the sticky nanotag surface which will result in lots of non-specific bindings. Therefore, a lot of effort should be put in resolving this issues before moving towards the real clinical applications.

Appendix

Journal papers

1. **Hai-nan Xie**, Iain A. Larmour, Vasiliki Tileli, Ai Leen Koh, David W. McComb, Karen Faulds, and Duncan Graham, "Deciphering Surface Enhanced Raman Scattering Activity of Gold Nanoworms through Optical Correlations", J. Phys. Chem. C, 2011, 115, 20515–20522.
2. **Hai-nan Xie**, Iain A. Larmour, W. Ewen Smith, Karen Faulds, and Duncan Graham, "Enhancing the SERS Properties of Nanoworms by Matrix Formation", Analyst, 2012,137, 2297-2299.
3. **Hai-nan Xie**, Iain A. Larmour, W. Ewen Smith, Karen Faulds, and Duncan Graham, "Surface Enhanced Raman Scattering Investigation of Hollow Gold Nanospheres", J. Phys. Chem. C, 2012, 116, 8338-8342.
4. **Hai-nan Xie**, Ross Stevenson , Nicholas Stone , Aaron Hernandez-Santana , Karen Faulds, and Duncan Graham, "Tracking Bisphosphonates through a 20 mm Thick Porcine Tissue by Using Surface-Enhanced Spatially Offset Raman Spectroscopy", Angew. Chem. Int. Ed., 2012, 51, 8509 –8511
5. **Hai-nan Xie**, Iain A. Larmour, Yi-Chieh Chen, Alastair W. Wark, Karen Faulds, and Duncan Graham, "Synthesis and NIR Optical Properties of Hollow Gold Nanospheres with LSPR Greater than One Micrometer", Nanoscale, 2013, DOI: 10.1039/C2NR33187J.

Conference presentations

Note: presenters underlined.

1. **Hai-nan Xie** and Duncan Graham, "Deciphering Surface Enhanced Raman Scattering Activity of Gold Nanoworms through Optical Correlations", 242nd ACS National Meeting in Denver, Colorado, August 28 – September 1, 2011. **Oral** Presentation

2. Melissa Skibba, **Hai-nan Xie**, Ross Stevenson, Karen Faulds, and Duncan Graham, “Detection of nitric oxide release in cell medium using diaminofluorescein dyes and Surface Enhanced Resonance technology”, 243rd ACS National Meeting in San Diego, California, March 25- 29 2012. **Poster** Presentation

3. **Hai-nan Xie** and Duncan Graham, “Surface Enhanced Raman Scattering Investigation of Hollow Gold Nanospheres”, Analytical Research Forum in Durham, UK, 02 July–04 July, 2012. **Oral** Presentation

4. **Hai-nan Xie** and Duncan Graham, “Tracking Bisphosphonates through a 20 mm Thick Porcine Tissue by Using Surface-Enhanced Spatially Offset Raman Spectroscopy”, Challenges in Nanoscience (ISACS9), Xiamen, China, August 31-September 3, 2012**.** **Oral** Presentation

References

(1) Saha, K.; Agasti, S. S.; Kim, C.; Li, X.; Rotello, V. M. *Chem. Rev.* **2012**, *112*, 2739-2779.

(2) Grzelczak, M.; Perez-Juste, J.; Mulvaney, P.; Liz-Marzan, L. M. *Chem. Soc. Rev.* **2008**, *37*, 1783-1791.

(3) Larmour, I. A.; Graham, D. *Analyst* **2011**, *136*, 3831-3853.

(4) Giljohann, D. A.; Seferos, D. S.; Daniel, W. L.; Massich, M. D.; Patel, P. C.; Mirkin, C. A. *Angew. Chem. Int. Ed.*, **2010**, *49*, 3280-3294.

(5) Boisselier, E.; Astruc, D. *Chem. Soc. Rev.* **2009**, *38*, 1759-1782.

(6) Turkevich, J.; Stevenson, P. C.; Hillier, J. *Discuss. Faraday Soc.* **1951**, *11*, 55-75.

(7) Frens, G. *Nature: Phys. Sci* **1973**, *241*, 20.

(8) Chow, M. K.; Zukoski, C. F. *Colloid Interface Sci* **1994**, *165*, 97-109.

(9) Krpetić, Ž.; Guerrini, L.; Larmour, I. A.; Reglinski, J.; Faulds, K.; Graham, D. *Small* **2012**, *8*, 707-714.

(10) Giersig, M.; Mulvaney, P. *Langmuir* **1993**, *9*, 3408-3413.

(11) Brust, M.; Walker, M.; Bethell, D.; Schiffrin, D. J.; Whyman, R. *J. Chem. Soc., Chem. Commun.* **1994**, 801-802.

(12) Tao, A. R.; Habas, S.; Yang, P. *Small* **2008**, *4*, 310-325.

(13) Prasad, B. L. V.; Stoeva, S. I.; Sorensen, C. M.; Klabunde, K. J. *Chem. Mater.* **2003**, *15*, 935-942.

(14) J. Zhong, C.; X. Zhang, W.; L. Leibowitz, F.; H. Eichelberger, H. *Chem. Commun.* **1999**, 1211-1212.

(15) Pol, V. G.; Gedanken, A.; Calderon-Moreno, J. *Chem. Mater.* **2003**, *15*, 1111-1118.

(16) Dawson, A.; Kamat, P. V. *J. Phys. Chem. B* **2000**, *104*, 11842-11846.

(17) Wei, G.-T.; Liu, F.-K.; Wang, C. R. C. *Anal. Chem.* **1999**, *71*, 2085-2091.

(18) Myroshnychenko, V.; Rodriguez-Fernandez, J.; Pastoriza-Santos, I.; Funston, A. M.; Novo, C.; Mulvaney, P.; Liz-Marzan, L. M.; Garcia de Abajo, F. J. *Chem. Soc. Rev.* **2008**, *37*, 1792-1805.

(19) Le Ru, E. C.; Etchegoin, P. G. *Principles of Surface-Enhanced Raman Spectroscopy and related plasmonic effects*; Elsevier: Amsterdam, 2009.

(20) Link, S.; El-Sayed, M. A. *J. Phys. Chem. B* **1999**, *103*, 4212-4217.

(21) Mie, G. *Annals of Phys.* **1908**, *330*, 377-445.

(22) Liu, D.; Wang, Z.; Jiang, X. *Nanoscale*, *3*, 1421-1433.

(23) Mirkin, C. A.; Letsinger, R. L.; Mucic, R. C.; Storhoff, J. J. *Nature* **1996**, *382*, 607-609.

(24) Rosi, N. L.; Mirkin, C. A. *Chem. Rev.* **2005**, *105*, 1547-1562.

(25) Xia, F.; Zuo, X.; Yang, R.; Xiao, Y.; Kang, D.; Vallee-Belisle, A.; Gong, X.; Yuen, J. D.; Hsu, B. B. Y.; Heeger, A. J.; Plaxco, K. W. *Proc. Natl. Acad. Sci. USA*, *107*, 10837-10841.

(26) Onyido, I.; Norris, A. R.; Buncel, E. *Chem. Rev.* **2004**, *104*, 5911-5930.

(27) Lee, J.-S.; Han, M. S.; Mirkin, C. A. *Angew. Chem. Int. Ed.* **2007**, *46*, 4093-4096.

(28) Xue, X.; Wang, F.; Liu, X. *J. Am. Chem. Soc.* **2008**, *130*, 3244-3245.

(29) Kim, H. N.; Ren, W. X.; Kim, J. S.; Yoon, J. *Chem. Soc. Rev.* **2012**, *41*, 3210-3244.

(30) Otsuka, H.; Akiyama, Y.; Nagasaki, Y.; Kataoka, K. *J. Am. Chem. Soc.* **2001**, *123*, 8226-8230.

(31) Huang, C.-C.; Huang, Y.-F.; Cao, Z.; Tan, W.; Chang, H.-T. *Anal. Chem.* **2005**, *77*, 5735-5741.

(32) Dykman, L. A.; Bogatyrev, V. A.; Khlebtsov, B. N.; Khlebtsov, N. G. *Anal. Biochem.* **2005**, *341*, 16-21.

(33) Thanh, N. T. K.; Rosenzweig, Z. *Anal. Chem.* **2002**, *74*, 1624-1628.

(34) Sapsford, K. E.; Berti, L.; Medintz, I. L. *Angew. Chem. Int. Ed.* **2006**, *45*, 4562-4589.

(35) Huang, T.; Murray, R. W. *Langmuir* **2002**, *18*, 7077-7081.

(36) Huang, C.-C.; Chang, H.-T. *Analytical Chemistry* **2006**, *78*, 8332-8338.

(37) Chen, S.-J.; Chang, H.-T. *Anal. Chem.* **2004**, *76*, 3727-3734.

(38) Dubertret, B.; Calame, M.; Libchaber, A. J. *Nat Biotech* **2001**, *19*, 365-370.

(39) Maxwell, D. J.; Taylor, J. R.; Nie, S. *J. Am. Chem. Soc.* **2002**, *124*, 9606-9612.

(40) Seferos, D. S.; Giljohann, D. A.; Hill, H. D.; Prigodich, A. E.; Mirkin, C. A. *J. Am. Chem. Soc.* **2007**, *129*, 15477-15479.

(41) Zheng, D.; Seferos, D. S.; Giljohann, D. A.; Patel, P. C.; Mirkin, C. A. *Nano Lett.* **2009**, *9*, 3258-3261.

(42) Prigodich, A. E.; Seferos, D. S.; Massich, M. D.; Giljohann, D. A.; Lane, B. C.; Mirkin, C. A. *ACS Nano* **2009**, *3*, 2147-2152.

(43) Medintz, I. L.; Clapp, A. R.; Mattoussi, H.; Goldman, E. R.; Fisher, B.; Mauro, J. M. *Nat. Mater.* **2003**, *2*, 630-638.

(44) Dyadyusha, L.; Yin, H.; Jaiswal, S.; Brown, T.; Baumberg, J. J.; Booy, F. P.; Melvin, T. *Chem. Comm.* **2005**, 3201-3203.

(45) Willets, K. A.; Van Duyne, R. P. *Annu. Rev. Phys. Chem.* **2007**, *58*, 267-297.

(46) Englebienne, P.; Van Hoonacker, A.; Verhas, M. *Analyst* **2001**, *126*, 1645-1651.

(47) Wang, J. *Small* **2005**, *1*, 1036-1043.

(48) Matsui, J.; Akamatsu, K.; Hara, N.; Miyoshi, D.; Nawafune, H.; Tamaki, K.; Sugimoto, N. *Anal. Chem.* **2005**, *77*, 4282-4285.

(49) Alkilany, A. M.; Thompson, L. B.; Boulos, S. P.; Sisco, P. N.; Murphy, C. J. *Adv. Drug Deliv. Rev.* ***2012***, *64*, 190-199.

(50) Nikoobakht, B.; El-Sayed, M. A. *Chem. Mater.* **2003**, *15*, 1957-1962.

(51) Weissleder, R. *Nat. Biotech.* **2001**, *19*, 316-317.

(52) Eghtedari, M.; Oraevsky, A.; Copland, J. A.; Kotov, N. A.; Conjusteau, A.; Motamedi, M. *Nano Lett.* **2007**, *7*, 1914-1918.

(53) Skrabalak, S. E.; Au, L.; Lu, X.; Li, X.; Xia, Y. *Nanomedicine* **2007**, *2*, 657-668.

(54) Chen, J.; Wang, D.; Xi, J.; Au, L.; Siekkinen, A.; Warsen, A.; Li, Z.-.; Zhang, H.; Xia, Y.; Li, X. *Nano Lett.* **2007**, *7*, 1318-1322.

(55) Skrabalak, S. E.; Chen, J.; Sun, Y.; Lu, X.; Au, L.; Cobley, C. M.; Xia, Y. *Acc. Chem. Res.* **2008**, *41*, 1587-1595.

(56) Skrabalak, S. E.; Au, L.; Li, X.; Xia, Y. *Nat. Protocols* **2007**, *2*, 2182-2190.

(57) Chen, J.; Saeki, F.; Wiley, B. J.; Cang, H.; Cobb, M. J.; Li, Z.-Y.; Au, L.; Zhang, H.; Kimmey, M. B.; Li; Xia, Y. *Nano Lett.* **2005**, *5*, 473-477.

(58) Yang, X.; Skrabalak, S. E.; Li, Z.-Y.; Xia, Y.; Wang, L. V. *Nano Lett.* **2007**, *7*, 3798-3802.

(59) Yavuz, M. S.; Cheng, Y.; Chen, J.; Cobley, C. M.; Zhang, Q.; Rycenga, M.; Xie, J.; Kim, C.; Song, K. H.; Schwartz, A. G.; Wang, L. V.; Xia, Y. *Nat. Mater.* **2009**, *8*, 935-939.

(60) Schwartzberg, A. M.; Olson, T. Y.; Talley, C. E.; Zhang, J. Z. *J. Phys. Chem. B* **2006**, *110*, 19935-19944.

(61) Zhang, J. Z. *J. Phys. Chem. Lett.* **2010**, *1*, 686-695.

(62) Souza, G. R.; Levin, C. S.; Hajitou, A.; Pasqualini, R.; Arap, W.; Miller, J. H. *Anal. Chem.* **2006**, *78*, 6232-6237.

(63) Lee, S.; Chon, H.; Lee, M.; Choo, J.; Shin, S. Y.; Lee, Y. H.; Rhyu, I. J.; Son, S. W.; Oh, C. H. *Biosens. Bioelectron.* **2009**, *24*, 2260-2263.

(64) Chon, H.; Lim, C.; Ha, S.-M.; Ahn, Y.; Lee, E. K.; Chang, S.-I.; Seong, G. H.; Choo, J. *Anal. Chem.* **2010**, *82*, 5290-5295.

(65) Liu, S.; Liu, J.; Han, X.; Cui, Y.; Wang, W. *Biosens. Bioelectron.* **2010**, *25*, 1640-1645.

(66) Melancon, M. P.; Lu, W.; Yang, Z.; Zhang, R.; Cheng, Z.; Elliot, A. M.; Stafford, J.; Olson, T.; Zhang, J. Z.; Li, C. *Mol. Cancer Ther.* **2008**, *7*, 1730-1739.

(67) Lu, W.; Xiong, C.; Zhang, G.; Huang, Q.; Zhang, R.; Zhang, J. Z.; Li, C. *Clin. Cancer Res.* **2009**, *15*, 876-886.

(68) Yguerabide, J.; Yguerabide, E. E. *Anal. Biochem.* **1998**, *262*, 157-176.

(69) Duckett, S.; Gilbert, B. *Foundations of Spectroscopy*; Oxford University Press, 2000.

(70) wikipedia http://en.wikipedia.org/wiki/Zeta_potential.

(71) Li, Y.; Jing, C.; Zhang, L.; Long, Y.-T. *Chemical Society Reviews*, *41*, 632.

(72) Goldstein, J.; Newbury, D. E.; Joy, D. C.; Lyman, C. E.; Echlin, P.; Lifshin, E.; Sawyer, L.; Michael, J. R. *Scanning Electron Microscopy and X-ray Microanalysis*; Springer, 2005.

(73) Williams, D. B.; Carter, C. B. *Transmission Electron Microscopy: A Textbook for Materials Science*; Springer, 2004.

(74) Egerton, R. F. *Rep. Prog. Phys.* **2009**, *72*, 016502.

(75) Raman, C. V.; Krishnan, K. S. *Nature* **1928**, *121*, 501-502.

(76) Ewen, S.; NJ, Modern Raman Spectroscopy–A Practical Approach, John Wiley: 2005.

(77) Moskovits, M. *J. Raman Spectrosc.* **2005**, *36*, 485.

(78) Graham, D.; Faulds, K. *Chem. Soc. Rev.* **2008**, *37*, 1042.

(79) Faulds, K.; McKenzie, F.; Smith, W. E.; Graham, D. *Angew. Chem. Int. Ed.* **2007**, *46*, 1829-1831.

(80) Stiles, P. L.; Dieringer, J. A.; Shah, N. C.; Van Duyne, R. P. *Annu. Rev. Anal. Chem.* **2008**, *1*, 601.

(81) Fang, Y.; Seong, N. H.; Dlott, D. D. *Science* **2008**, *321*, 388.

(82) Wustholz, K. L.; Henry, A.-I.; McMahon, J. M.; Freeman, R. G.; Valley, N.; Piotti, M. E.; Natan, M. J.; Schatz, G. C.; Duyne, R. P. V. *J. Am. Chem. Soc.*, *132*, 10903.

(83) Le Ru, E. C.; Galloway, C.; Etchegoin, P. G. *Phys. Chem. Chem. Phys.* **2006**, *8*, 3083.

(84) Wustholz, K. L.; Henry, A.-I.; McMahon, J. M.; Freeman, R. G.; Valley, N.; Piotti, M. E.; Natan, M. J.; Schatz, G. C.; Duyne, R. P. V. *J. Am. Chem. Soc,* **2010**, *132*, 10903.

(85) McFarland, A. D.; Young, M. A.; Dieringer, J. A.; Van Duyne, R. P. *J. Phys. Chem. ,B* **2005**, *109*, 11279.

(86) Nie, S.; Emory, S. R. *Science* **1997**, *275*, 1102.

(87) Kumar, P. S.; Pastoriza-Santos, I.; Rodríguez-González, B.; Abajo, F. J. G. d.; Liz-Marzán, L. M. *Nanotechnology* **2008**, *19*, 015606.

(88) Oldenburg, S. J.; Averitt, R. D.; Westcott, S. L.; Halas, N. J. *Chem. Phys. Lett.*, **1998**, *288*, 243.

(89) Brinson, B. E.; Lassiter, J. B.; Levin, C. S.; Bardhan, R.; Mirin, N.; Halas, N. J. *Langmuir* **2008**, *24*, 14166.

(90) Hirsch, L. R.; Jackson, J. B.; Lee, A.; Halas, N. J.; West, J. L. *Anal. Chem.*, **2003**, *75*, 2377.

(91) Sershen, S. R.; Westcott, S. L.; Halas, N. J.; West, J. L. *J. Biomed. Mater. Res.* **2000**, *51*, 293.

(92) O'Neal, D. P.; Hirsch, L. R.; Halas, N. J.; Payne, J. D.; West, J. L. *Cancer Lett.*, **2004**, *209*, 171.

(93) Gobin, A. M.; O'Neal, D. P.; Watkins, D. M.; Halas, N. J.; Drezek, R. A.; West, J. L. *Laser Surg. Med.*, **2005**, *37*, 123.

(94) Hirsch, L. R.; Stafford, R. J.; Bankson, J. A.; Sershen, S. R.; Rivera, B.; Price, R. E.; Hazle, J. D.; Halas, N. J.; West, J. L. *Proc. Natl. Acad. Sci. USA*, **2003**, *100*, 13549.

(95) Loo, C.; Lowery, A.; Halas, N.; West, J.; Drezek, R. *Nano Lett.* **2005**, *5*, 709.

(96) Loo, C.; Hirsch, L.; Lee, M.-H.; Chang, E.; West, J.; Halas, N.; Drezek, R. *Opt. Lett.* **2005**, *30*, 1012.

(97) Gobin, A. M.; Lee, M. H.; Halas, N. J.; James, W. D.; Drezek, R. A.; West, J. L. *Nano Lett.* **2007**, *7*, 1929.

(98) Cho, E. C.; Au, L.; Zhang, Q.; Xia, Y. *Small* **2010**, *6*, 517.

(99) Preciado-Flores, S.; Wang, D.; Wheeler, D. A.; Newhouse, R.; Hensel, J. K.; Schwartzberg, A.; Wang, L.; Zhu, J.; Barboza-Flores, M.; Zhang, J. Z. *J. Mater. Chem.* **2011**, *21*, 2344.

(100) Bashkatov, A. N.; Genina, E. A.; Kochubey, V. I.; Tuchin, V. V. *J. Phys. D: Appl. Phys.* **2005**, *38*, 2543.

(101) Izumi, C. M. S.; Moffitt, M. G.; Brolo, A. G. *J. Phys. Chem. C* **2011**, *115*, 19104.

(102) Lal, S.; Grady, N. K.; Kundu, J.; Levin, C. S.; Lassiter, J. B.; Halas, N. J. *Chem. Soc. Rev.* **2008**, *37*, 898.

(103) Gellner, M.; Küstner, B.; Schlücker, S. *Vib. Spectrosc.* **2009**, *50*, 43.

(104) Laurence, T. A.; Braun, G.; Talley, C.; Schwartzberg, A.; Moskovits, M.; Reich, N.; Huser, T. *J. Am. Chem. Soc.* **2008**, *131*, 162.

(105) Schwartzberg, A. M.; Olson, T. Y.; Talley, C. E.; Zhang, J. Z. *J. Phys. Chem. B* **2006**, *110*, 19935.

(106) Wikipedia *http://en.wikipedia.org/wiki/Schlenk_line*.

(107) Xie, H.-n.; Larmour, I. A.; Tileli, V.; Koh, A. L.; McComb, D. W.; Faulds, K.; Graham, D. *J. Phys. Chem. C* **2011**, *115*, 20515.

(108) McLintock, A.; Hunt, N.; Wark, A. W. *Chem. Commun.* **2011**, *47*, 3757.

(109) Schwartzberg, A. M.; Olson, T. Y.; Talley, C. E.; Zhang, J. Z. *J. Phys. Chem. C* **2007**, *111*, 16080.

(110) Peña-Rodríguez, O.; Pal, U. *J. Phys. Chem. C* **2011**, *115*, 22271.

(111) Hao, E.; Li, S.; Bailey, R. C.; Zou, S.; Schatz, G. C.; Hupp, J. T. *J. Phys. Chem. B* **2004**, *108*, 1224.

(112) Le Ru, E. C.; Etchegoin, P. G.; Meyer, M. *J. Chem. Phys.* **2006**, *125*, 204701.

(113) Larmour, I. A.; Faulds, K.; Graham, D. *J. Phys. Chem. C* **2010**, *114*, 13249.

(114) Martin, L. C.; Larmour, I. A.; Faulds, K.; Graham, D. *Chem. Commun.* **2010**, *46*, 5247.

(115) Meyer, M.; Le Ru, E. C.; Etchegoin, P. G. *J. Phys. Chem. B* **2006**, *110*, 6040.

(116) Etchegoin, P. G.; Meyer, M.; Blackie, E.; Le Ru, E. C. *Anal. Chem.* **2007**, *79*, 8411.

(117) Knappenberger, K. L.; Schwartzberg, A. M.; Dowgiallo, A.-M.; Lowman, C. A. *J. Am. Chem. Soc.* **2009**, *131*, 13892.

(118) Chandra, M.; Dowgiallo, A.-M.; Knappenberger, K. L. *J. Am. Chem. Soc.* **2010**, *132*, 15782.

(119) Mahmoud, M. A.; Snyder, B.; El-Sayed, M. A. *J. Phys. Chem. C* **2010**, *114*, 7436.

(120) Álvarez-Puebla, R. A. *J. Phys. Chem. Lett.***2012**, *3*, 857.

(121) Oldenburg, S. J.; Westcott, S. L.; Averitt, R. D.; Halas, N. J. *J. Chem. Phys.* **1999**, *111*, 4729.

(122) Lefrant, S.; Baltog, I.; Baibarac, M.; Mevellec, J. Y.; Chauvet, O. *Carbon* **2002**, *40*, 2201.

(123) Leopold, N.; Lendl, B. *J. Phys. Chem. B* **2003**, *107*, 5723.

(124) Nikoobakht, B.; El-Sayed, M. A. *J. Phys. Chem. A* **2003**, *107*, 3372.

(125) Wheeler, D. A.; Newhouse, R. J.; Wang, H.; Zou, S.; Zhang, J. Z. *J. Phys. Chem. C* **2010**, *114*, 18126.

(126) Gibson, K. F.; Correia-Ledo, D.; Couture, M.; Graham, D.; Masson, J.-F. *Chem. Commun.* **2011**, *47*, 3404.

(127) Zhang, Y. *Plasmonics* **2011**, *6*, 393.

(128) Chen, H.; Shao, L.; Ming, T.; Sun, Z.; Zhao, C.; Yang, B.; Wang, J. *Small*, *6*, 2272.

(129) Chen, G.; Wang, Y.; Yang, M.; Xu, J.; Goh, S. J.; Pan, M.; Chen, H. *J. Am. Chem. Soc.* **2010**, *132*, 3644.

(130) Braun, G. B.; Lee, S. J.; Laurence, T.; Fera, N.; Fabris, L.; Bazan, G. C.; Moskovits, M.; Reich, N. O. *J. Phys. Chem. C* **2009**, *113*, 13622.

(131) Khan, I.; Cunningham, D.; Littleford, R. E.; Graham, D.; Smith, W. E.; McComb, D. W. *Anal. Chem.* **2005**, *78*, 224.

(132) Camden, J. P.; Dieringer, J. A.; Wang, Y.; Masiello, D. J.; Marks, L. D.; Schatz, G. C.; Van Duyne, R. P. *J. Am. Chem. Soc.* **2008**, *130*, 12616.

(133) Jones, M. R.; Osberg, K. D.; Macfarlane, R. J.; Langille, M. R.; Mirkin, C. A. *Chem. Rev.* **2011**, *111*, 3736.

(134) Abu Hatab, N. A.; Oran, J. M.; Sepaniak, M. J. *ACS Nano* **2008**, *2*, 377.

(135) Haynes, C. L.; Van Duyne, R. P. *J. Phys. Chem. B* **2001**, *105*, 5599-5611.

(136) Strehle, K. R.; Cialla, D.; Rösch, P.; Henkel, T.; Köhler, M.; Popp, J. *Anal. Chem.* **2007**, *79*, 1542-1547.

(137) Tran, C. D. *Anal. Chem.* **1984**, *56*, 824-826.

(138) Xu, P.; Mack, N. H.; Jeon, S.-H.; Doorn, S. K.; Han, X.; Wang, H.-L. *Langmuir* **2010**, *26*, 8882-8886.

(139) Kassu, A.; Robinson, P.; Sharma, A.; Ruffin, P. B.; Brantley, C.; Edwards, E.; 1 ed.; Dobisz, E. A., Eldada, L. A., Eds.; SPIE: San Diego, California, USA, 2010; Vol. 7764, p 77640M-7.

(140) Mondal, B.; Saha, S. K. *Chem. Phys. Lett.* **2010**, *497*, 89-93.

(141) Lee, C. H.; Tian, L.; Singamaneni, S. *ACS Appl. Mater. Interfaces* **2010**, *2*, 3429-3435.

(142) Shimada,M.; Yamada, Y.; Itoh, M.; Yatagai, T. *Phys. Med. Biol.* **2001**, *46*, 2385.

(143) Hu, M.; Chen, J.; Marquez, M.; Xia, Y.; Hartland, G. V. *J. Phys. Chem. C* **2007**, *111*, 12558.

(144) Seize, T. K. *South. Med. J.* **1977**, *70*, 1299.

(145) Faulds, K.; Jarvis, R.; Smith, W. E.; Graham, D.; Goodacre, R. *Analyst* **2008**, *133*, 1505.

(146) Le Ru, E. C.; Meyer, M.; Etchegoin, P. G. *J. Phys. Chem. B* **2006**, *110*, 1944-1948.

(147) Wang, Z. B.; Luk'yanchuk, B. S.; Guo, W.; Edwardson, S. P.; Whitehead, D. J.; Li, L.; Liu, Z.; Watkins, K. G. *J. Chem. Phys.* **2008**, *128*.

(148) Hu, M.; Novo, C.; Funston, A.; Wang, H.; Staleva, H.; Zou, S.; Mulvaney, P.; Xia, Y.; Hartland, G. V. *J. Mater. Chem.* **2008**, *18*, 1949-1960.

(149) Camden, J. P.; Dieringer, J. A.; Zhao, J.; Van Duyne, R. P. *Acc. Chem. Res.* **2008**, *41*, 1653.

(150) Weber, M. L.; Litz, J. P.; Masiello, D. J.; Willets, K. A. *ACS Nano* **2012**, *6*, 1839.

(151) Stranahan, S. M.; Willets, K. A. *Nano Lett.* **2010**, *10*, 3777.

(152) Cang, H.; Labno, A.; Lu, C.; Yin, X.; Liu, M.; Gladden, C.; Liu, Y.; Zhang, X. *Nature* **2011**, *469*, 385.

(153) Rycenga, M.; Cobley, C. M.; Zeng, J.; Li, W.; Moran, C. H.; Zhang, Q.; Qin, D.; Xia, Y. *Chem. Rev.* **2011**, *111*, 3669.

(154) Xu, S.; Zhao, B.; Xu, W.; Fan, Y. *Colloids Surf. A* **2005**, *257-258*, 313.

(155) Brown, J.; Coleman, R. *Breast Cancer Res* **2002**, *4*, 24

(156) Theriault, R. L.; Lipton, A.; Hortobagyi, G. N.; Leff, R.; Glück, S.; Stewart, J. F.; Costello, S.; Kennedy, I.; Simeone, J.; Seaman, J. J.; Knight, R. D.; Mellars, K.; Heffernan, M.; Reitsma, D. J.; Group, f. t. P. A. B. C. S. *J. Clin. Oncol.* **1999**, *17*, 846.

(157) Hortobagyi, G. N.; Theriault, R. L.; Porter, L.; Blayney, D.; Lipton, A.; Sinoff, C.; Wheeler, H.; Simeone, J. F.; Seaman, J.; Knight, R. D.; Heffernan, M.; Reitsma, D. J.; Kennedy, I.; Allan, S. G.; Mellars, K. *N. Engl. J. Med.* **1996**, *335*, 1785.

(158) Catterall, J.; Cawston, T. *Arthritis Res Ther* **2003**, *5*, 12

(159) Zhang, S.; Gangal, G.; Uludag, H. *Chem. Soc. Rev.* **2007**, *36*, 507.

(160) Zaheer, A.; Lenkinski, R. E.; Mahmood, A.; Jones, A. G.; Cantley, L. C.; Frangioni, J. V. *Nat Biotech* **2001**, *19*, 1148.

(161) Wang, K.; Allen, L.; Fung, E.; Chan, C. C.; Chan, J. C. S.; Griffith, J. F. *Clin. Nucl. Med.* **2005**, *30*, 655.

(162) Christoffersen, M. R.; Christoffersen, J. r. *Cryst. Growth Des.* **2002**, *3*, 79.

(163) Hernandez-Santana, A.; Yavorskyy, A.; Olinyole, A.; McCarthy, G. M.; McMahon, G. P. *Chem. Commun* **2008**, 2686.

(164) Matousek, P.; Clark, I. P.; Draper, E. R. C.; Morris, M. D.; Goodship, A. E.; Everall, N.; Towrie, M.; Finney, W. F.; Parker, A. W. *Appl. Spectrosc.* **2005**, *59*, 393.

(165) Matousek, P.; Morris, M. D.; Everall, N.; Clark, I. P.; Towrie, M.; Draper, E.; Goodship, A.; Parker, A. W. *Appl. Spectrosc.* **2005**, *59*, 1485.

(166) Stone, N.; Faulds, K.; Graham, D.; Matousek, P. *Anal. Chem.* **2010**, *82*, 3969.

(167) Stone, N.; Kerssens, M.; Lloyd, G. R.; Faulds, K.; Graham, D.; Matousek, P. *Chem. Sci.* **2011**, *2*, 776.

(168) Yuen, J. M.; Shah, N. C.; Walsh, J. T.; Glucksberg, M. R.; Van Duyne, R. P. *Anal. Chem.* **2010**, *82*, 8382.

(169) Doering, W. E.; Piotti, M. E.; Natan, M. J.; Freeman, R. G. *Adv. Mater.* **2007**, *19*, 3100.

(170) Mulvaney, S. P.; Musick, M. D.; Keating, C. D.; Natan, M. J. *Langmuir* **2003**, *19*, 4784.

(171) Doering, W. E.; Nie, S. *Anal. Chem.* **2003**, *75*, 6171.

(172) Freeman, R. G.; Doering, W. E.; Walton, I. D.; Penn, S. G.; Davis, G.; Wong, F.; Natan, M. J. *Proc. SPIE* **2005**, 114-122.

(173) Schiestel, T.; Brunner, H.; Tovar, G. E. *J. Nanosci. Nanotechnol.* **2004**, *4*, 504.

(174) Stone, N.; Baker, R.; Rogers, K.; Parker, A. W.; Matousek, P. *Analyst* **2007**, *132*, 899.

(175) Stone, N.; Matousek, P. *Cancer Res.* **2008**, *68*, 4424.

(176) Muller, L.; de Escauriaza, M. D.; Lajoie, P.; Theis, M.; Jung, M.; Muller, A.; Burgard, C.; Greiner, M.; Snapp, E. L.; Dudek, J.; Zimmermann, R. *Mol. Biol. Cell*, *21*, 691.

(177) Timlin, J. *J. Biomed. Opt.* **1999**, *4*, 28.

(178) Kukreti, S.; Cerussi, A.; Tromberg, B.; Gratton, E. *Dis. Markers* **2008**, *25*, 281.

(179) Matcher, S. J.; Cope, M., Delpy, D. T. *Phys. Med. Biol.* **1994**, *39*, 177.

(180) Xia, J. J.; Berg, E. P.; Lee, J. W.; Yao, G. *Meat Sci.* **2007**, *75*, 78.

(181) Wang, Q.; Lonergan, S. M.; Yu, C. *Meat Sci.* **2012**, *91*, 232.

(182) Spiegelberg, C.; Geng, J.; Hu, Y.; Kaneda, Y.; Jiang, S.; Peyghambarian, N. *J. Lightwave Technol.* **2004**, *22*, 57.

(183) Brolo, A. G.; Sanderson, A. C.; Smith, A. P. *Phys. Rev. B* **2004**, *69*, 045424.